HZDR-060

Wissenschaftlich-Technische Berichte
HZDR-060 2015 · ISSN 2191-8708

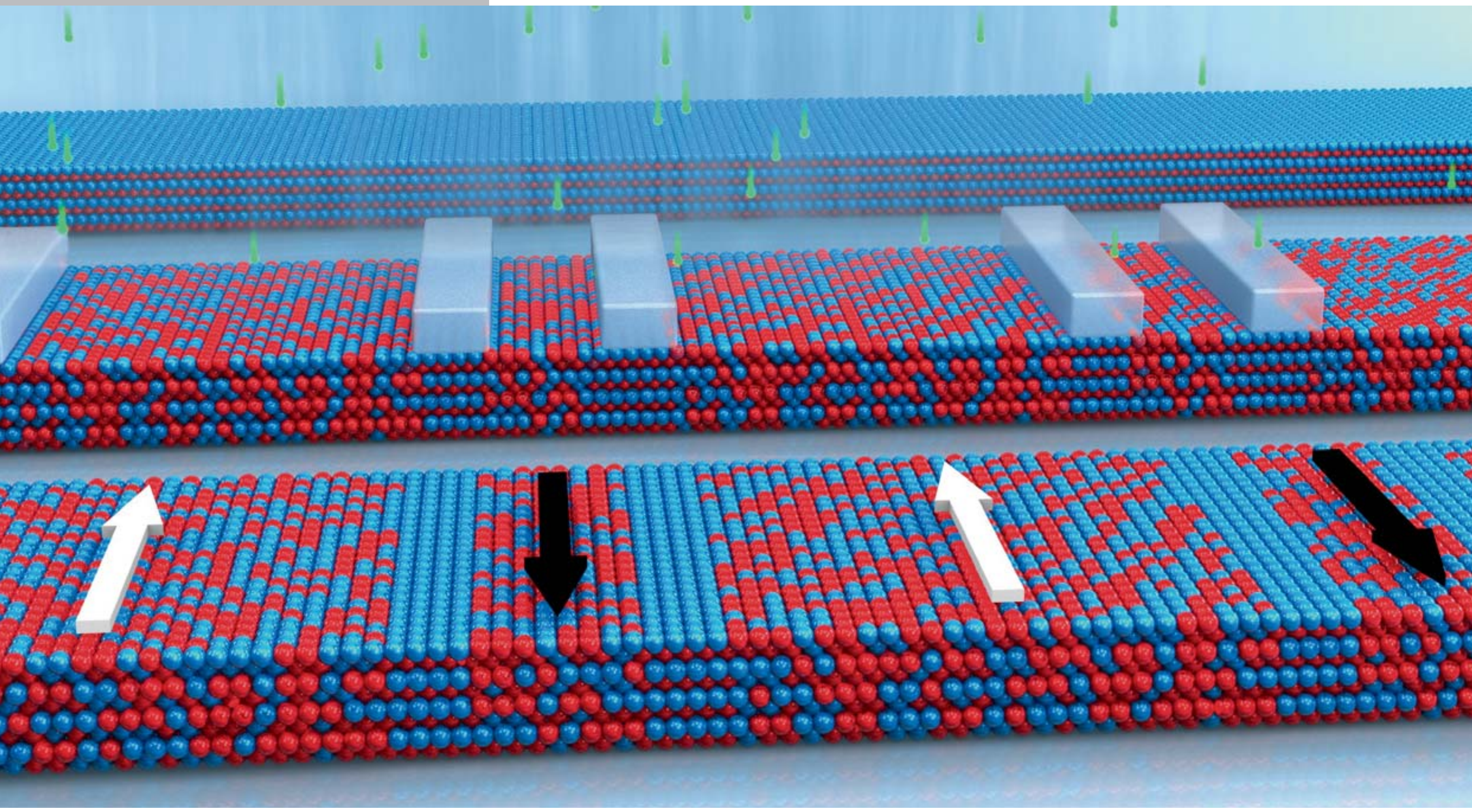

ANNUAL REPORT 2014

INSTITUTE OF ION BEAM PHYSICS AND MATERIALS RESEARCH

HZDR

HELMHOLTZ
ZENTRUM DRESDEN
ROSSENDORF

Wissenschaftlich-Technische Berichte
HZDR–060

Annual Report 2014

Institute of Ion Beam Physics and Materials Research

Editors

J. Fassbender, V. Heera,
M. Helm, P. Zahn

HZDR

HELMHOLTZ
ZENTRUM DRESDEN
ROSSENDORF

Cover Picture

The cover shows a schematic of the concept of a spin valve device produced using ion-beam irradiation. Consider a mesoscopic $Fe_{60}Al_{40}$ wire, seen in the background, composed of well-ordered atomic planes of Fe (blue spheres) and Al (red spheres) atoms. This chemically ordered structure is non-magnetic, but it transforms to a ferromagnetic state when the atomic arrangement is disordered. To achieve this transformation locally at the nanoscale, resist masks were placed on the wire (middle row). The wire was irradiated with Ne^+ ions at an energy of 20 keV and a low fluence of 6×10^{14} ions cm^{-2}. The ions penetrate the ordered lattice and randomize the atomic arrangement, thereby magnetizing the disturbed regions. Regions covered by the resist mask are not influenced by the energetic ions, and remain non-magnetic. The resulting tailored magnetic stripes (front row) are isolated from each other by sub-50 nm non-magnetic spacers. The magnetization directions of such stripes can be aligned using external magnetic fields. As an electric current traverse through these stripes, spin-polarization and spin-scattering phenomena occur, causing the electrical resistance to be dependent on the stripe magnetization directions. Such devices, known as spin valves, are crucial for sensing magnetic fields, for instance in data-storage devices. Future magneto-transport devices could potentially be produced using ion-beam irradiation. Image: HZDR / S. Münster

For further information see:
R. Bali et al., Nano Lett. **14** (2), pp. 435–441 (2014),
reprinted at pp. 18–24 of this Annual Report.

Print edition: ISSN 2191-8708
Electronic edition: ISSN 2191-8716

Published by Helmholtz-Zentrum Dresden - Rossendorf e.V.

This report is also available at https://www.hzdr.de/FWI.

Helmholtz-Zentrum Dresden - Rossendorf e.V.
Institute of Ion Beam Physics and Materials Research
Bautzner Landstraße 400
01328 Dresden
Germany

Directors	Prof. Dr. M. Helm	Prof. Dr. J. Fassbender
Phone	+ 49 (351) 260 2260	+ 49 (351) 260 3096
Fax	+ 49 (351) 260 3285	+ 49 (351) 260 3285
Email	m.helm@hzdr.de	j.fassbender@hzdr.de

www.hzdr.de/FWI

Preface by the directors

This past year 2014 was the year when we finally completely arrived as a “full member” in the Helmholtz Association. This is related to the successfully passed research evaluation in the framework of the Program Oriented Funding (POF), which will give us a stable and predictable funding for the next five years (2015 – 2019). This is particularly true for our large-scale user facilities, like the Ion Beam Center (IBC) and the electron accelerator ELBE with the free-electron laser. Most of our activities are assigned to the program “**From Matter to Materials and Life**” within the research area “Matter”, in cooperation with several other German Helmholtz Centers. Our in-house research is performed in three so-called research themes, as depicted in the schematic below. What is missing there for simplicity is a small part of our activities in the program “Nuclear Waste Management and Safety” within the research area “Energy”.

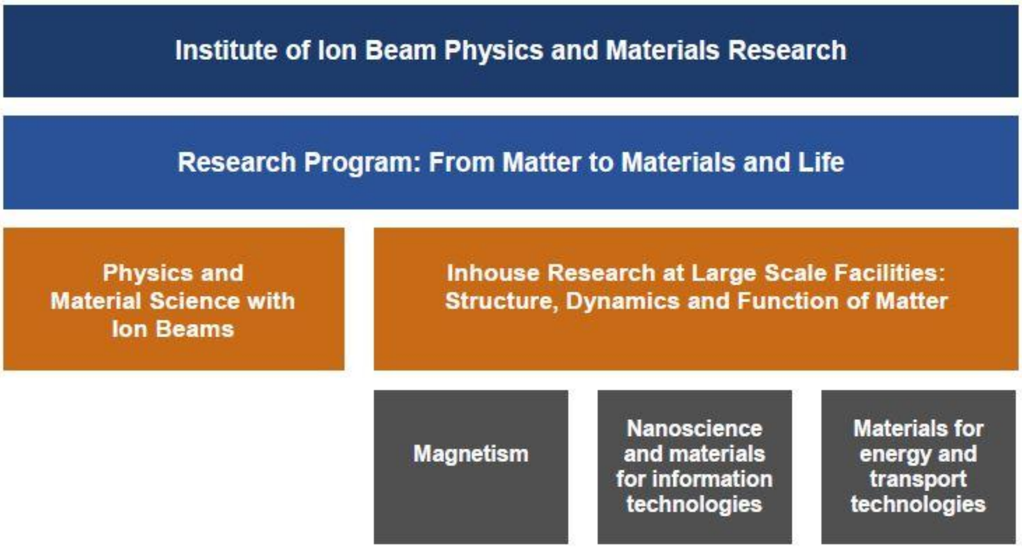

Our research and facilities were well appreciated by the evaluation committee, who made the following judgement about the Ion Beam Center:

“The Ion Beam Centre (IBC) of HZDR is an internationally leading ion-beam facility (with ion energies ranging from several eV to several tens of MeV). At both the national and international level it is one of the key players and is unique in its kind. The synergy between forefront research and user service has been leading to a very good publication output for both in-house research and user research. …

The very broad range of beam energies, the versatility of techniques and applications – both for ion beam modification of materials and for ion-beam analysis – makes the IBC unique in its kind. …

The strength of IBC is that its activities are based on a combination of forefront research and user service, which mutually interact in synergy and strengthen one another. In turn, this synergy has been leading to a very good publication output for both in-house research and user research.”

In order to make our Annual Report a bit more compact, we have decided to include only four full journal papers this year. This was also triggered by the fact that our publication activities have turned out be become more diverse, in more diverse journals than in the past, and often through longer papers, which would be too long to reprint them here. However, apart from the constantly quantitatively high publication output, we succeeded to publish in excellent journals such as Nature Physics, Nano Letters and Physical Review Letters, in fields as diverse as ion beam physics, magnetism and terahertz spectroscopy.

Two of our scientists, Dr. Artur Erbe and Dr. Alexej Pashkin obtained their Habilitation in 2014, both at University of Konstanz. For the first time, we are hosting an Emmy Noether Young Investigator Group funded by the Deutsche Forschungsgemeinschaft (DFG); the group works on the hot topic of magnonics and is headed by Dr. Helmut Schultheiß.

Finally we would like to cordially thank all partners, friends, and organizations who supported our progress in 2014. Special thanks are due to the Executive Board of the Helmholtz-Zentrum Dresden-Rossendorf, the Minister of Science and Arts of the Free State of Saxony, and the Minister of Education and Research of the Federal Government of Germany. Numerous partners from universities, industry and research institutes all around the world contributed essentially, and play a crucial role for the further development of the institute. Last but not least, the directors would like to thank again all IIM staff for their efforts and excellent contributions in 2014.

Prof. Manfred Helm

Prof. Jürgen Fassbender

Contents

Selected Publications

Statistics

Selected Publications

Image: HZDR / S. Münster

Copyright remarks

The following journal articles are reprinted with kind permission from:

Mittendorff, M.; Wendler, F.; Malic, E.; Knorr, A.; Orlita, M.; Potemski, M.; Berger, C.; de Heer, W. A.; Schneider, H.; Helm, M.; Winnerl, S.
Carrier dynamics in Landau-quantized graphene featuring strong Auger scattering
Nature Physics, Vol. **11**, pp. 75-81
© 2014 Macmillan Publishers Limited
DOI: 10.1038/NPHYS3164

Bali, R.; Wintz, S.; Meutzner, F.; Hübner, R.; Boucher, R.; Ünal, A. A.; Valencia, S.; Neudert, A.; Potzger, K.; Bauch, J.; Kronast, F.; Facsko, S.; Lindner, J.; Fassbender, J.
Printing nearly-discrete magnetic patterns using chemical disorder induced ferromagnetism
Nano Letters, Vol. **14**, pp. 435-441
© 2013 American Chemical Society
DOI: 10.1021/nl404521c

Wilhelm, R. A.; Gruber, E.; Ritter, R.; Heller, R.; Facsko, S.; Aumayr, F.
Charge exchange and energy loss of slow highly charged ions in 1 nm thick carbon nanomembranes
Physical Review Letters, Vol. **112**, Art.-No. 153201
© 2014 American Physical Society
DOI: 10.1103/PhysRevLett.112.153201

Khalid, M.; Weschke, E.; Skorupa, W.; Helm, M.; Zhou, S.
Ferromagnetism and impurity band in a magnetic semiconductor: InMnP
Physical Review B, Vol. **89**, Art.-No. 121301(R)
© 2014 American Physical Society
DOI: 10.1103/PhysRevB.89.121301

nature physics

ARTICLES

Carrier dynamics in Landau-quantized graphene featuring strong Auger scattering

Martin Mittendorff[1,2*†], Florian Wendler[3], Ermin Malic[3], Andreas Knorr[3], Milan Orlita[4,5], Marek Potemski[4], Claire Berger[6,7], Walter A. de Heer[6,8], Harald Schneider[1], Manfred Helm[1,2] and Stephan Winnerl[1*]

The energy spectrum of common two-dimensional electron gases consists of a harmonic (that is, equidistant) ladder of Landau levels, thus preventing the possibility of optically addressing individual transitions. In graphene, however, owing to its non-harmonic spectrum, individual levels can be addressed selectively. Here, we report a time-resolved experiment directly pumping discrete Landau levels in graphene. Energetically degenerate Landau-level transitions from $n = -1$ to $n = 0$ and from $n = 0$ to $n = 1$ are distinguished by applying circularly polarized THz light. An analysis based on a microscopic theory shows that the zeroth Landau level is actually depleted by strong Auger scattering, even though it is optically pumped at the same time. The surprisingly strong electron–electron interaction responsible for this effect is directly evidenced through a sign reversal of the pump–probe signal.

Transport experiments on graphene in magnetic fields have revealed a number of fascinating phenomena, such as quantum ratchet effects[1], the Hofstadter butterfly[2–4] and the fractional quantum Hall effect[5,6]. The anomalous quantum Hall effect, which is a consequence of a Landau level (LL) at zero energy in graphene (Fig. 1a), is considered a hallmark of the Dirac-fermion nature of charge carriers in graphene[7,8]. The non-equidistant LL structure has been observed in various continuous-wave (cw) magneto-spectroscopy experiments[9–12], which provided evidence for the Dirac-cone band structure at various energies[10,11]. Furthermore, this technique allows one to determine the Fermi velocity[9] and to identify graphene of extremely high quality[12]. The observation of a giant Faraday rotation of light passing through graphene in magnetic fields as well as the demonstration of tunable THz detectors highlight the application potential of graphene in magneto-optic devices[13,14]. For more sophisticated applications such as light emitters, however, a detailed knowledge of the carrier dynamics is required.

Although the relaxation dynamics in graphene at zero magnetic field has been studied intensively[15–20] there is so far only one time-resolved spectroscopy study in the presence of a magnetic field[21], in which a pump probe study was performed at high energies corresponding to the excitation of a quasi-continuum of LLs characterized by a LL separation smaller than the LL broadening. The observed increase in relaxation time at enhanced magnetic fields was attributed to a suppression of Auger processes[21]. The role of Auger scattering bridging the valence and conduction bands and changing the number of charge carriers has been controversially discussed for graphene in the absence of magnetic fields[19,22,23]. Charge carriers fulfil energy and momentum conservation for Auger processes only along a straight line on the Dirac cone. It has been argued that the contribution of processes restricted to lines in *k*-space vanishes in the two-dimensional phase space. However, full quantum-mechanical treatments of the ultrafast carrier dynamics indicate that Auger processes, that is, Auger recombination and impact ionization, are very efficient in graphene[19,24–26]. The possibility of generating multiple electron–hole pairs due to impact ionization dominating over Auger recombination is at present a fascinating research topic. Although evidence for carrier multiplication was found in a pump–probe experiment[19], two time- and angle-resolved photoemission spectroscopy studies do not report this effect[27,28]. However, the applied high pump fluence in the range of 1 mJ cm^{-2} in refs 27,28 results in a regime where Auger recombination is predicted to be predominant, preventing carrier multiplication from occurring[25,26]. Owing to their specific energy structure, the energetically lowest LLs, which can be selectively excited in the experiment, open a unique route to investigate the importance of Auger scattering in graphene.

In this Article, we present a joint experimental and theoretical study investigating the carrier dynamics in Landau-quantized graphene by selectively pumping and probing transitions between low-energy LLs. Hence, for the first time, the discrete graphene LL system is investigated in a time-resolved study. We apply radiation with a photon energy of 75 meV (wavelength: 16.5 μm) and magnetic fields of up to 7 T to address the possible relaxation channels of excited electrons in the presence of a magnetic field. Thorough understanding of the dynamics in this unique discrete-level system is obtained by performing pump–probe experiments with circularly polarized radiation, which allows one to selectively address the degenerate $\mathrm{LL}_{-1} \rightarrow \mathrm{LL}_0$ and $\mathrm{LL}_0 \rightarrow \mathrm{LL}_1$ transitions (Fig. 1a). Our main observation is that for one of the four possible combinations of pumping and probing with left- and right-circularly polarized radiation, the differential transmission signal (DTS) shows the opposite sign with respect to the signal

---

[1]Helmholtz-Zentrum Dresden-Rossendorf, PO Box 510119, 01314 Dresden, Germany. [2]Technische Universität Dresden, 01062 Dresden, Germany. [3]Technische Universität Berlin, Hardenbergstraße 36, 10623 Berlin, Germany. [4]Laboratoire National des Champs Magnétiques Intenses, CNRS-UJF-UPS-INSA, 38042 Grenoble, France. [5]Charles University Faculty of Mathematics and Physics, Ke Karlovu 5, 121 16 Praha, Czech Republic. [6]Georgia Institute of Technology, Atlanta, Georgia 30332, USA. [7]CNRS — Institut Néel, 38042 Grenoble, France. [8]Department of Physics, King Abdulaziz University, Jeddah 22254, Saudi Arabia. †Present address: University of Maryland, College Park, Maryland 20742, USA. *e-mail: mhm@umd.edu; s.winnerl@hzdr.de

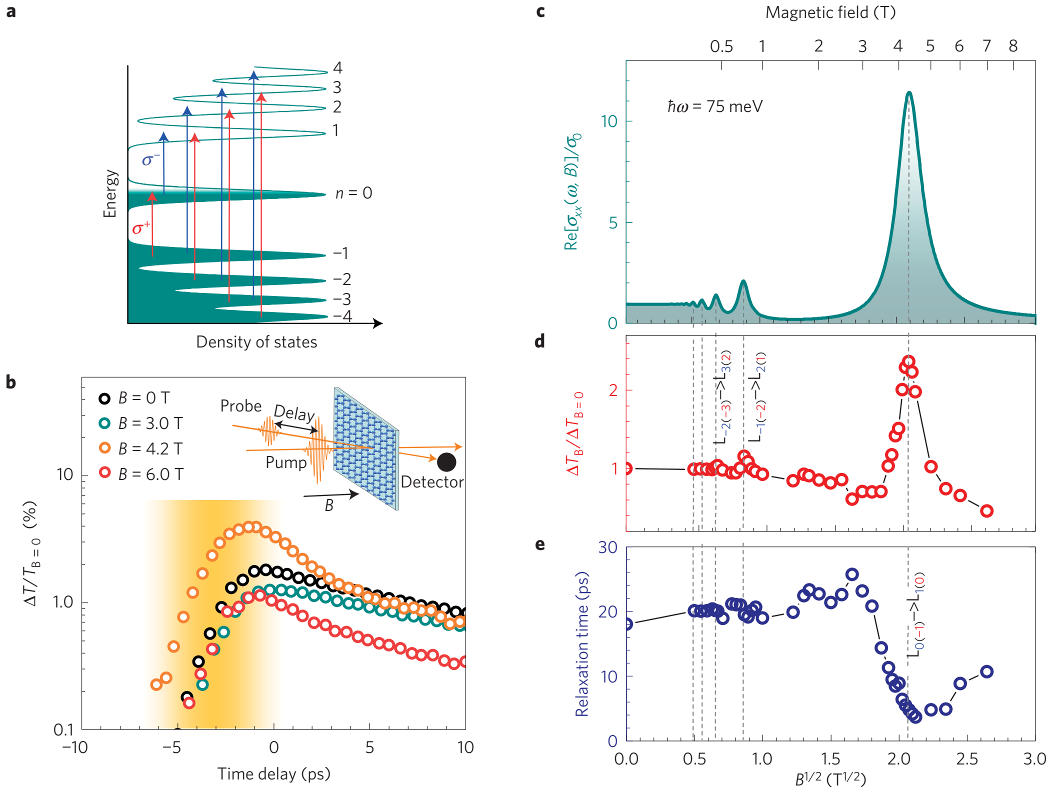

Figure 1 | Pump–probe spectroscopy on graphene with linearly polarized radiation. **a**, LL spectrum of graphene with allowed dipole transitions for σ^- and σ^+-radiation. **b**, Pump–probe signals for different magnetic fields. In the inset the pump–probe experiment involving linearly polarized beams is depicted. In this case, transitions allowed for σ^--radiation as well as σ^+-radiation are excited and probed. **c**, Dynamic conductivity, which is proportional to the absorption, of one graphene layer. The calculation, as well as all experimental data in the other panels, corresponds to a photon energy of 75 meV. **d**, *B*-dependent pump-induced maximum transmission change normalized to the case at zero magnetic field. **e**, Initial decay time of the pump–probe signal for varied magnetic fields. For magnetic fields below 3 T this decay time corresponds to the slow component of the dynamics, whereas for higher fields it is dominated by the additional fast component. The dashed lines in **d** and **e** identify the corresponding LL transitions. Here the red (blue) subscripts denote transitions excited by σ^+ (σ^-) radiation, see also **a**.

expected from the usually applied single particle absorption bleaching scheme. This observation reveals a highly efficient elastic relaxation channel that we can unambiguously identify by performing microscopic time-resolved calculations of the carrier dynamics. The experiments and calculations show that Auger scattering is the predominant relaxation process giving rise to a redistribution of carriers in Landau-quantized graphene on a picosecond timescale. The fundamental insights obtained into the nature of carrier–carrier scattering in graphene in the presence of a magnetic field are relevant for novel applications, such as graphene-based Landau lasers.

The time-resolved experiments were performed on multilayer (~40 layers) epitaxial graphene (MEG) grown by thermal decomposition on the C-terminated face of SiC (ref. 29). The decoupled nature of the layers of the sample was evidenced by Raman spectroscopy[30] and cw magneto-spectroscopy[9]. The majority of graphene layers exhibit weak doping[11,18], although layers close to the interface of SiC are strongly n-doped[16,31,32]. In our sample the majority of layers is n-type, with an electron concentration in the range of several $10^{10}\,\mathrm{cm}^{-2}$ (see details of sample doping in Methods). The free-electron laser FELBE delivered radiation pulses with a duration of 2.7 ps (full-width at half-maximum, FWHM) and a photon energy of 75 meV. Various pump–probe experiments were performed, involving linear polarization as well as left- and right-circularly polarized radiation for pumping and probing. A simplified sketch of the experiment with linearly polarized radiation is shown in the inset of Fig. 1b. Details on the experimental configuration can be found in the Methods. In all experiments, the sample temperature was kept at 10 K in a cryostat that allows the application of magnetic fields up to 7 T.

In the following, induced transmission transients (Fig. 1b) are analysed. The features of the induced transmission amplitudes (Fig. 1d) and the initial relaxation time (Fig. 1e) are identified by comparing their *B*-field dependence to the dynamic conductivity of a graphene layer (Fig. 1c). The dynamic conductivity, which is proportional to the absorption, is calculated using the Kubo formalism[9], considering the dipole radiation selection rule $|\Delta n| = 1$. A width of 7 meV is chosen in accord with cw magneto-spectroscopy data[11]. The calculation allows us to attribute peaks in the induced transmission to the interband transitions $\mathrm{LL}_{-1(0)} \rightarrow \mathrm{LL}_{0(1)}$, $\mathrm{LL}_{-2(-1)} \rightarrow \mathrm{LL}_{1(2)}$ and $\mathrm{LL}_{-3(-2)} \rightarrow \mathrm{LL}_{2(3)}$ in weakly n-doped graphene layers (Fig. 1c,d). On resonance with these transitions the induced transmission is enhanced. The strongest resonant enhancement (by factor of 2.5 relative to the signal at $B = 0$) is observed for the energetically lowest transition (Fig. 1d). Note that owing to the vanishing density of states between LLs (for example, for $1\,\mathrm{T} < B < 3\,\mathrm{T}$) the pump–probe signal is expected to vanish in this region. The observed non-zero signals in the experiment most likely stem from intraband LL transitions in the highly doped graphene layers close to the interface with the SiC substrate. In cw magneto-spectroscopy experiments, broad absorption features from doped layers have already been observed[33,34] supporting this interpretation.

For magnetic fields below 3 T the relaxation dynamics is characterized by a single exponential decay with a time constant of about 20 ps (Fig. 1b,e). For higher magnetic fields an additional fast decay component is observed. At $B = 4.2$ T the $\mathrm{LL}_{-1(0)} \to \mathrm{LL}_{0(1)}$ transition is resonantly excited. Here, we observe a fast initial decay of $\tau = (3 \pm 1)$ ps—that is, the initial dynamics is almost one order of magnitude faster than the slow component. This very fast decay of the pump–probe signal is surprising, as the LL spacing does not match the energy of optical phonons and, thus, the carrier–phonon scattering is expected to be strongly quenched[35,36].

To shed light on the nature of the observed fast population change responsible for the acceleration of the carrier dynamics, we employ circularly polarized radiation (σ^+ and σ^--radiation). We record DTS successively for all four combinations of pumping and probing with σ^+ and σ^--radiation (see Fig. 2a). According to the optical selection rules, σ^+-radiation pumps the $\mathrm{LL}_{-1} \to \mathrm{LL}_0$ transition and σ^--radiation the $\mathrm{LL}_0 \to \mathrm{LL}_1$ transition[37] (see Fig. 2b). It is instructive to visualize the expected DTS sign in the absence of scattering for intrinsic graphene—that is, for initial occupations $\rho_0 = 0.5$, $\rho_{-1} = 1$ and $\rho_1 = 0$. This system is fully symmetric with respect to electrons and holes and, consequently, with respect to excitation by σ^+ and σ^--radiation. In this case, assuming that the dynamics is determined only by Pauli blocking, one expects positive DTS (increased transmission) for pumping and probing with the same polarization state and negative pump–probe signals (increased absorption) for pumping and probing with the opposite polarization state (see Fig. 2b). The signals within one pair of similar and opposite polarization feature similar amplitudes. For doped graphene the electron–hole symmetry is broken; hence, the absolute values of the induced transmission differ for the four different polarization combinations. Nevertheless, this does not change the expected DTS sign discussed above. Furthermore, energy relaxation via phonons and defect-mediated phonon scattering have no influence, as these processes relax the carrier distribution back into the equilibrium state.

The experiments show the following behaviour: the DTS for pumping with σ^--radiation (Fig. 2c,e) exhibits a fast initial decay, of the order of the pulse duration, and a slower relaxation component. The sign of the DTS is in accord with the expectation considering the pump scheme depicted in Fig. 2b. In particular, negative DTS is observed for pumping with σ^--radiation and probing with σ^+-radiation (Fig. 2e). For pumping with σ^+-radiation and probing with σ^--radiation (Fig. 2g), however, an unexpected positive signal is observed, indicating that a strong redistribution of carriers must take place, beyond the effect induced by the photon field. A possible explanation is efficient Auger scattering, which can lead to a fast redistribution of carriers, giving rise to a different sign of the DTS. One can distinguish two counteracting Auger scattering processes, inducing $\mathrm{LL}_0 \to \mathrm{LL}_{-1}$, $\mathrm{LL}_0 \to \mathrm{LL}_1$ and $\mathrm{LL}_{-1} \to \mathrm{LL}_0$, $\mathrm{LL}_1 \to \mathrm{LL}_0$ transitions, respectively, as indicated in the sketches to the left of the panels containing the experimental data (Fig. 2c, e,g,i). Generally, they are referred to as Auger recombination and impact ionization, respectively. In graphene, the terminology is not straightforward, as LL_0 is shared by the valence and the conduction bands. Therefore, in the following, we will refer to $\mathrm{LL}_0 \to \mathrm{LL}_{-1}$ and $\mathrm{LL}_0 \to \mathrm{LL}_1$ ($\mathrm{LL}_{-1} \to \mathrm{LL}_0$ and $\mathrm{LL}_1 \to \mathrm{LL}_0$) as outward (inward) Auger scattering with respect to the zeroth LL. Finally, the DTS for pumping with σ^+-radiation and probing with σ^+-radiation contains a negative tail after an initially positive peak (see Fig. 2i). Such a behaviour cannot be understood by just considering optical pumping and energy relaxation—again suggesting a crucial contribution from Auger scattering.

To obtain a thorough understanding of the underlying elementary scattering processes we performed microscopic calculations. Next, the foundation of the model is described, then we compare experimental and calculated DTS results and, finally, we discuss the microscopic mechanism behind the experimentally observed and theoretically confirmed unexpected DTS behaviour. Our model is based on the density matrix formalism[38,39]. Similar to previous modelling in the absence of a magnetic field[18,40], we derive a set of equations describing time-resolved microscopic polarizations $p_{nn'}(t)$ and population probabilities $\rho_n(t)$

$$\dot{\rho}_n(t) = \pm 2 \sum_{n'} \mathrm{Re}[\Omega_{nn'}(t) p_{nn'}(t)] + S_n{}^{\mathrm{in}}(t)[1 - \rho_n(t)] - S_n{}^{\mathrm{out}}(t) p_n(t)$$

$$\dot{p}_{nn'}(t) = i\Delta\omega_{nn'} p_{nn'}(t) + \Omega_{nn'}(t)[\rho_n(t) - \rho_{n'}(t)] - \frac{\Gamma(t)}{\hbar} p_{nn'}(t)$$

Here $\Omega_{nn'}(t)$ denotes the Rabi frequency, $\Delta\omega_{nn'}$ the LL transition frequency, $S_n{}^{\mathrm{in/out}}(t)$ the time-dependent in- and out-scattering rates and $\Gamma(t)$ the many-particle and disorder-induced dephasing of the microscopic polarization. The magnetic field was introduced in the Dirac equation via the Peierls substitution[37]. The equations include the optical excitation as well as Coulomb- and phonon-induced many-particle scattering processes. The strength of the carrier–light interaction is given by the optical matrix element and depends on the excitation field, both being incorporated into the Rabi frequency. The time- and LL-dependent in- and out-scattering rates $S_n{}^{\mathrm{in/out}}(t) = S_n{}^{\mathrm{in/out}}|_{\mathrm{Coulomb}}(t) + S_n{}^{\mathrm{in/out}}|_{\mathrm{phonon}}(t)$ describe energy-conserving many-particle Coulomb processes and inelastic scattering with phonons. The efficiency of the former is determined by the Coulomb matrix elements that are obtained using tight-binding wavefunctions. The microscopic treatment of the Coulomb interaction is crucial for understanding the experimentally observed fast carrier dynamics. In contrast, the carrier–phonon scattering is negligibly small at the beginning, owing to the mismatch of the optical phonon energy and the investigated inter-LL transitions. Scattering with acoustic phonons assisted by impurities is expected to contribute to the experimentally observed slower component in the differential transmission spectra (for details of modelling refer to Methods). The modelling was performed for low n-type graphene with a carrier concentration of 6×10^{10} cm^{-2}, which corresponds a filling of LL_0 of 64% at 4.2 T. (At $B = 0$ this would correspond to a Fermi energy of 28 meV, see also Methods for details of sample doping.) First, we optically generate a non-equilibrium distribution by applying a circularly polarized pulse with a width of 2.7 ps, a pump fluence of 0.1 μJ cm^{-2} and an excitation energy of 75 meV, corresponding to the experimental realization. Then, we investigate the temporal evolution of the microscopic polarization $p_{nn'}$ and the carrier occupations $\rho_n(t)$ in the involved LLs. We focus on the carrier dynamics within the energetically lowest LLs.

The calculated differential transmission reproduces well all qualitative features of the measured DTS (see Fig. 2d,f,h,j). For pumping with σ^+-radiation, the theoretical curves show the same surprising result as observed in the experiment, namely the unexpected positive signal for probing with σ^--radiation and the initially positive and subsequently negative signal for probing with σ^+-radiation (Fig. 2h,j). We note that by artificially weakening the electron–electron coupling the expected negative DTS is obtained for pumping and probing with opposite polarization (see Supplementary Methods), confirming that Auger processes are indeed the reason for the surprising positive DTS observed in the experiment, as further discussed below. Note that for pumping with σ^--radiation, the signals are in accord with the expectations considering the optical selection rules; however, when probing with σ^+-radiation a plateau after the initial peak is observed in the DTS (Fig. 2f). This is an indication that also in this configuration the underlying dynamics is more complex than a simple relaxation to the equilibrium. The processes leading to the plateau are further discussed in the Supplementary Methods.

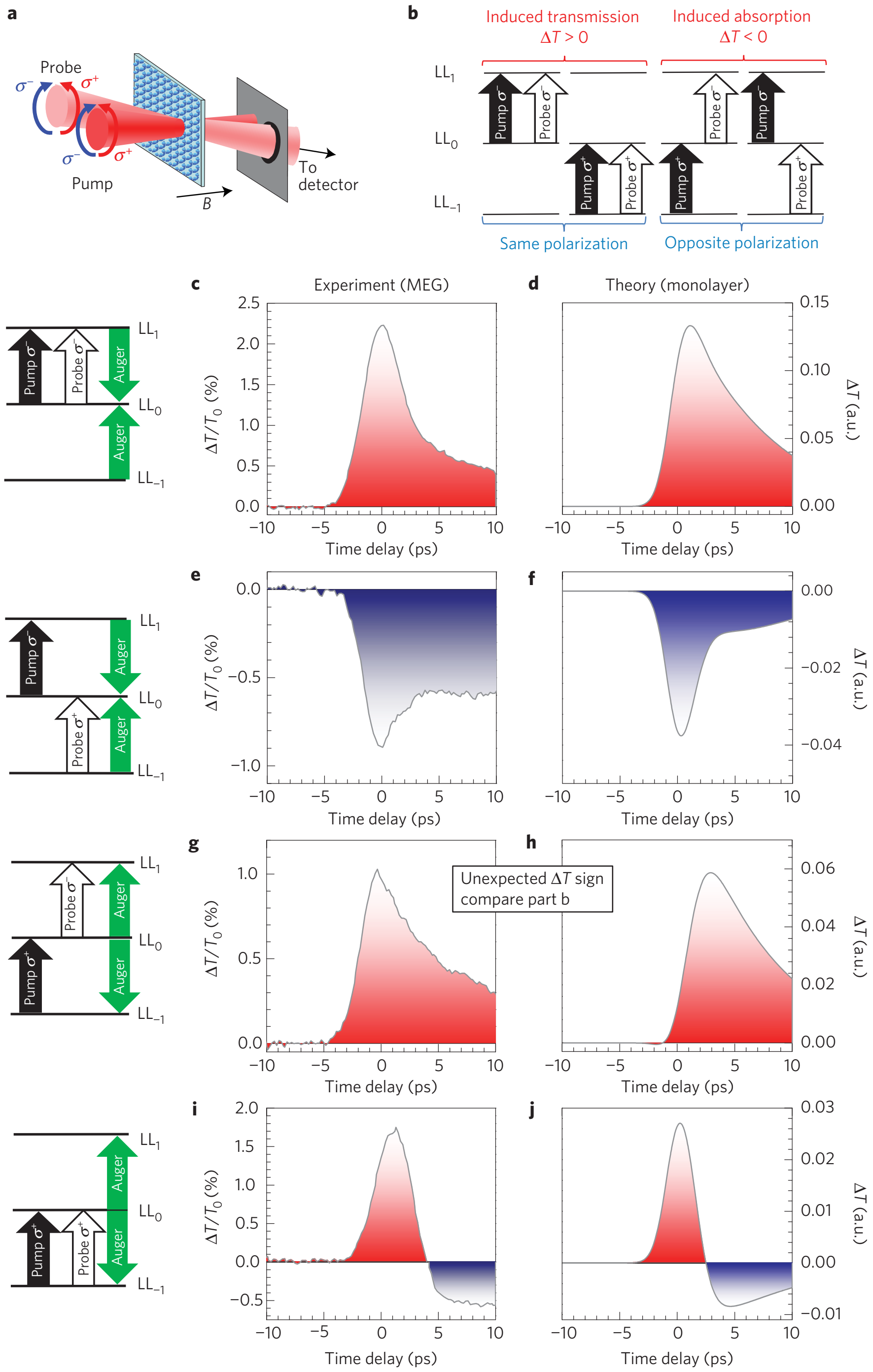

Figure 2 | Pump–probe spectroscopy on graphene with circularly polarized radiation. **a**, Configuration of the experiments for pumping and probing with σ^- and σ^+-radiation. **b**, In the absence of strong Auger scattering, pumping and probing with the same polarization results in induced transmission, whereas applying opposite polarization results in induced absorption. **c**,**e**,**g**,**i**, Experimental pump–probe signals for all four combinations of pumping and probing with σ^- and σ^+-radiation. Blue and red shaded regions highlight positive and negative DTS, respectively. **d**,**f**,**h**,**j**, Differential transmission calculated by microscopic theory for all four combinations of pumping and probing with σ^- and σ^+-radiation. The diagrams left of panels **c**–**j** indicate the corresponding polarization of pump and probe beam as well as the dominating Auger scattering process—that is, either inward or outward Auger scattering. The photon energy is 75 meV and $B = 4.2$ T for all panels. a.u., arbitrary units.

As our calculations give microscopic access to the time-resolved populations of the LLs, we can reveal the underlying elementary scattering processes responsible for the observed and theoretically predicted surprising features in the differential transmission spectra. Our calculations clearly reveal that Auger processes play the crucial role. They give rise to an efficient redistribution of carriers in the energetically equidistant levels LL_0, LL_1 and LL_{-1}. The time-resolved occupations of the energetically lowest LLs are

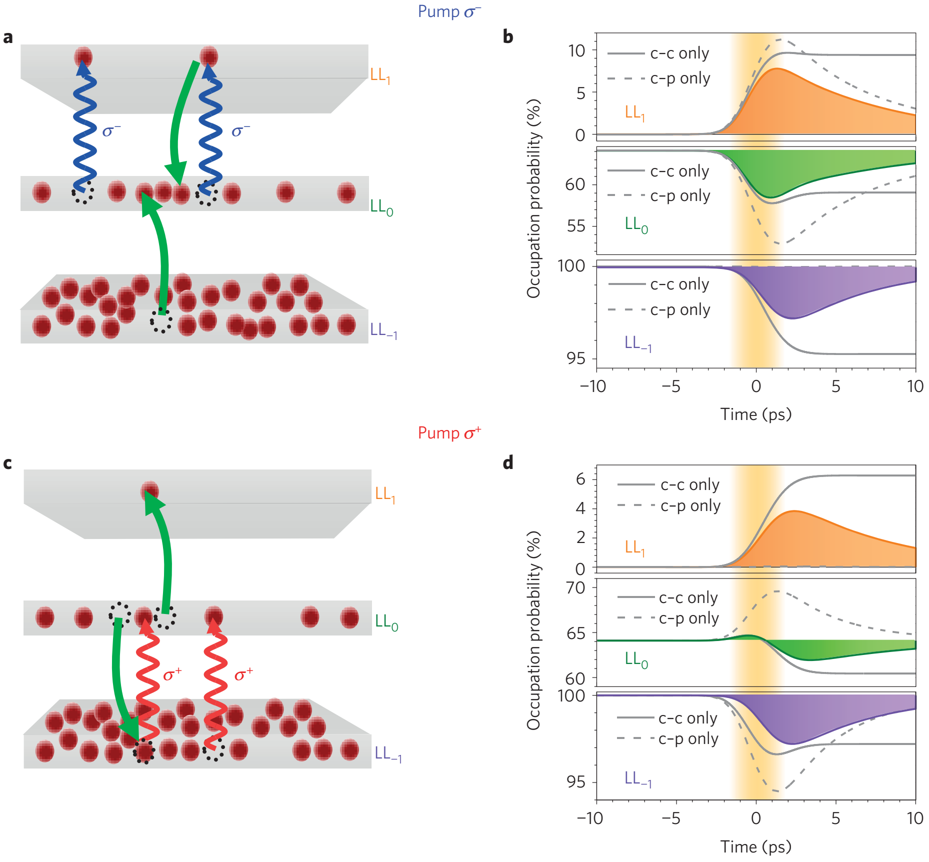

Figure 3 | Level occupation for pumping with circularly polarized radiation. a,**c**, Illustration of the transitions between LL_{-1}, LL_0 and LL_1 induced by optical pumping and the net Auger scattering. The green arrows symbolize the predominant contribution of inward (**a**) or outward (**c**) Auger scattering. **b**,**d**, Occupations of the LLs corresponding to **a** and **c**, respectively, calculated by microscopic modelling, taking into account the optical excitation, carrier–carrier and carrier–phonon scattering (coloured curves). The solid (dashed) grey line corresponds to the dynamics considering optical excitation and carrier–carrier (carrier–phonon) scattering only. The vertical orange shaded area indicates the duration of the pump pulse.

shown in Fig. 3: for pumping with σ^--radiation, optical excitation depopulates LL_0, leading to a decrease of $\rho_0(t)$ (Fig. 3b). At the same time, LL_1 becomes populated, resulting in an increase of $\rho_1(t)$. In the case of pumping with σ^--radiation, inward Auger scattering dominates, because it counteracts the optical pumping (Fig. 3a). This effect causes the decreased occupation of LL_{-1}, which is not affected by the optical pumping (Fig. 3b). In contrast, for pumping with σ^+-radiation, outward Auger scattering dominates over inward processes (Fig. 3c). In n-type graphene, the Auger scattering is so efficient that, after an initial increase of $\rho_0(t)$ due to the optical pumping, an Auger-induced decrease is found (Fig. 3d). As a result, we do not observe enhanced absorption and negative DTS as expected for pumping with σ^+ and probing with σ^--radiation (Fig. 2b), but rather a positive pump–probe signal (see Fig. 2g,h). The Auger scattering efficiently populates LL_1, giving rise to absorption bleaching of the σ^--probe pulse and resulting in positive differential transmission. The initial increase and subsequent decrease of the occupation of LL_0 is responsible for the sign reversal of the DTS for pumping and probing with σ^+-radiation (see Fig. 2i,j; for a detailed explanation see Supplementary Methods).

It is instructive to separately consider the effects of carrier–carrier and carrier–phonon scattering on the level occupation (see grey lines in Fig. 3b,d). Pure carrier–phonon scattering leads to population changes only in the LLs that are directly affected by the optical pumping. Consequently, in this case the population of LL_0 is increased by σ^+ pumping (Fig. 3d). In contrast, pure carrier–carrier scattering results in a dynamics that is qualitatively very similar to the full dynamics. The only difference is that without phonon scattering the level occupation does not relax back to the initial equilibrium state, because the energy added by the pump pulse cannot be removed from the electronic system. This leads to a new hot-carrier equilibrium state that is characterized by a decreased population of both LL_{-1} and LL_0 as well as an increased population in LL_1 for pumping with both σ^- and σ^+ radiation (Fig. 3b,d).

Note that for intrinsic graphene the effect of the Auger processes on the carrier distribution is not strong enough to change the sign of the DTS. Even small doping breaks the electron–hole symmetry and, consequently, the balance between outward and inward Auger scattering. This results in the surprising effects observed. The same effects observed for n-doped graphene under pumping with σ^+-radiation occur for p-doped graphene under pumping with σ^--radiation. Further reasoning behind the unexpected DTS sign in Fig. 2g can be given using simple thermodynamic arguments. The observed Auger scattering represents a very efficient (elastic) relaxation process that drives the system perturbed by the pump pulse towards the new equilibrium at higher electron temperature. This redistribution is visible, in particular, in the occupation of LL_0, which increases with increasing electron temperature for p-doped graphene, but always decreases in the n-doped system. Counter-intuitively, the latter happens even when LL_0 is directly pumped. The positive DTS sign for a σ^--polarized probe pulse in Fig. 2g thus directly reflects the pump-induced depopulation of LL_0. More detailed considerations described in the Supplementary Methods reveal that positive DTS signals for σ^--polarized probe pulses are expected when the initial occupation of LL_0 exceeds a threshold value of $2-\sqrt{2}\approx 0.59$.

Our study conclusively shows that carrier–carrier scattering is the predominant mechanism for carrier redistribution in Landau-quantized graphene. Scattering with optical phonons, on the other hand, is expected to be strongly suppressed unless the LLs are resonant with the optical phonon energy[35,36]. In the experiments performed, we find only a moderate increase of the decay time with increasing magnetic field, from 18 ± 3 ps at 0 T to 22 ± 3 ps at 3 T (Fig. 1b,e). A possible explanation for this decay component could be defect-assisted scattering with acoustic phonons, which has been identified as an important scattering mechanism in the absence of magnetic fields[41,42]. The role of these phonon-related relaxation channels for Landau-quantized graphene still needs to be thoroughly investigated in future studies.

In conclusion, our results show that Landau-quantized graphene is ideal for the investigation of strong carrier–carrier scattering processes. The levels LL_{-1}, LL_0 and LL_1 are decoupled from the remaining spectrum both with respect to optical excitation and scattering. The three equidistant but optically selectively addressable levels are an ideal system to study energy-conserving carrier–carrier scattering processes. The possibility of polarization-sensitive induced absorption and induced transmission can be applied for concepts of optical switching with high functionality. In quantum information processing, circularly polarized radiation is often used to address quantum bits. The switching in Landau-quantized graphene can be controlled all-optically by the polarization state of the radiation. Electric gating allowing one to switch from n-type to p-type graphene would add even more functionality. Furthermore, the non-equidistant Landau spectrum of graphene offers the possibility of developing a tunable laser. For example, pumping the $LL_{-3}\rightarrow LL_2$ transition should result in population inversion between LL_2 and LL_1. On the other hand, Auger scattering may be directly exploited to realize carrier multiplication in Landau-quantized graphene. To this end, pumping the $LL_{-3}\rightarrow LL_4$ transition Auger scattering between the equidistant levels LL_4, LL_1 and LL_0 can facilitate carrier multiplication.

Methods

Pump–probe spectroscopy. The free-electron laser FELBE provided frequency-tunable Fourier-limited radiation pulses. In the experiments described in the paper a photon energy of 75 meV was chosen. The pulse duration of the 75-meV pulses was 2.7 ps (repetition rate 13 MHz). The pulses were split into pump and probe pulses by a pellicle beam splitter. The polarizations of pump and probe beams were controlled independently. Frequency-tunable quarter-wave plates (from Alphalas GmbH) were used for the generation of circularly polarized radiation. Both the pump and probe beam were focused on the sample in the magnet cryostat by an off-axis parabolic mirror (effective focal length: 178 mm). The spot size on the sample was ∼0.5 mm (FWHM). The pump fluence was $\sim 0.1\,\mu\mathrm{J\,cm^{-2}}$—in this range the DTS increased linearly with pump fluence. The fluence of the probe beam was about 10% of the pump fluence. The time delay between pump and probe pulses was varied by a mechanical delay stage.

Microscopic modelling. In this study, we focus on the impact of Coulomb interactions and include carrier–phonon scattering on a phenomenological level. To this end, the full scattering rate $S_n^{\mathrm{in/out}}|_{\mathrm{phonon}}$ including Pauli-blocking terms and phonon occupations is considered, while the corresponding electron–phonon matrix elements are adjusted to the experimentally observed decay. The phonons are assumed to be in equilibrium with a phonon bath and their occupations are described by the Bose–Einstein distribution. In contrast, the Coulomb interaction is entirely considered on a microscopic footing. We also take dynamical screening of the Coulomb potential into account by evaluating the dielectric function $\varepsilon(q,\omega)$ in the random phase approximation, following the approach of refs 37,43. The LL broadening is calculated self-consistently, taking into account scattering of electrons on an impurity potential with a Gaussian white noise distribution[44]. This electron-impurity scattering yields the dominant contribution to the dephasing $\Gamma(t)$ of the microscopic polarization, which also comprises contributions of Coulomb- and phonon-induced many-particle scattering.

Sample doping. MEG samples grown on the C-terminated face of SiC consist of a number of layers that are rotated against each other. Charge transfer from the SiC substrate results in high doping of the first layer at the interface, with an electron concentration of $10^{13}\,\mathrm{cm^{-2}}$. Successive layers exhibit a doping of ∼30% of the previous layer; hence, after five layers, low carrier concentrations in the range $10^{10}\,\mathrm{cm^{-2}}$–$10^{11}\,\mathrm{cm^{-2}}$ are reached[16,31]. Pump–probe experiments, cw magneto-spectroscopy and angle-resolved photoemission spectroscopy indicate that a substantial number of layers exhibit doping in the region of $10^{10}\,\mathrm{cm^{-2}}$ (refs 9,18,45). For the sample used in our experiment, layers with carrier concentrations of $\sim 10^{10}\,\mathrm{cm^{-2}}$ were evidenced by magneto-spectroscopy and pump–probe experiments. The experiments in all four combinations of pumping and probing with σ^+- and σ^--radiation in magnetic fields directly indicate that LL_0 can be neither completely filled nor completely empty. The completely filled zeroth LL would give $4.1\times 10^{11}\,\mathrm{cm^{-2}}$ electrons for $B=4.2$ T. For $B=0$ this corresponds to a Fermi energy of 53 meV. Note that intrinsic graphene is characterized by $\rho_0=0.5$, corresponding to $2.0\times 10^{11}\,\mathrm{cm^{-2}}$ electrons at $B=4.2$ T. For the microscopic modelling a concentration of excess electrons of $6\times 10^{10}\,\mathrm{cm^{-2}}$ was used. This value corresponds to a total of $2.6\times 10^{11}\,\mathrm{cm^{-2}}$ electrons in LL_0, $\rho_0=(2.6\times 10^{11})/(4.1\times 10^{11})=0.64$ and a Fermi energy (at $B=0$) of 28 meV. This doping value, being in between the experimentally determined borders, provides an overall good agreement between experimental and calculated DTS. By varying the carrier concentration in the calculation, individual features of the DTS change slightly; however, the surprising DTS sign change remains. The experimental signals contain contributions from graphene of different doping due to the gradient in doping towards the substrate. Furthermore, there are slight lateral inhomogeneities, which are averaged owing to the applied infrared beams having a diameter of ∼0.5 mm.

Received 20 March 2014; accepted 20 October 2014;

References

1. Drexler, C. *et al.* Magnetic quantum ratchet effect in graphene. *Nature Nanotech.* **8,** 104–107 (2013).
2. Ponomarenko, L. A. *et al.* Cloning of Dirac fermions in graphene superlattices. *Nature* **497,** 594–597 (2013).
3. Dean, C. R. *et al.* Hofstadter's butterfly and the fractal quantum Hall effect in moire superlattices. *Nature* **497,** 598–602 (2013).
4. Hunt, B. *et al.* Massive Dirac fermions and Hofstadter butterfly in a van der Waals heterostructure. *Science* **340,** 1427–1430 (2013).
5. Bolotin, K. I., Ghahari, F., Shulman, M. D., Stormer, H. L. & Kim, P. Observation of the fractional quantum Hall effect in graphene. *Nature* **462,** 196–199 (2009).
6. Du, X., Skachko, I., Duerr, F., Luican, A. & Andrei, E. Y. Fractional quantum Hall effect and insulating phase of Dirac electrons in graphene. *Nature* **462,** 192–195 (2009).
7. Novoselov, K. S. *et al.* Two-dimensional gas of massless Dirac fermions in graphene. *Nature* **438,** 197–200 (2005).
8. Zhang, Y., Tan, J. W., Stormer, H. L. & Kim, P. Experimental observation of the quantum Hall effect and Berry's phase in graphene. *Nature* **438,** 201–204 (2005).
9. Sadowski, M. L., Martinez, G., Potemski, M., Berger, C. & deHeer, W. A. Landau level spectroscopy of ultrathin graphene layers. *Phys. Rev. Lett.* **97,** 266405 (2006).
10. Plochocka, P. *et al.* High energy limit of massless Dirac fermions in multilayer graphene using magneto-optical transmission spectroscopy. *Phys. Rev. Lett.* **100,** 087401 (2008).
11. Orlita, M. *et al.* Approaching the Dirac point in high-mobility multilayer epitaxial graphene. *Phys. Rev. Lett.* **101,** 267601 (2008).
12. Neugebauer, P., Orlita, M., Faugeras, C., Barra, A-L. & Potemski, M. How perfect can graphene be? *Phys. Rev. Lett.* **103,** 136403 (2009).
13. Crassee, I. *et al.* Giant Faraday rotation in single- and multilayer graphene. *Nature Phys.* **7,** 48–51 (2011).
14. Kawano, Y. Wide-band frequency tunable terahertz and infrared detection with graphene. *Nanotechnology* **24,** 21404 (2013).
15. Dawlaty, J. M., Shivaraman, S., Chandrashekhar, M., Rana, F. & Spencer, M. G. Measurement of ultrafast carrier dynamics in epitaxial graphene. *Appl. Phys. Lett.* **92,** 042116 (2008).
16. Sun, D. *et al.* Ultrafast relaxation of excited Dirac fermions in epitaxial graphene using optical differential transmission spectroscopy. *Phys. Rev. Lett.* **101,** 157402 (2008).
17. Breusing, M. *et al.* Ultrafast nonequilibrium carrier dynamics in a single graphene layer. *Phys. Rev. B* **83,** 153410 (2011).

18. Winnerl, S. *et al.* Carrier relaxation in epitaxial graphene photoexcited near the Dirac point. *Phys. Rev. Lett.* **107,** 237401 (2011).
19. Brida, D. *et al.* Ultrafast collinear scattering and carrier multiplication in graphene. *Nature Commun.* **4,** 1987 (2013).
20. Tielrooij, K. J. *et al.* Photoexcitation cascade and multiple hot-carrier generation in graphene. *Nature Phys.* **9,** 248–252 (2013).
21. Plochocka, P. *et al.* Slowing hot-carrier relaxation in graphene using a magnetic field. *Phys. Rev. B* **80,** 245415 (2009).
22. Foster, M. S. & Aleiner, I. L. Slow imbalance relaxation and thermoelectric transport in graphene. Quasiclassical cyclotron resonance of Dirac fermions in highly doped graphene. *Phys. Rev. B* **79,** 085415 (2010).
23. Otsuji, T. *et al.* Graphene-based devices in terahertz science and technology. *J. Phys. D* **45,** 303001 (2012).
24. Rana, F. Electron–hole generation and recombination rates for Coulomb scattering in graphene. *Phys. Rev. B* **76,** 155431 (2007).
25. Winzer, T., Knorr, A. & Malic, E. Carrier multiplication in graphene. *Nano Lett.* **10,** 4839–4843 (2010).
26. Winzer, T. & Malic, E. Impact of Auger processes on carrier dynamics in graphene. *Phys. Rev. B* **85,** 241404 (2012).
27. Gierz, I. *et al.* Snapshots of non-equilibrium Dirac carrier distributions in graphene. *Nature Mater.* **12,** 1119–1124 (2013).
28. Johannsen, J. C. *et al.* Direct view of hot carrier dynamics in graphene. *Phys. Rev. Lett.* **111,** 027403 (2013).
29. Berger, C. *et al.* Electronic confinement and coherence in patterned epitaxial graphene. *Science* **312,** 1191–1196 (2006).
30. Ferrari, A. C. *et al.* Raman spectrum of graphene and graphene layers. *Phys. Rev. Lett.* **97,** 187401 (2006).
31. Sun, D. *et al.* Spectroscopic measurement of interlayer screening in multilayer epitaxial graphene. *Phys. Rev. Lett.* **104,** 136802 (2010).
32. Winnerl, S. *et al.* Time-resolved spectroscopy on epitaxial graphene in the infrared spectral range: Relaxation dynamics and saturation behaviour. *J. Phys. Condens. Matter* **25,** 054202 (2013).
33. Witowski, A. M. *et al.* Quasiclassical cyclotron resonance of Dirac fermions in highly doped graphene. *Phys. Rev. B* **82,** 165305 (2010).
34. Orlita, M. *et al.* Classical to quantum crossover of the cyclotron resonance in graphene: A study of the strength of intraband absorption. *New J. Phys.* **14,** 095008 (2012).
35. Wang, Z-W. *et al.* The temperature dependence of optical phonon scattering in graphene under strong magnetic field. *J. Phys. Soc. Jpn* **82,** 094606 (2013).
36. Wendler, F., Knorr, A. & Malic, E. Resonant carrier-phonon scattering in graphene under Landau quantization. *Appl. Phys. Lett.* **103,** 253117 (2013).
37. Goerbig, M. O. Electronic properties of graphene in a strong magnetic field. *Rev. Mod. Phys.* **83,** 1193–1243 (2011).
38. Haug, H. & Koch, S. W. *Quantum Theory of the Optical and Electronic Properties of Semiconductors* (World Scientific, 2009).
39. Malic, E. & Knorr, A. *Graphene and Carbon Nanotubes – Ultrafast Relaxation Dynamics and Optics* (Wiley-VCH, 2013).
40. Malic, E., Winzer, T., Bobkin, E. & Knorr, A. Microscopic theory of absorption and ultrafast many-particle kinetics in graphene. *Phys. Rev. B* **84,** 205406 (2011).
41. Graham, M. W., Shi, S. F., Ralph, D. C., Park, J. & McEuen, P. L. Photocurrent measurements of supercollision cooling in graphene. *Nature Phys.* **9,** 103–108 (2013).
42. Betz, A. C. *et al.* Supercollision cooling in undoped graphene. *Nature Phys.* **9,** 109–112 (2013).
43. Roldán, R., Goerbig, M. O. & Fuchs, J-N. The magnetic field particle-hole excitation spectrum in doped graphene and in a standard two-dimensional electron gas. *Semicond. Sci. Technol.* **25,** 034005 (2010).
44. Ando, T. & Uemura, Y. Theory of quantum transport in a two-dimensional electron system under magnetic fields. I. Characteristics of level broadening and transport under strong fields. *J. Phys. Soc. Jpn* **36,** 959–967 (1974).
45. Sprinkle, M. *et al.* First direct observation of a nearly ideal graphene band structure. *Phys. Rev. Lett.* **103,** 226803 (2009).

Acknowledgements

Support from the German Science Foundation DFG in the framework of the Priority Program 1459 Graphene is acknowledged. E.M. and F.W. are grateful to the Einstein Foundation Berlin. The research at the free-electron laser FELBE was supported by the European Community's Seventh Framework Programme (FP7/2007–2013) under Grant agreement No. 226716. Part of this work has been supported by the ERC-2012-AdG-320590 MOMB project as well as the EC Graphene Flagship. We are grateful to P. Michel and the FELBE team for their dedicated support. The Grenoble group acknowledges fruitful discussions with D. M. Basko.

Author contributions

S.W., M.M., M.H., M.O. and M.P. conceived the experiments; M.M. performed the experiments, partly together with M.O. and S.W.; M.M., S.W., H.S. and M.H. analysed and interpreted the data; F.W., E.M. and A.K. developed the microscopic theoretical model. M.O. and M.P. originated the considerations for critical level occupation described in the Supplementary Methods. C.B. and W.A.d.H. prepared the samples; S.W. and E.M. wrote the paper with major input and edits from M.H. All authors discussed the results and commented on the manuscript.

Additional information

Supplementary information is available in the online version of the paper. Reprints and permissions information is available online at www.nature.com/reprints. Correspondence and requests for materials should be addressed to M.M. or S.W.

Competing financial interests

The authors declare no competing financial interests.

NANO LETTERS
Letter
pubs.acs.org/NanoLett

Printing Nearly-Discrete Magnetic Patterns Using Chemical Disorder Induced Ferromagnetism

Rantej Bali,*[†,‡] Sebastian Wintz,[†,§] Falk Meutzner,[†,∥] René Hübner,[†] Richard Boucher,[∥] Ahmet A. Ünal,[⊥] Sergio Valencia,[⊥] Andreas Neudert,[†] Kay Potzger,[†] Jürgen Bauch,[∥] Florian Kronast,[⊥] Stefan Facsko,[†] Jürgen Lindner,[†] and Jürgen Fassbender[†,§]

[†]Institut für Ionenstrahlphysik und Materialforschung, Helmholtz-Zentrum Dresden-Rossendorf, D-01328 Dresden, Germany
[‡]School of Physics, University of Western Australia, 35 Stirling Highway, Crawley WA 6009, Perth, Australia
[§]Institut für Festkörperphysik and [∥]Institut für Werkstoffwissenschaft, Technische Universität Dresden, Helmholtzstrasse 10, D-01069 Dresden, Germany
[⊥]Helmholtz-Zentrum Berlin für Materialien und Energie, Albert-Einstein-Strasse 15, D-12489 Berlin, Germany

Supporting Information

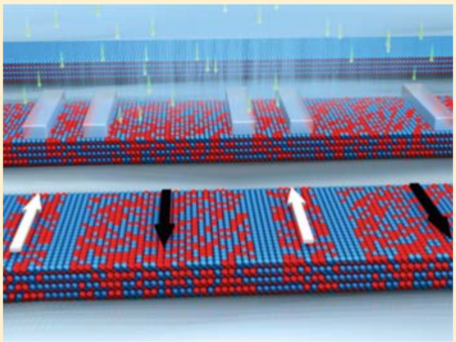

ABSTRACT: Ferromagnetism in certain alloys consisting of magnetic and nonmagnetic species can be activated by the presence of chemical disorder. This phenomenon is linked to an increase in the number of nearest-neighbor magnetic atoms and local variations in the electronic band structure due to the existence of disorder sites. An approach to induce disorder is through exposure of the chemically ordered alloy to energetic ions; collision cascades formed by the ions knock atoms from their ordered sites and the concomitant vacancies are filled randomly via thermal diffusion of atoms at room temperature. The ordered structure thereby undergoes a transition into a metastable solid solution. Here we demonstrate the patterning of highly resolved magnetic structures by taking advantage of the large increase in the saturation magnetization of $Fe_{60}Al_{40}$ alloy triggered by subtle atomic displacements. The sigmoidal characteristic and sensitive dependence of the induced magnetization on the atomic displacements manifests a sub-50 nm patterning resolution. Patterning of magnetic regions in the form of stripes separated by ~40 nm wide spacers was performed, wherein the magnet/spacer/magnet structure exhibits reprogrammable parallel (↑/spacer/↑) and antiparallel (↑/spacer/↓) magnetization configurations in zero field. Materials in which the magnetic behavior can be tuned via ion-induced phase transitions may allow the fabrication of novel spin-transport and memory devices using existing lateral patterning tools.

KEYWORDS: *Phase-transitions, chemical disorder, magnetic patterning, magnetic nanostructures, memory devices*

Fabrication of highly resolved magnetic objects is of vital importance for the functioning of devices such as patterned data storage media and magnetoresistive random access memories (MRAMs). Continued increase of data storage capacity may depend on the ability to fabricate magnetic nanoelements on large wafers using commercially viable processes. A route to large-area patterning of magnetic nanostructures is the localized exposure of materials to accelerated ions, where the magnetic properties of regions selectively exposed are modified.[1−3] Typically, irradiation with ions causes disorder within the material and this modifies parameters such as magnetic anisotropy axes,[4] switching fields,[5] magnetic damping,[6−8] and interlayer exchange coupling.[8−11] Modulation of these secondary parameters may not be sufficient to fabricate, for instance, spin-transport devices where it is crucial to decouple neighboring ferromagnetic regions with narrow nonmagnetic spacers. Therefore, it is essential to obtain materials in which large variation of intrinsic properties such as the saturation magnetization (M_s) is possible at high lateral resolution.

Ion-induced modification of M_s usually occurs through suppression of the magnetic phase and can be achieved by destroying the structure through large atomic displacements,[12] alloying with the ion species,[13−15] or amorphization by intermixing with a cap layer.[16] These destructive processes require excessively high ion-fluences (typically ~10^{16}−10^{18} ions cm^{-2}) and may result in the formation of magnetic inhomogeneities, thereby lowering the resolution of patterning.[17] Furthermore, the destructive process hinders the use of a focused ion-beam as a stylus for direct writing of magnetic patterns. Some processes can be nondestructive, for instance, where the incident ions chemically react with the material to form ferromagnetic phases locally, however, owing to

Received: August 27, 2013
Revised: December 23, 2013
Published: December 30, 2013

stoichiometric reasons large ion fluences may be required.[18] In certain alloys, ferromagnetism can be induced by increasing chemical disorder,[19,20] a property that could be ideal for writing magnetic patterns using ions. However, these systems have yet to be exploited for high-resolution patterning, partly due to the insufficient sensitivity of the induced magnetization on the disorder. In all types of ion-induced modifications, ions penetrate a material in a quasi-Gaussian distribution that could translate into a depth-varying magnetization. Ions are also scattered laterally, causing modifications to the material underneath a shadow-mask, thereby blurring the intended magnetic pattern and imposing a limit on the patterning resolution.

In this Letter, we demonstrate sub-50 nm resolution magnetic patterning by employing a chemically ordered $Fe_{60}Al_{40}$ alloy, in which the M_s is drastically increased via ion-induced disordering. The increase in M_s is attributable to an increase in the Fe−Fe nearest neighbors (n-ns) due to disorder. We show that relatively few displacements of Fe and Al atoms are sufficient to increase the saturation magnetization by a factor of 40. This sensitivity of the induced magnetization to the atomic displacements implies that homogenously magnetized regions can be obtained using fewer ions ($\sim 10^{14}$ ions cm^{-2}), as compared with destructive or chemically reactive processes. Furthermore under the given ion-energy and -fluence conditions, the homogeneously magnetized objects can be obtained with limited lateral scattering; restriction of lateral scattering significantly enhances the patterning resolution, that is the closest lateral distance at which neighboring magnetic objects can be placed while maintaining magnetic isolation.

High-resolution magnetic patterning is proven experimentally by the fabrication of magnetically decoupled stripes separated by 40 nm wide spacers on a $Fe_{60}Al_{40}$ wire. The decoupling enables the stabilization of binary magnetic states, that is, parallel and antiparallel moment configurations of neighboring stripes in remnant fields. The existence of binary magnetic states is prerequisite for the operation of spin-valves and is obtained in a device with narrow cross-section. Spin-transport devices require narrow cross sections for achieving high-current densities. Devices with narrow cross sections are usually fabricated vertically in the form of multilayered pillar structures that require complicated process steps and are difficult to electrically contact. Achieving the so-called "current-perpendicular-to-plane" (CPP) geometry within two lateral patterning steps could greatly simplify the fabrication of spin-transport devices. Moreover, materials exhibiting disorder-induced ferromagnetism may also be highly suited for stylus-like writing of prototype devices using focused ion beams or for large-area printing of magnetic device architectures with a broad beam. The lithography and implantation tools necessary for these processes may already exist in semiconductor foundries.

Ion-induced ferromagnetism in $Fe_{60}Al_{40}$ has so far been studied on sheets of ~300 μm thicknesses.[21−23] At this thickness, incident ions cannot be made to fully penetrate the bulk-like material, ruling out the possibility of transport devices. Furthermore, the untransformed chemically ordered bulk material causes a large background signal, which interferes with the structural and magnetic property characterization of the disordered regions. In ref 21, the disordering effect of Ga^+ ions from a focused ion beam was used to write magnetic dots of ~100 nm diameter at a separation of 500 nm; this large separation prevents any estimate of the ultimate patterning resolution. Here, a systematic study of the effect of chemical disorder on thin films of $Fe_{60}Al_{40}$ with partial and full penetration by ions has been used to build a semiempirical model from which the effect of inhomogeneous depth penetration and lateral scattering of ions on the induced magnetization can be estimated.

While ion-irradiation is an attractive technique for the fabrication of devices, it can suffer from problems such as inhomogeneous depth penetration and lateral scattering. Because of these difficulties, previous literature does not unambiguously show that ion-irradiation can be used to fabricate discrete magnetic nanostructures at high resolution. In contrast, we present a method for achieving highly resolved magnetic structures and provide direct proof for their existence. We begin by showing the effect of chemical disordering on the ferromagnetic properties of thin $Fe_{60}Al_{40}$ films.

Chemical Disorder and Magnetic Properties. In $Fe_{60}Al_{40}$ alloys, the chemically ordered simple cubic B2 (CsCl) phase (space group 221) is paramagnetic whereas the disordered, body-centered cubic A2 phase (space group 229) is ferromagnetic.[24−26] The structure of chemically ordered Fe−Al is schematically shown in Figure 1. The chemically ordered structure consists of planes of pure Fe separated by planes consisting of Al and the remaining Fe atoms. Each atom has 8 n-ns: the Fe atoms in the Al-rich planes have 8 n-ns of Fe and those in the pure-Fe planes have on average 1.6 Fe n-ns, making an average of 2.67 Fe−Fe n-ns in the chemically ordered structure. The Fe−Fe n-ns increase to 4.8 for the disordered structure where the Fe and Al atoms are randomly arranged. This increase in Fe−Fe n-ns is crucial for setting up exchange coupling and inducing ferromagnetism.[27−35] Chemical disorder can be induced by ions possessing sufficient energy to knock Fe and Al atoms from their ordered sites. The vacancies formed in this process are filled with random occupancy due to thermal diffusion at room temperature, resulting in the B2→A2 phase transition.

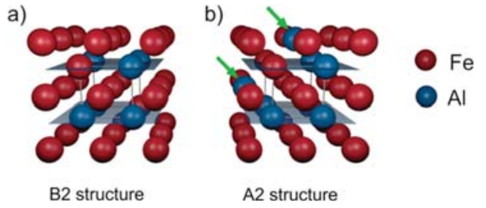

Figure 1. (a) Schematic structure of chemically ordered (B2) Fe−Al, where pure-Fe planes separate Al-rich planes. (b) The disordered (A2) structure showing the occurrence of Al sites in the initially pure-Fe planes, indicated by the arrows.

The effect of ion-induced disorder is seen in the magnetic hysteresis loops of Figure 2a. Hysteresis loops were measured using a vibrating sample magnetometer (VSM) on $Fe_{60}Al_{40}$ films of 40 nm nominal thickness, deposited on SiO_2(150 nm)/Si(001) substrates. The films were annealed at 773 K in vacuum to induce chemical ordering. Figure 2a shows that the annealed sample is weakly ferromagnetic with a saturation magnetization of M_s = 20 kA m^{-1}.

The chemically ordered samples were irradiated with 6×10^{14} ions cm^{-2} of Ne^+-ions at 10 and 30 keV respectively. According to simulations, ion-induced displacements of atoms follow a Gaussian-like distribution with the peaks located at

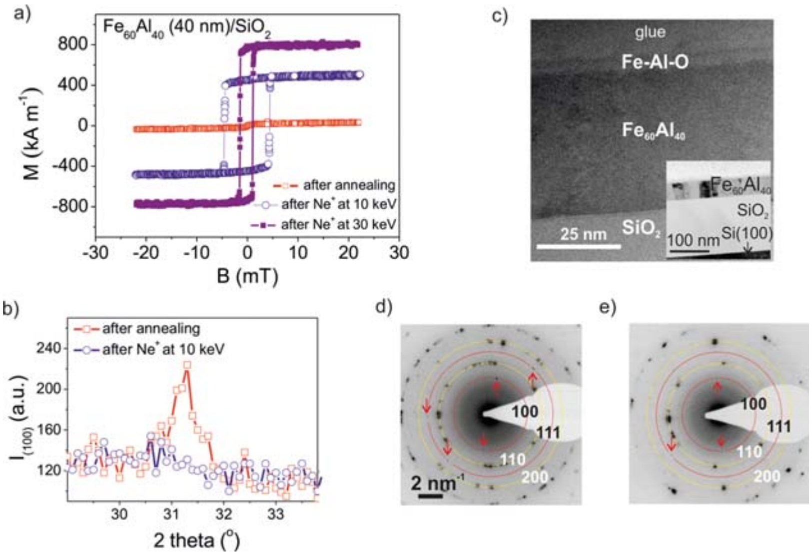

Figure 2. (a) Magnetic hysteresis loops for $Fe_{60}Al_{40}$ films of 40 nm thickness measured after vacuum annealing at 773 K (squares) and after irradiation of the annealed films with Ne^+ at 10 (circles) and 30 keV (solid squares). A fluence of 6×10^{14} ions cm^{-2} was used for the above irradiation exposures. (b) The 100 superstructure reflection obtained using X-ray diffraction for the sample after annealing and subsequent irradiation with Ne^+ at 10 keV. (c) Cross-sectional high-resolution transmission electron microscopy image of the sample irradiated with 10 keV Ne^+. (d) Selected area electron diffraction pattern of the $Fe_{60}Al_{40}$ film after annealing and (e) after 10 keV Ne^+ irradiation. Concentric circles mark the 100 and 111 superstructure reflections (red) and 110 and 200 reflections (yellow). Arrows indicate the observed superstructure reflections.

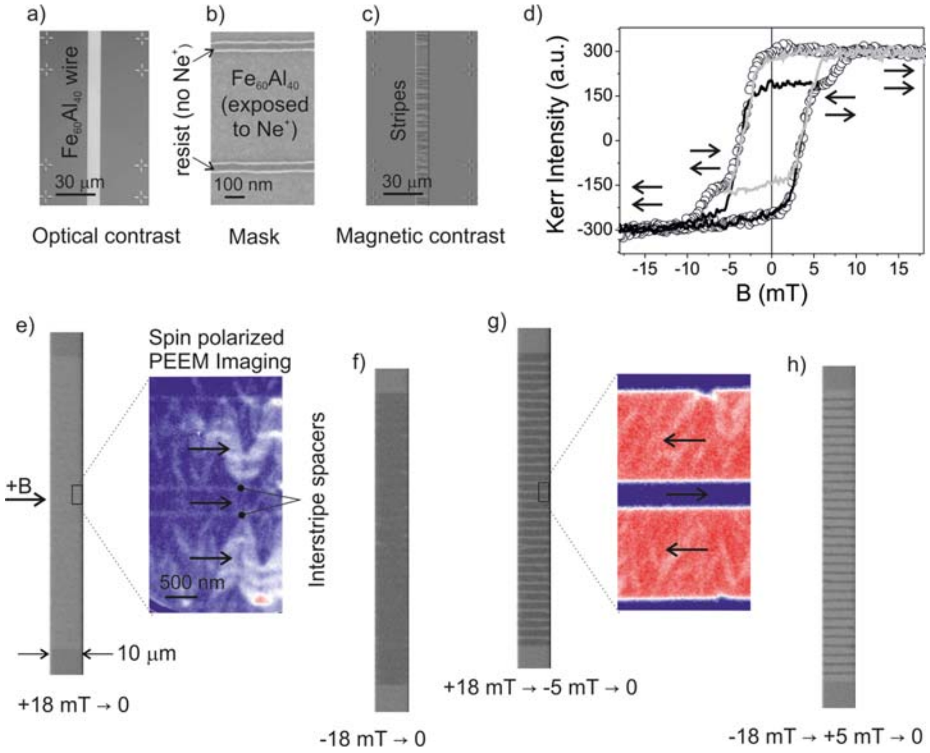

Figure 3. (a) Optical micrograph of the $Fe_{60}Al_{40}$ wire of 10 μm width. (b) Scanning electron microscopy image of the wire surface with the resist mask. (c) Magnetic contrast obtained using Kerr microscopy showing the presence of ferromagnetic stripes. (d) Major hysteresis loop (circles) and partial hysteresis loops (lines) measured on a set of 32 pairs of magnetic stripes, with widths 0.5 μm and 2 μm respectively, formed due to chemical disorder induced by 10 keV Ne^+ ions. The individual magnetic stripes are separated by weakly-magnetic regions of ∼40 nm width. The spacers are formed due to the stopping of Ne^+ ions by the resist mask shown in (b). (e−h) Magnetic contrast in the 10 μm wide wires corresponding to remnant points of the hysteresis loops shown in (d). Higher-resolution SPEEM images obtained after applying the same field history as in (d) are shown as magnifications of (e,g).

depths of 8.5 and 17 nm for Ne^+ impinging at 10 and 30 keV, respectively.[36] The effect of ion-induced disorder is clearly seen in the magnetic hysteresis, where $\langle M_s \rangle$ increases to 480 and 780 kA m^{-1}, respectively, for the 10 and 30 keV samples.[37] The M_s of the 30 keV Ne^+ sample is a factor of 40 larger than that of the annealed sample.

The magnetic behavior can be correlated to the chemical ordering. Figure 2b shows X-ray diffraction measurements around the 100 reflection for the sample after annealing and after subsequent 10 keV Ne^+-irradiation. The 100 reflection is allowed for the B2 superstructure but vanishes for the disordered A2 phase. The annealed $Fe_{60}Al_{40}$ film possessing low M_s shows a clear superstructure reflection whereas this reflection vanishes for the 10 keV sample possessing higher M_s.

A microscopic characterization of the film structure was obtained using cross-sectional high-resolution transmission electron microscopy (TEM). Figure 2c shows a TEM cross-section for the 10 keV sample. The actual $Fe_{60}Al_{40}$ thickness was close to 40 nm covered with a 4 nm thick continuous oxide layer. The well-defined substrate−film interface region suggests that possible intermixing with the SiO_2 buffer layer due to annealing and irradiation is negligible. The film surface was found to be smooth, pointing to negligible sputtering by the Ne^+ ions. Selected area electron diffraction (SAED) patterns are shown in Figure 2d,e for the annealed and 10 keV Ne^+ samples, respectively. In Figure 2d, the SAED pattern of the annealed sample matches that of B2 phase $Fe_{60}Al_{40}$.[38] The superstructure reflections either vanish or are of lowered intensity on the 10 keV Ne^+ irradiated sample (Figure 2e). The low intensity reflections suggest that some residual chemical order is retained despite exposure to 10 keV Ne^+. This is also consistent with the lower $\langle M_s \rangle$ of the 10 keV Ne^+ irradiated sample, which is not fully magnetized, and the fact that induced M_s increases further for 30 keV irradiation.

Thus ion-induced chemical disorder causes a significant increase of M_s in initially ordered $Fe_{60}Al_{40}$ thin films. Next, we attempt to localize the chemical disorder for fabricating magnetic structures into topographically flat films and to investigate the limits on the patterning resolution in the presence of lateral scattering of ions.

Patterning of Reprogrammable Magnetic Structures. Magnetic patterning was performed on a 10 μm wide and 400 μm long wire of chemically ordered $Fe_{60}Al_{40}$ (Figure 3a). The wire was covered with a 150 nm thick resist layer and patterned using e-beam lithography. TRIM simulation showed that the 150 nm thick resist layer is sufficient to block impinging 10 keV Ne^+-ions.

Lithography was used to carve out stripe like openings of 0.5 and 2 μm widths. As shown in the micrograph in Figure 3b, the stripe-openings were separated by ~40 nm wide (and 150 nm high) resist walls, thereby stopping the impinging Ne^+ ions reaching the areas directly underneath the resist. These areas can be expected to retain chemical order after exposure to Ne^+, however, only if the lateral scattering of ions is restricted. The wire covered by the shadow-mask was exposed to 10 keV Ne^+-ions at a fluence of 6×10^{14} ion cm^{-2}. Figure 3c shows the magnetic contrast image, obtained using Kerr Microscopy on the sample prior to application of saturating magnetic fields. Striped regions are clearly observed possessing random magnetic orientations.

Magnetic contrast was captured while sweeping the field to obtain hysteresis loops shown in Figure 3d on a set of 32 (0.5 μm/spacer/2 μm/spacer) stripe-pairs. Magnetic field, B, was applied perpendicular to the wire, that is, parallel to the 10 μm long edge of the ferromagnetic stripes. Magnetization reversal occurs via a two-staged process; the first reversal step occurs at ~±3 mT and the second step at ~±7 mT. The magneto-optic intensity changes by 80% in the first reversal step, indicating that the 2 μm wide stripes reverse collectively at the smaller field. In the stripe geometry, the internal demagnetizing field increases with the stripe width. Reversal of the 2 μm wide stripes therefore occurs at smaller externally applied field as compared with the 0.5 μm stripes, resulting in selective reversal.

To further test the selective reversal behavior, partial hysteresis loops were recorded, that is, the stripes were saturated in one direction at a field of ±18 mT, subsequently the field was swept to a small reverse field of ∓5 mT and finally returned to ±18 mT. As seen in Figure 3d, partial loops do not exhibit the second reversal stage, since after saturation the reversal fields for the 0.5 μm stripes were not reached; and the partial loops selectively reversed the 2 μm wide stripes. In the saturated state, the stripe magnetizations are aligned parallel, and after the first reversal step of the 2 μm wide stripes the stripe magnetizations are antiparallel (indicated by the arrows in Figure 3d).

Magnetic contrast images were captured at remnant points of the above hysteresis loops and are shown in Figure 3e−h. Stripes with magnetization pointing towards the left or right appear as dark and bright contrast, respectively. Images captured after applying the saturating field of ±18 mT followed by reduction to zero field show that the parallel magnetization configuration is preserved in remanence (Figure 3e,f). The antiparallel configuration is obtained after applying a reverse field of ∓5 mT to the saturated stripes and returning to zero field. Figure 3g,h shows alternating light and dark contrast of the antiparallel state in remnant fields.

Thus, parallel and antiparallel magnetization configurations can be programmed using the magnetic field history and are nonvolatile, that is, stable when the field is switched off. Selective reversal and the existence of binary magnetic states viz., (↑↑), (↑↓), (↓↑), and (↓↓) is a prerequisite for spin-valves and advantageous in devices for storing data bits. In particular with respect to spin-transport devices, it is also necessary to ensure that the magnetic regions are separated by narrow spacers of zero or low magnetization. In order to prove the existence of the spacer, spin-resolved photo-emission electron microscopy (SPEEM) measurements that can achieve a spatial resolution below 50 nm were undertaken.

X-ray Magnetic Imaging. Magnetic contrast was obtained by illuminating the sample with circularly polarized X-rays at the energy corresponding to the Fe L_3 resonance. X-ray magnetic circular dichroism (XMCD), that is, the difference of two images taken with opposite helicity provides a measure of the magnetization component along the photon incidence direction. The direction of incidence was aligned parallel to the 10 μm long edge of the magnetic stripes.

The SPEEM micrographs are shown in Figure 3e,g as magnified equivalent regions of the Kerr-images. The color scale varies from red to blue for magnetic moments pointing left or right respectively. Straight, low-contrast regions are found to separate the 500 nm and 2 μm wide high-contrast regions that correspond to the magnetic stripes. Within the stripes, a substructure of meandering low-contrast regions are observed. These low-contrast regions (Figure 3e) tend to become broader at the wire-edge and narrower toward the center and are prominent only in the parallel configuration.

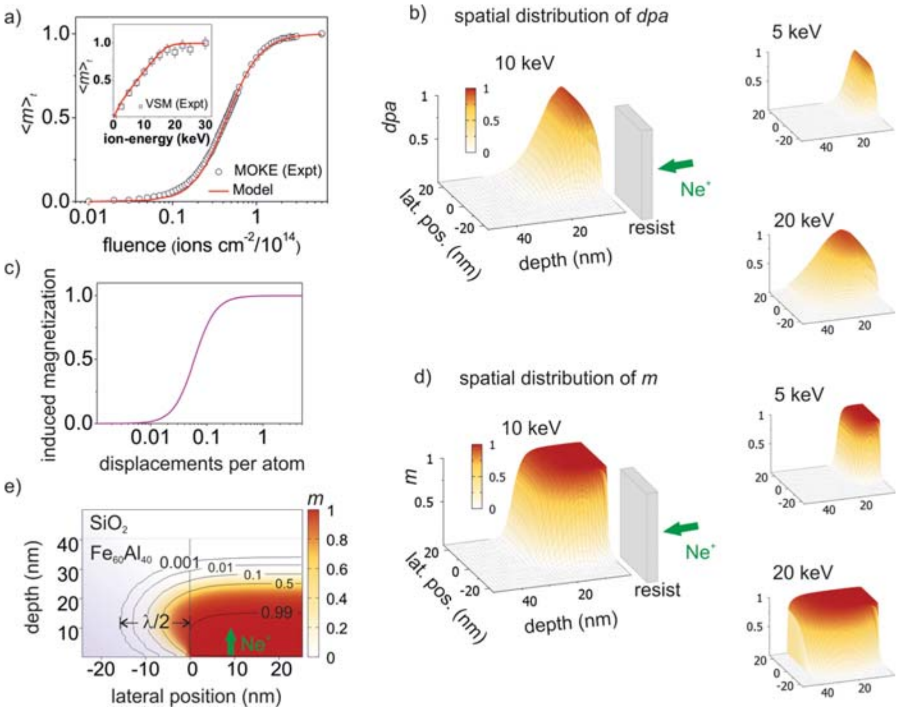

Figure 4. (a) Variation of average magnetization $\langle m \rangle_t$ with Ne^+ fluence at 20 keV, and (inset of a) $\langle m \rangle_t$ variation with ion-energy at a fluence of 6×10^{14} ions cm^{-2}. Red lines show the semiempirical data fitting. (b) Simulations showing the spatial-distribution of the displacements per atom, dpa, in the vicinity of a mask, for Ne^+ at energies of 5, 10, and 20 keV and a fluence of 6×10^{14} ions cm^{-2}. (c) Variation of induced magnetization m with dpa, calculated from the semiemprical model. (d) Spatial-distribution of m in the vicinity of a mask for the dpa-distributions shown in (b). (e) Projection of m on the cross-sectional plane of the film for the 10 keV sample. The mask covers the lateral region between 0 and −25 nm, and λ is the resolution of magnetic patterning.

These regions nearly vanish in the antiparallel configuration, that is, they respond to the magnetic field. Therefore the meandering substructure likely corresponds to domains where the moments exhibit a large perpendicular component relative to the magnetic stripes, in order to minimize the stray field. The straight low-contrast regions, however, are unresponsive to the magnetic field and occur for both parallel and antiparallel states. Because the straight low-contrast lines also exactly follow the pattern of the shadow mask, it can be concluded that these lines correspond to the 40 nm wide unirradiated regions. Neighboring 500 nm and 2 μm wide ferromagnetic stripes are therefore isolated by a continuous weakly magnetic spacer of 40 nm nominal width.

Lateral scattering of ions however may penetrate the region underneath the 40 nm wide masks and further narrow the spacer regions. We attempt to estimate the extent of this effect through a semiempirical approach, and study its consequences on the patterning resolution.

Semiempirical Modeling and Discussions. The problem of estimating the magnetization induced due to the lateral scattering and inhomogeneous depth penetration of ions is approached by first relating the normalized increase of magnetization, m, to the average displacements undergone by an atom during the irradiaton process, that is, displacements per atom (dpa). A B2→A2 transition occurring within a limited set of atoms with coexisting phases can be modeled by a sigmoidal function.

The above hypothesis can be tested by observing the dependence of m on the fluence. A fluence gradient was obtained by making 20 keV Ne^+ ions incident on the sample while blanking the ion-beam at a known rate using a mechanized shutter. In this way, the fluence was varied between 0 and 6×10^{14} ions cm^{-2}. A polarized laser spot was scanned along the fluence gradient and the m averaged over the probe depth, $\langle m \rangle_t$, was measured using the magneto-optical Kerr effect (MOKE). Figure 4a shows a clear sigmoidal variation of $\langle m \rangle_t$ with the ion-fluence, and because fluence is proportional to dpa it confirms the validity of an s-shaped fitting curve.

The dpa caused by ions of a given energy can be calculated using the binary collision approximation. Simulations performed using the TRIM program reveal that Ne^+ ions at 20 keV can cause ∼320 displacements per ion, and the corresponding value for 5 and 10 keV are 98 and 185, respectively. The calculated spatial variation of dpa for Ne^+ ions impinging on 40 nm thick $Fe_{60}Al_{40}$ films irradiated through a mask at energies of 5, 10, and 20 keV and fluence of 6×10^{14} ions cm^{-2} are shown in Figure 4b.

In the case of uniform irradiation, the dpa will remain constant in lateral position, x. The presence of a mask causes a variation of dpa in x. This was simulated by setting the mask edge at $x = 0$, such that no ions are incident for $x < 0$. Atomic displacements may still occur in regions where $x < 0$ purely due to lateral scattering. Moving away from the mask edge in the positive direction, dpa gradually increases finally reaching the constant value for uniform irradiation. As seen in Figure 4b, dpa varies in a quasi-Gaussian form with the film depth, t. The dpa(t) at $x = +25$ nm is identical to that for a uniformly irradiated film.

The dpa(t) calculated for uniformly irradiated films will be used to fit the fluence variation shown in Figure 4a. An equation describing a sigmoid with m varying between 0 and 1 will be used to simulate the data; because the measurements are an average over the probe depth, it is necessary to integrate from the surface at $t = 0$, to the probe depth $t = t_i$ (ref 39)

$$\langle m \rangle_t = \frac{1}{t_i} \int_{t_i}^{0} \left(\frac{\mathrm{dpa}(t)}{\mathrm{dpa}_0} \right)^p \left[1 + \left(\frac{\mathrm{dpa}(t)}{\mathrm{dpa}_0} \right)^p \right]^{-1} \mathrm{d}t \tag{1}$$

where dpa_0 is the dpa at which m equals 0.5 and p is related to the slope of the quasi-linear region of the sigmoid. For $\mathrm{dpa}_0 = 0.06$ and $p = 2.3$, the semiempirical model fits the fluence-variation of $\langle m \rangle_t$ shown in Figure 4a. The sigmoidal m(dpa) variation obtained by the above model is shown in Figure 4c.

The model can be cross-checked by fitting the variation of $\langle m \rangle_t$ with the ion-energy. The inset of Figure 4a shows that the same parameters also fit the variation of $\langle m \rangle_t$ with the ion-energy. Increasing the ion-energy results in deeper penetration of the ions and above a threshold the ions fully penetrate the film and maximum $\langle m \rangle_t$ can be achieved. Figure 4a shows that the given 40 nm thick $\mathrm{Fe_{60}Al_{40}}$ films can be fully penetrated by 20 keV $\mathrm{Ne^+}$-ions.

The semiempirical model can now be applied to the spatial distribution of dpa shown in Figure 4b, to obtain the spatial variation of m in the vicinity of a mask-edge. The m-spatial distributions are shown in Figure 4d and reveal nearly discrete magnetic elements, where the depth and lateral penetration of the magnetized regions depends on the ion-energy. These plots can be used to estimate the lateral resolution of patterning, λ.

We define λ as the minimum lateral spacing between two magnetic objects, while keeping $m < 0.001$ within the spacer region. Figure 4e shows the lateral projection of the m-spatial distribution for the 10 keV $\mathrm{Ne^+}$ sample, with the projection of m shown in color code and contour lines showing $m = 0.001$ to 0.99. It is seen that $m = 0.99$ is achieved directly underneath the mask edge and can be considered as the edge of the magnetic element. The lateral distance between the $m = 0.99$ and 0.001 contour lines then corresponds to $\lambda/2$. The conservative estimates of λ for 5, 10, and 20 keV $\mathrm{Ne^+}$ ions are 18, 31, and 47 nm respectively.[40]

The 31 nm resolution calculated for 10 keV $\mathrm{Ne^+}$ ions is consistent with the results in Figure 3 where separation between magnetic stripes was realized using an ~40 nm wide shadow mask. Varying the ion-energy provides depth control of the magnetic element. With 20 keV $\mathrm{Ne^+}$ ions, full depth penetration and sub-50 nm patterning resolution can be achieved. Note that the lateral penetration of ions does not necessarily limit the patterning resolution and can instead be exploited for patterning spacers that are narrower than the lithographed mask.

The present estimate of sub-50 nm patterning resolution is based on a semiempirical approach that considers the effect of lateral scattering of ions and has been confirmed through direct observation. Furthermore, the patterning resolution has been defined rather conservatively, requiring that the increase in magnetization at the center of the spacing between two magnetic objects is restricted to 1 part in 1000. A more conventional definition, analogous to photolithography, may require the magnetization increase at the spacing center to be restricted to half the maximum M_s, and as seen in Figure 4e the resolution in this case falls within the sub-10 nm range.

The high lateral patterning resolution originates from the sensitive dependence of the induced magnetization on the atomic displacements. The sensitive dependence seen in Figure 4c allows the tail regions of the quasi-Gaussian dpa variation to achieve maximum M_s, leading to the high definition of magnetic elements. The reason for the sensitivity of the phase transition to the ion-fluence lies in the fact that each ion can cause ~100 atomic displacements. Thus, a relatively small number of ions are sufficient to cause substantial changes to the local environment of the moment carrying Fe atoms.

A first approximation of the disorder induced variation in the Fe−Fe n-ns can be made by assuming 100% efficiency in recombination of vacancies (formed due to atomic displacements) with thermally diffusing atoms. In Figure 4c, it is seen that $m = 0.99$ is induced for dpa = 0.5. Assuming the probability of vacancy recombination with an Fe atom to be the same as the atomic fraction (=0.6), it can be seen that random displacement of half the atoms causes the Fe−Fe n-ns to increase to 3.6, thereby inducing 99% of the magnetization. This is consistent with reports, where the Fe−Fe n-ns were controlled by varying the composition of Fe−Al alloys and majority of the M_s was induced as the Fe−Fe n-ns increased from 3 to 4.[27] Furthermore, the magnetic moment per Fe-atom (estimated from Figure 2a) in the chemically ordered state is 0.04 μ_B and it increases to 1.67 μ_B for the disordered state, which is close to the 1.8 μ_B predicted from calculations.[31] Ion-induced disorder in thin films could provide a way to directly observe the effect of purely varying the nearest neighbor interactions on, for instance, the spin and orbital contributions to the net magnetic moment, thereby shedding light on the mechanism of disorder induced ferromagnetism.

Conclusions. We show that sub-50 nm ion-induced lateral patterning of magnetic structures can be enabled by disorder-induced ferromagnetism, where the induced magnetization sensitively depends on the chemical disorder. Nearly discrete magnetic elements can be embedded within atomically flat films and can be made to partially or fully penetrate the film depth. The highly discrete magnetic resolution and the fine-tunability of magnetic properties may enable novel spin-transport and spin-wave devices. The semiempirical model shows that resolution can be sufficiently high such that the separation between the embedded magnetic objects can approach the spin-diffusion length of some materials, potentially making laterally patterned spin-transport devices viable. Ion-induced disorder can also provide a powerful way to modulate the M_s of certain materials with nanoscale periodicity.[41] Periodic magnetic structures may be fabricated using interference of femtosecond laser beams, to cause localized annealing of chemically disordered films at points of constructive intereference.[42] Showing that discrete magnetic nanostructures can be prepared using disorder induced ferromagnetism has important consequences not previously considered in literature, such as the possibility of laterally patterned spin-transport devices; our results are a step in this direction. These results may spur the search for new materials possessing disorder induced ferromagnetism for the local manipulation of magnetic properties.

■ ASSOCIATED CONTENT

Ⓢ Supporting Information

Further details on the experimental methods used as well as the TRIM simulations is available. This material is available free of charge via the Internet at http://pubs.acs.org.

AUTHOR INFORMATION

Corresponding Author

*E-mail: rantej@gmail.com, r.bali@hzdr.de.

Notes

The authors declare no competing financial interest.

ACKNOWLEDGMENTS

We thank Andreas Henschke, Franziska Nierobisch, Ingolf Winkler, Andrea Scholz, Joachim Wagner, Annette Kunz, Martina Mißbach, and Claudia Neisser for technical support. The experimental work was financed by the in-house funding of the Institute of Ion Beam Physics and Materials Research, (Helmholtz-Zentrum Dresden-Rossendorf e.V.). R.B. acknowledges the Australian Post-Doctoral Fellowship from the Australian Research Council through Grant DP110103980.

ABBREVIATIONS

CPP, current perpendicular to plane; dpa, displacements per atom; m, induced magnetization (normalizd); M_s, saturation magnetization; MOKE, magneto-optic Kerr effect; MRAMs, magnetoresistive random access memories; n-ns, nearest-neighbors; SAED, selected area electron diffraction; SPEEM, spin-polarized photo emission electron microscopy; TEM, transmission electron microscopy; TRIM, transport of ions in matter

REFERENCES

(1) Fassbender, J.; McCord, J. *J. Magn. Magn. Mater.* **2008**, *320*, 579.

(2) Fassbender, J.; Ravelosona, D.; Samson, Y. *J. Phys. D* **2004**, *37*, R179.

(3) Baglin, J. E. E. *Appl. Surf. Sci.* **2012**, *258*, 4103.

(4) Chappert, C.; Bernas, H.; Ferré, J.; Kottler, V.; Jamet, J.-P.; Chen, Y.; Cambril, E.; Devolder, T.; Rousseaux, F.; Mathet, V.; Launois, H. *Science* **1998**, *280* (5371), 1919.

(5) McCord, J.; Gemming, T.; Schultz, L.; Fassbender, J.; Liedke, M. O.; Frommgerger, M.; Quandt, E. *Appl. Phys. Lett.* **2005**, *86*, 162502.

(6) Fassbender, J.; McCord, J. *Appl. Phys. Lett.* **2006**, *88*, 252501.

(7) Barsukov, I.; Römer, F. M.; Meckenstock, R.; Lenz, K.; Lindner, J.; Hemken to Krax, S.; Banholzer, A.; Körner, M.; Grebing, J.; Fassbender, J.; Farle, M. *Phys. Rev. B* **2011**, *84*, 140410(R).

(8) Obry, B.; Pirro, P.; Brächer, T.; Chumak, A. V.; Osten, J.; Ciubotaru, F.; Serga, A. A.; Fassbender, J.; Hillebrands, B. *Appl. Phys. Lett.* **2013**, *102*, 202403.

(9) Demokritov, S. O.; Bayer, C.; Poppe, S.; Rickart, M.; Fassbender, J.; Hillebrands, B.; Kholin, D. I.; Kreines, N. M.; Liedke, O. M. *Phys. Rev. Lett.* **2003**, *90*, 097201.

(10) Höink, V.; Schmalhorst, J.; Reiss, G.; Weis, T.; Lengemann, D.; Engel, D.; Ehresmann, A. *J. Appl. Phys.* **2008**, *103*, 123903.

(11) Wintz, S.; Bunce, C.; Banholzer, A.; Körner, M.; Strache, T.; Mattheis, R.; McCord, J.; Raabe, J.; Quitmann, C.; Erbe, A.; Fassbender, J. *Phys. Rev. B* **2012**, *85*, 134417.

(12) Hellwig, O.; Weller, D.; Kellock, A. J.; Baglin, J. E. E.; Fullerton, E. E. *Appl. Phys. Lett.* **2001**, *79*, 1151.

(13) Vogel, A.; Wintz, S.; Gerhardt, T.; Bocklage, L.; Strache, T.; Im, M.-Y.; Fischer, P.; Fassbender, J.; McCord, J.; Meier, G. *Appl. Phys. Lett.* **2011**, *98*, 20250.

(14) McGrouther, D.; Chapman, J. N. *Appl. Phys. Lett.* **2005**, *87*, 022507.

(15) McCord, J.; Schultz, L.; Fassbender, J. *Adv. Mater.* **2008**, *20*, 2090.

(16) Fassbender, J.; Mücklich, A.; Potzger, K.; Möller, W. *Nucl. Instrum. Methods B* **2006**, *248*, 343.

(17) Gaur, N.; Kundu, S.; Piramanayagam, S. N.; Maurer, S. L.; Tan, H. K.; Wong, S. K.; Steen, S. E.; Yang, H.; Bhatia, C. S. *Sci. Rep.* **2013**, *03*, 1907.

(18) Kim, S.; Lee, S.; Ko, J.; Son, J.; Kim, M.; Kang, S.; Hong, J. *Nat. Nanotechnol.* **2012**, *7*, 567.

(19) Maat, S.; Kellock, A. J.; Weller, D.; Baglin, J. E. E.; Fullerton, E. E. *J. Magn. Magn. Mater.* **2003**, *265*, 1.

(20) Zhou, G. F.; Bakker, H. *Mater. Trans., JIM* **1995**, *36*, 329.

(21) Menéndez, E.; Liedke, M. O.; Fassbender, J.; Gemming, T.; Weber, A.; Heyderman, L. J.; Rao, K. V.; Deevi, S. C.; Suriñach, S.; Baró, M. D.; Sort, J.; Nogués, J. *Small* **2009**, *5* (2), 229.

(22) Fassbender, J.; Liedke, M. O.; Strache, T.; Möller, W.; Menéndez, E.; Sort, J.; Rao, K. V.; Deevi, S. C.; Nogués, J. *Phys. Rev. B* **2008**, *77*, 174430.

(23) Varea, A.; Menéndez, E.; Montserrat, J.; Lora-Tamayo, E.; Weber, A.; Heyderman, L. J.; Deevi, S. C.; Rao, K. V.; Suriñach, S.; Baró, M. D.; Buchanan, K. S.; Nogués, J.; Sort, J. *J. Appl. Phys.* **2011**, *109*, 093918.

(24) Zamora, L. E.; Pérez Alcázar, G. A.; Vélez, G. Y.; Betancur, J. D.; Marco, J. F.; Romero, J. J.; Martínez, A.; Palomares, F. J.; González, J. M. *Phys. Rev. B* **2009**, *79*, 094418.

(25) Trautvetter, M.; Wiedwald, U.; Paul, H.; Minkow, A.; Ziemann, P. *Appl. Phys. A: Mater. Sci. Process.* **2011**, *102* (3), 725.

(26) Sort, J.; Concustell, A.; Menéndez, E.; Suriñach, S.; Rao, K. V.; Deevi, S. C.; Baró, M. D.; Nogués, J. *Adv. Mater.* **2006**, *18*, 1717.

(27) (a) Huffman, G. P.; Fisher, R. M. *J. Appl. Phys.* **1967**, *38*, 735. (b) Beck, P. A. *Metall. Trans.* **1971**, *2*, 2015.

(28) Krause, J. C.; Schaf, J.; da Costa, M. I., Jr.; Paduani, C. *Phys. Rev. B* **2000**, *61* (9), 6196.

(29) Wu, D.; Munroe, P. R.; Baker, I. *Philos. Mag.* **2003**, *83*, 295−313.

(30) Wertheim, G. K.; Jaccarino, V.; Wernick, J. H.; Buchanan, D. N. E. *Phys. Rev. Lett.* **1964**, *12*, 24.

(31) Kulikov, N. I.; Postnikov, A. V.; Borstel, G.; Braun, J. *Phys. Rev. B* **1999**, *59* (10), 6824.

(32) Reddy, B. V.; Jena, P.; Deevi, S. C. *Intermetallics* **2000**, *8* (9−11), 1197.

(33) Smirnov, A. V.; Shelton, W. A.; Johnson, D. D. *Phys. Rev. B* **2005**, *71*, 064408.

(34) Bose, S. K.; Drchal, V.; Kudrnovský, J.; Jepsen, O.; Andersen, O. K. *Phys. Rev. B* **1997**, *55* (13), 8184.

(35) Menéndez, E.; Sort, J.; Liedke, M. O.; Fassbender, J.; Suriñach, S.; Baró, M. D.; Nogués, J. *New J. Phys.* **2008**, *10*, 103030.

(36) Simulations were performed using Transport of Ions in Matter (TRIM, see Ziegler, J. F.; Ziegler, M. D.; Biersack, J. P. *Nucl. Instrum. Methods B* **2010**, *268* (11−12), 1818.

(37) For irradiated samples the induced magnetization may vary with the ion penetration depth and therefore the measurement yields an average saturation magnetization, $\langle M_s \rangle$.

(38) ICSD card 165164 based on: Stein, F.; Vogel, S. C.; Eumann, M.; Palm, M. *Intermetallics* **2010**, *18*, 150.

(39) In case of VSM measurements the whole sample is probed and t_i = 40 nm. MOKE is a surface sensitive technique and the laser penetrates only partially through the film thickness. Therefore, the limiting case was considered, where t_i was taken as the depth at which $\langle m \rangle_t$ reaches its maximum. Maximum $\langle m \rangle_t$ occurred for $t_i \approx 20$ nm, which is consistent with the typical light penetration depth in metals; see Qiu, Z. Q.; Bader, S. D. *Rev. Sci. Instrum.* **2000**, *71*, 1243.

(40) Using the $m = 0.001$ contour line provides a conservative estimate for λ; indeed the selective switching shown in Figure 3 is realized despite the existence of the 20 kA m^{-1} residual M_s within the chemically ordered spacer regions, which is a factor of ∼0.025 the 780 kA m^{-1} M_s of the fully disordered regions.

(41) Neusser, S.; Grundler, D. *Adv. Mater.* **2009**, *21*, 2927.

(42) Polushkin, N. I.; Oliveira, V.; Conde, O.; Vilar, R.; Drozdov, Yu. N.; Apolinário, A.; García-García, A.; Teixeira, J. M.; Kakazei, G. N. *Appl. Phys. Lett.* **2012**, *101*, 132408.

PRL **112,** 153201 (2014) PHYSICAL REVIEW LETTERS week ending 18 APRIL 2014

Charge Exchange and Energy Loss of Slow Highly Charged Ions in 1 nm Thick Carbon Nanomembranes

Richard A. Wilhelm,[1,2,*] Elisabeth Gruber,[3] Robert Ritter,[3] René Heller,[1] Stefan Facsko,[1] and Friedrich Aumayr[3]
[1]*Helmholtz-Zentrum Dresden-Rossendorf, Institute of Ion Beam Physics and Materials Research, 01328 Dresden, Germany, EU*
[2]*Technische Universität Dresden, 01069 Dresden, Germany, EU*
[3]*TU Wien - Vienna University of Technology, Institute of Applied Physics, 1040 Vienna, Austria, EU*

(Received 19 November 2013; published 14 April 2014)

Experimental charge exchange and energy loss data for the transmission of slow highly charged Xe ions through ultrathin polymeric carbon membranes are presented. Surprisingly, two distinct exit charge state distributions accompanied by charge exchange dependent energy losses are observed. The energy loss for ions exhibiting large charge loss shows a quadratic dependency on the incident charge state indicating that equilibrium stopping force values do not apply in this case. Additional angle resolved transmission measurements point on a significant contribution of elastic energy loss. The observations show that regimes of different impact parameters can be separated and thus a particle's energy deposition in an ultrathin solid target may not be described in terms of an averaged energy loss per unit length.

DOI: 10.1103/PhysRevLett.112.153201 PACS numbers: 34.35.+a, 34.70.+e, 68.49.Sf, 79.20.Rf

Modern approaches in ion and electron irradiation of solids such as nano-structuring of thin films or even structuring of free-standing monolayers such as graphene [1–3] or MoS_2 [4,5] rely on models for structural and electronic defect formation. Most important for processes during ion-solid interaction is the amount of deposited energy and its dissipation channels [6]. We show that the energy loss and charge exchange of ions in very thin films, such as two-dimensional materials, show significant differences to solids with reduced thickness. The understanding of these differences is not only of importance for ion beam analysis of two-dimensional materials but in particular for manipulating and tailoring their properties. [7].

To probe interaction processes in very thin target materials slow highly charged ions (HCI) are ideal tools due to their energy deposition confinement to shallow surface regions. Besides the well known near-surface potential energy deposition [8,9] also an expected increased preequilibrium kinetic energy loss (stopping force) [10] is confined to a few nm at the surface. In the conventional description of both contributions to the stopping force, i.e., nuclear and electronic stopping, the charge state of an ion is identified with its equilibrium charge state by Bohr's stripping criterion [11,12]. The equilibrium charge state by Bohr is given as $Q_{\mathrm{eq}} = Z^{1/3} v/v_0$ and describes the (average) charge state of an ion passing through a solid at a given velocity v (v_0: Bohr's velocity, Z: nuclear charge of the ion). The charge state Q of slow highly charged ions is much higher than the equilibrium charge state Q_{eq} ($Q_{\mathrm{eq}} \ll Q \lesssim Z$). Therefore, the interaction of HCI with surfaces may not be described in terms of an equilibrium charge state dependent stopping force. Furthermore, due to the localization of the energy deposition slow HCI can be used as an efficient tool for surface nanostructuring [13–24] and tuning of the electrical properties of materials [25], as well as a probe for surface energy deposition processes [26,27].

Recently, it has been shown that slow HCI can create pores in 1 nm thick carbon nanomembranes (CNM) [28,29] mainly by deposition of their potential energy [30]. Here we report on measurements of kinetic energy loss and charge loss of slow highly charged Xe ions transmitted through 1 nm CNM. For carbon foils with larger thicknesses of 5 and 10 nm Schenkel *et al.* found evidence for a charge state dependent stopping force, whereas the total increase was reported to be small (factor 1.5) [31–33] for ions at about 2 keV/amu. This can be attributed to the fact that the equilibrium charge state is reached within the foil thickness and preequilibrium stopping force values may only contribute to a minor extent. In contrast, we observe two *distinct* exit charge state distributions with charge states much higher than the equilibrium charge state and an increase in stopping force with charge state by a factor up to 4, indicating that a 1 nm carbon layer is thin enough to address preequilibrium interaction processes of ions in solids. The two distributions allow a separation of different impact parameter regimes. This implicates that the interaction of particles with ultrathin solid targets may not be described in terms of an "average interaction per unit length."

Highly charged ions are produced in a room-temperature electron beam ion trap [34] at the Ion Beam Center of the Helmholtz-Zentrum Dresden-Rossendorf. Xe ion charge states from $Q = 10$–30 are selected utilizing an analyzing magnet. To prevent charge exchange processes within the beam line or the experimental chamber the base pressure is kept below 5×10^{-9} mbar for all experiments. The kinetic ion energy is adjusted by means of an electrostatic deceleration system in the range of 40–135 keV (310–1050 eV/amu). Free-standing carbon nanomembranes with a thickness of 1 nm [28,29] from CNM TECHNOLOGIES Bielefeld, Germany, on a standard transmission electron microscopy (TEM) grid with an underlying lacey carbon support are mounted within the experimental chamber. The membranes consist of a self-assembled monolayer of 1-1'-biphenyl-4-thiol (H-$(C_6H_4)_2$-SH), which has been cross-linked (polymerized) and hydrogen depleted by low-energy electron irradiation [28]. Contaminations of the CNM with light elements (O, F, I) have been reported [28] and additional sulfur contaminations are observed using Auger electron spectroscopy. The obtained concentrations are well below 1 at. % and are therefore neglected in the following discussion; i.e., the CNM is considered as pure carbon material. Possible hydrogen content of the CNM is assumed to be small due to hydrogen loss upon preparation of the CNM [29]. A separate manipulation stage within the experimental chamber holds an electrostatic analyzer with a HAMAMATSU PHOTONICS channeltron for ion counting. This manipulation stage allows angle resolved transmission measurements with an acceptance angle of the analyzer of 1.6°. The energy resolution of the analyzer is measured to be $\Delta E \approx 1.5 \times 10^{-3} E$, giving reasonable accuracy for charge exchange measurements. The total uncertainty in energy loss determination ranges from 60 to 200 eV mainly due to limited measurement precision, i.e., number of counted ions. Note that the mean energy of the transmitted ions is deduced from the median of the distribution of the corresponding exit charge state. The electrostatic energy filter allows 5000 V as maximum voltage, which leads to constraints in measurements of large charge exchanges. The primary ion beam is charge state analyzed without target by the electrostatic analyzer to check for charge exchange with residual gas atoms within the beam line. For incident ion charge states above $Q = 20$ ions are detected with a charge loss of $\Delta Q = Q_{\text{in}} - Q_{\text{exit}} = 1$ to 3. However, the amount of ions with lower charge states than the primary one is 4 orders of magnitude smaller. Their contribution can therefore be neglected.

The intensity of the ion beam is kept below 5000 ions/s with a typical beam diameter of 1.5 mm, yielding an ion flux of about 10^9 $\text{cm}^{-2}\,\text{h}^{-1}$. Significant damage of the membrane might occur only for exposure times longer than 100 h assuming a critical fluence of 10^{11} cm^{-2}, where 1% of the ions hit a previously damaged area of 10 nm^2. No degradation of the CNM during transmission measurements is observed.

TEM and helium ion microscopy studies of the CNM reveal that no pores larger than 1 nm in diameter exist. However, on a larger scale the membrane shows cracks (10–50 μm) due to a non-perfect coverage over large holes in the support film. Control experiments using a TEM grid with a lacey carbon support film but without a CNM showed no charge exchange nor energy loss. Thus, we can conclude that (a) ions penetrating the lacey carbon film are either stopped within the film or transmitted as neutral atoms and are therefore not detected and (b) that the amount of ions undergoing small angle deflections on the walls of supporting structure or during passage through cracks is negligible.

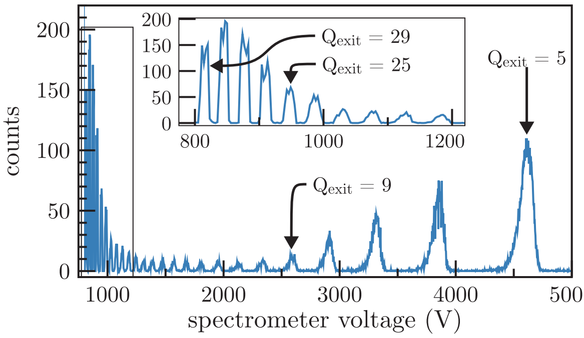

FIG. 1. (color online). Spectrum of a 1050 eV/amu Xe^{30+}beam transmitted through a 1 nm thick carbon nanomembrane. All charge states below $Q = 30$ (but larger than $Q = 4$) are visible, whereas two distinct distributions can be observed. The high exit charge state distribution is magnified in the inset.

For slow highly charged Xe ions transmitted through a CNM, two distinct exit charge state distributions are observed. Figure 1 shows a typical transmission spectrum obtained with the electrostatic analyzer. The positions of the exit charge states are marked by arrows. The first distribution, ranging from $Q_{\text{exit}} = 29$ to 12, shows an intensity maximum at $Q_{\text{exit}} = 28$. Within the uncertainty of the measurement the peaks show no energy loss and no energy straggling. Note that the peak width originates from the channeltron entrance slit (detector resolution), whereas the uncertainty is determined by the steepness of the peak edges. The second distribution, ranging from $Q_{\text{exit}} = 12$ to 5, is instead combined with an energy loss and an energy straggling visible as a larger peak width in Fig. 1. Due to the voltage limitation of our spectrometer the maximum of the second distribution can not be determined.

In order to distinguish between possible processes leading to the two exit charge state distributions angle resolved transmission measurements are performed. Figure 2 depicts three different transmission spectra for a 46.8 keV Xe^{25+} ion beam analyzed under 0°, 2°, and 4° projectile exit angle, respectively. Clearly the distribution of high charge states vanishes with tilting angle (see double logarithmic representation in the inset), while low charge states are transmitted up to 4°, even though the intensity decreases more than one order of magnitude. The energy losses $\Delta E(\alpha_{\text{exit}})$ for ions with $Q_{\text{exit}} = 2$ $(\Delta Q = 23)$ are marked as well. From the increase in energy loss with deflection angle and the fact that the high charge state distribution is only observed in (exact) forward direction we conclude that the low charge state distribution results

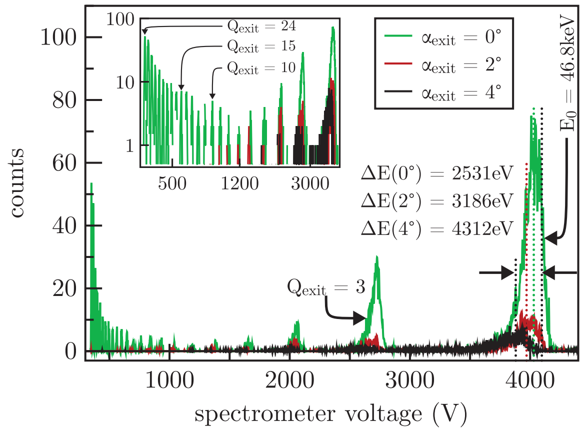

FIG. 2. (color online). Transmission spectra of a 46.8 keV (363 eV/amu) Xe^{25+} beam for different transmission angles of 0° (green), 2° (red), and 4° (black). High exit charge states are only observable under 0° (see double logarithmic inset). Due to the lower beam energy, the lowest observable exit charge state is $Q_{\mathrm{exit}} = 2$.

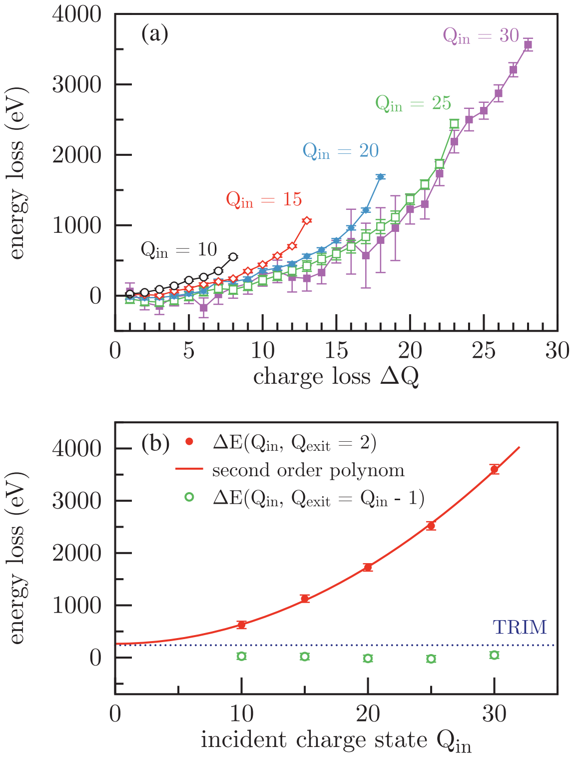

FIG. 3. (color online). Energy loss of 40 keV ions as a function of the charge loss ΔQ (a) and of the incident charge state Q_{in} (b), respectively. In (b) the energy loss is shown only for ions with exit charge state $Q_{\mathrm{exit}} = 2$ (red) and for ions with a charge loss of $\Delta Q = 1$ (green) (maximum and minimum ΔQ). The red curve is a polynomial fit of second order to the obtained data ($\Delta E(Q_{\mathrm{in}}) = 3.7\ \mathrm{eV} \cdot Q_{\mathrm{in}}^2 + 264\ \mathrm{eV}$). The dotted line shows the result from a TRIM simulation (see text).

from close collisions of the ions with target atoms. Since the mass of Xe is approximately 10 times higher than the mass of C energy and momentum conservation yield a maximum deflection angle of 5.2° for one elastic scattering event. Due to the small thickness of 1 nm of the membrane we expect that the ions undergo at most one scattering event [35]. In contrast, the high exit charge state distribution is only observed under straight forward direction and the energy loss is negligible. This is attributed to the fact that for large impact parameters the deflection angle as a result of an elastic collision as well as the transferred energy (energy loss) become very small. In this case a contribution to the energy loss could only result from ion interaction with the electrons of the membrane. However, the observed energy loss for the high exit charge states is in any case smaller than the measurement uncertainty.

The measured energy loss at 0° for highly charged ions with a constant kinetic energy of 40 keV (310 eV/amu) but varying incident charge states is shown in Fig. 3. Figure 3(a) shows the mean energy loss as a function of the charge loss ΔQ. The energy loss is strongly dependent on the charge loss, whereas the same charge loss leads to different energy losses depending on the residual charge (e.g., $\Delta Q = 18$ for $Q_{\mathrm{in}} = 20$, 25, and 30, respectively [see Fig. 3(a)]). The green dots in Fig 3(b) represent the energy loss deduced from the peaks with $\Delta Q = 1$, i.e., from ions which exhibit the smallest charge loss as a function of the incident charge state Q_{in}. The energy loss for these ions lies within the measurement uncertainty and can only be estimated to be smaller than 60 eV. The red dots in Fig. 3(b) show the energy loss obtained from the analysis of the $Q_{\mathrm{exit}} = 2$ peaks, i.e., for ions with the highest charge loss observable with our setup. These ions show a quadratic increase of the mean energy loss with incident charge state [see fit in Fig 3(b)] and consequently a much higher value than predicted by TRIM [12]. In fact, the TRIM result of 237 eV reproduces the energy loss for a neutral atom ($Q_{\mathrm{in}} = 0$) from an extrapolation of our measured data (264 eV) if one considers a CNM carbon density of $5.54 \times 10^{22}\ \mathrm{at/cm^3}$ [36] and an exit angle of < 1.6° in the simulation. Since we identified low exit charge states resulting from nuclear (i.e., elastic) collisions, the charge state dependent energy loss represents experimental evidence for the predicted increase in nuclear stopping with projectile ion charge state by Biersack [10], even though the predicted values are not reproduced.

To estimate the amount of ions transmitted at charge states, which can not be observed by the analyzer or even as neutrals, the transmission spectra have been normalized. For intensity normalization we employed the fact that a membrane usually does not cover the entire TEM grid perfectly but has some micrometer sized cracks. Ions which pass through these cracks do not interact with the target and therefore remain in their incident charge state without any

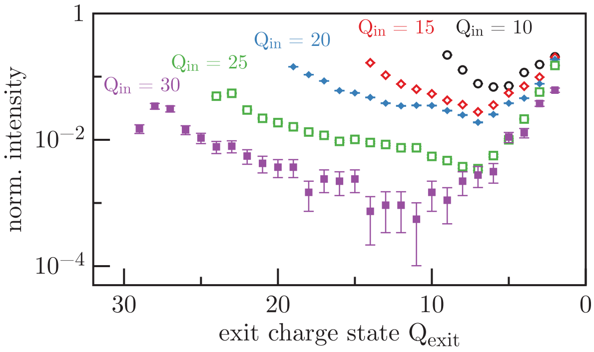

FIG. 4. (color online). Normalized intensity of exit charge states for different incident charge states from $Q_{\text{in}} = 10$ (black) to $Q_{\text{in}} = 30$ (purple) at $E_{\text{kin}} = 40$ keV (310 eV/amu).

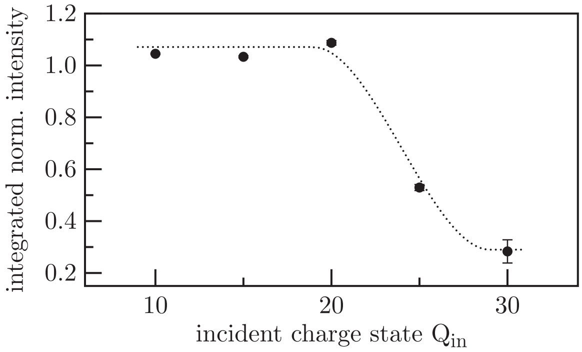

FIG. 5. Integrated normalized intensity (see text) as a function of the incident charge state for $E_{\text{kin}} = 40$ keV (310 eV/amu). The dotted line is drawn to guide the eye.

energy loss. For a constant incident kinetic ion energy of 40 keV the ratio of transmitted ions per exit charge state to the amount of transmitted ions through cracks is shown in Fig. 4. Note that all data shown in Fig. 4 are obtained from the same sample. The two distributions can clearly be distinguished by the minimum in between (e.g., $Q_{\text{exit}} = 11$ for $Q_{\text{in}} = 30$). Furthermore, the data indicate that for higher incident charge states more ions are neutralized. This can be derived from the steeper slopes towards lower exit charge states below the minimum for $Q_{\text{in}} = 30$ and 25 than for $Q_{\text{in}} = 20$, 15, and 10. This fact becomes more evident in Fig. 5 where the integral of the curves from Fig. 4 is plotted as a function of the incident charge state. An integrated normalized intensity of about 1–1.1 is obtained for incident charge states 10 to 20, whereas the value drops towards higher incident charge states to about 0.3. From the drop we conclude that for increasing incident charge states more ions are transmitted as single charged ions or as neutral atoms. Above a certain charge state the ion therefore captures electrons more effectively from the target system. The onset of the drop at about $Q_{\text{in}} = 20$ coincides very well with the observed potential energy threshold for pore production by HCI in CNM reported recently [30]. We conclude that the potential energy deposition becomes more efficient above a threshold charge state.

The fact that the two distributions are well separated may result from a strongly impact parameter dependent charge exchange. For close collisions, where also nuclear energy transfer occurs, the ion and the target atom (or target molecule) form a quasimolecule due to the strong overlap of their corresponding electronic wave functions. This overlap leads to a strong level shift [8] and therefore a direct capture of target electrons into inner shells of the ion. The consideration of the biphenyl molecule (or rather the aromatic ring after cross-linking) as the “target molecule” for the charge exchange process is physically justified by the delocalization of the carbon valence electrons over the aromatic ring and to some extend over its neighboring molecules. It also provides enough electrons to reach values of up to $\Delta Q = 28$. Contributions to the charge exchange from other species than carbon are neglected due to their small concentrations (< 1 at.%) and from hydrogen due to the fact that it provides only one electron per atom. For large impact parameters (> 2 Å) the nuclear charge of the carbon atoms is sufficiently screened and no nuclear energy transfer occurs. Electrons may only be transferred to the ion via classical over barrier transport [37,38], because no overlap of the electron densities of the molecule and the ion occurs. The critical distance $R_c \propto \sqrt{8Q+2}/W$ for classical charge transfer depends on the work function W of the material in the case of above surface neutralization [38]. The present experimental findings indicate a critical distance R_c smaller than the interatomic distances in the membrane. Therefore the work function should be identified here with the ionization energy of the cross-linked biphenyl molecule or for simplicity with the atomic ionization energies (11, 24, 46 eV, …) for successive ionization of carbon [39]. Since the second electron to be transferred has already a much higher binding energy than the first one, its exchange is only possible at much shorter distances. Niehaus showed in his extended classical over barrier model for charge exchange of highly charged ions interacting with molecules that the cross section for three-electron-capture is already about a factor of 30 smaller than the cross section for one-electron-capture [37]. Charge exchanges for impact parameter larger than those needed for a sufficient level shift are therefore limited to small ΔQ. For slow highly charged ions interacting with very thin target materials the processes can hence be described better in a picture of ion-molecule interaction rather than ion-solid interaction. The concept of stopping force as the *mean* energy loss per unit length fails in a thin membrane, because no averaging over impact parameters appears anymore.

The authors acknowledge fruitful discussions with Christoph Lemell. Thanks go to Nico Klingner for support with the channeltron. Financial support from the Deutsche Forschungsgemeinschaft (DFG) (Project No. HE 6174/1-1) and from the Austrian FWF (Project No. I 1114-N20) is acknowledged.

---

[*] r.wilhelm@hzdr.de

[1] A. K. Geim and K. S. Novoselov, Nat. Mater. **6**, 183 (2007).

[2] A. K. Geim, Science **324**, 1530 (2009).

[3] O. Ochedowski, B. Kleine Bussmann, B. Ban d'Etat, H. Lebius, and M. Schleberger, Appl. Phys. Lett. **102**, 153103 (2013).

[4] S. Bertolazzi, J. Brivio, and A. Kis, ACS Nano **5**, 9703 (2011).

[5] H.-P. Komsa, S. Kurasch, O. Lehtinen, U. Kaiser, and A. V. Krasheninnikov, Phys. Rev. B **88**, 035301 (2013).

[6] D. Kost, S. Facsko, W. Möller, R. Hellhammer, and N. Stolterfoht, Phys. Rev. Lett. **98**, 225503 (2007).

[7] U. Bangert, W. Pierce, D. M. Kepaptsoglou, Q. Ramasse, R. Zan, M. H. Gass, J. A. Van den Berg, C. B. Boothroyd, J. Amani, and H. Hofsäss, Nano Lett. **13**, 4902 (2013).

[8] A. Arnau, F. Aumayr, P. M. Echenique, M. Grether, W. Heiland, J. Limburg, R. Morgenstern, P. Roncin, S. Schippers, R. Schuch, N. Stolterfoht, P. Varga, T. J. M. Zouros, and H. P. Winter, Surf. Sci. Rep. **27**, 113 (1997).

[9] F. Aumayr, S. Facsko, A. S. El-Said, C. Trautmann, and M. Schleberger, J. Phys. Condens. Matter **23**, 393001 (2011).

[10] J. P. Biersack, Nucl. Instrum. Methods Phys. Res., Sect. B **80–81**, 12 (1993).

[11] W. Brandt and M. Kitagawa, Phys. Rev. B **25**, 5631 (1982).

[12] J. F. Ziegler, J. P. Biersack, and M. D. Ziegler, *SRIM—The Stopping and Range of Ions in Matter*, Vol. 5 (SRIM Co., Chester, MD, 2008).

[13] R. Heller, S. Facsko, R. A. Wilhelm, and W. Möller, Phys. Rev. Lett. **101**, 096102 (2008).

[14] A. S. El-Said, R. Heller, W. Meissl, R. Ritter, S. Facsko, C. Lemell, B. Solleder, I. C. Gebeshuber, G. Betz, M. Toulemonde, W. Möller, J. Burgdörfer, and F. Aumayr, Phys. Rev. Lett. **100**, 237601 (2008).

[15] A. S. El-Said, R. Heller, F. Aumayr, and S. Facsko, Phys. Rev. B **82**, 033403 (2010).

[16] A. S. El-Said, R. A. Wilhelm, R. Heller, S. Facsko, C. Lemell, G. Wachter, J. Burgdörfer, R. Ritter, and F. Aumayr, Phys. Rev. Lett. **109**, 117602 (2012).

[17] R. Ritter, R. A. Wilhelm, R. Ginzel, G. Kowarik, R. Heller, A. S. El-Said, R. M. Papaléo, W. Rupp, J. R. C. López-Urrutia, J. Ullrich, S. Facsko, and F. Aumayr, Europhys. Lett. **97**, 13001 (2012).

[18] L. P. Ratliff, R. Minniti, A. Bard, E. W. Bell, J. D. Gillaspy, D. Parks, A. J. Black, and G. M. Whitesides, Appl. Phys. Lett. **75**, 590 (1999).

[19] A. Persaud, S. J. Park, J. A. Liddle, T. Schenkel, J. Bokor, and I. W. Rangelow, Nano Lett. **5**, 1087 (2005).

[20] M. Ilg, C. D. Weis, J. Schwartz, A. Persaud, Q. Ji, C. Chi Lo, J. Bokor, A. Hegyi, E. Guliyev, I. W. Rangelow, and T. Schenkel, J. Vac. Sci. Technol. B **30**, 06FD04 (2012).

[21] M. Tona, H. Watanabe, S. Takahashi, N. Nakamura, N. Yoshiyasu, M. Sakurai, T. Terui, S. Mashiko, C. Yamada, and S. Ohtani, Surf. Sci. **601**, 723 (2007).

[22] Y. Baba, K. Nagata, S. Takahashi, N. Nakamura, N. Yoshiyasu, M. Sakurai, C. Yamada, S. Ohtani, and M. Tona, Surf. Sci. **599**, 248 (2005).

[23] S. Takahashi, M. Tona, K. Nagata, N. Nakamura, N. Yoshiyasu, C. Yamada, S. Ohtani, and M. Sakurai, Appl. Phys. Lett. **87**, 063111 (2005).

[24] N. Nakamura, M. Terada, Y. Nakai, Y. Kanai, S. Ohtani, K. Komaki, and Y. Yamazaki, Nucl. Instrum. Methods Phys. Res., Sect. B **232**, 261 (2005).

[25] J. M. Pomeroy, H. Grube, A. C. Perrella, and J. D. Gillaspy, Appl. Phys. Lett. **91**, 073506 (2007).

[26] R. E. Lake, J. M. Pomeroy, H. Grube, and C. E. Sosolik, Phys. Rev. Lett. **107**, 063202 (2011).

[27] J. M. Pomeroy, R. E. Lake, and C. E. Sosolik, Nucl. Instrum. Methods Phys. Res., Sect. B **269**, 1238 (2011).

[28] A. Turchanin, A. Beyer, C. T. Nottbohm, X. H. Zhang, R. Stosch, A. Sologubenko, J. Mayer, P. Hinze, T. Weimann, and A. Gölzhäuser, Adv. Mater. **21**, 1233 (2009).

[29] A. Turchanin and A. Gölzhäuser, Prog. Surf. Sci. **87**, 108 (2012).

[30] R. Ritter, R. A. Wilhelm, M. Stöger-Pollach, R. Heller, A. Mücklich, U. Werner, H. Vieker, A. Beyer, S. Facsko, A. Gölzhäuser, and F. Aumayr, Appl. Phys. Lett. **102**, 063112 (2013).

[31] M. A. Briere, T. Schenkel, D. H. Schneider, P. Bauer, and A. Arnau, Phys. Scr. **T73**, 324 (1997).

[32] T. Schenkel, M. A. Briere, A. V. Barnes, A. V. Hamza, K. Bethge, H. Schmidt-Böcking, and D. H. Schneider, Phys. Rev. Lett. **79**, 2030 (1997).

[33] T. Schenkel, A. V. Hamza, A. V. Barnes, and D. H. Schneider, Prog. Surf. Sci. **61**, 23 (1999).

[34] G. Zschornack, M. Kreller, V. P. Ovsyannikov, F. Grossman, U. Kentsch, M. Schmidt, F. Ullmann, and R. Heller, Rev. Sci. Instrum. **79**, 02A703 (2008).

[35] We estimate that the elastic mean free path is in the range of the membrane's thickness or even larger by considering a model of hard spheres and an energy transfer cutoff of 10 eV.

[36] D. G. Matei, N. E. Weber, S. Kurasch, S. Wundrack, M. Woszczyna, M. Grothe, T. Weimann, F. Ahlers, R. Stosch, U. Kaiser, and A. Turchanin, Adv. Mater. **25**, 4146 (2013).

[37] A. Niehaus, J. Phys. B **19**, 2925 (1986).

[38] J. Burgdörfer, P. Lerner, and F. W. Meyer, Phys. Rev. A **44**, 5674 (1991).

[39] U. Thumm, J. Phys. B **27**, 3515 (1994).

RAPID COMMUNICATIONS

PHYSICAL REVIEW B **89**, 121301(R) (2014)

Ferromagnetism and impurity band in a magnetic semiconductor: InMnP

M. Khalid,[1,*] Eugen Weschke,[2] W. Skorupa,[1] M. Helm,[1,3] and Shengqiang Zhou[1,†]
[1]*Helmholtz-Zentrum Dresden Rossendorf, Institute of Ion Beam Physics and Materials Research, Bautzner Landstrasse 400, D-01328 Dresden, Germany*
[2]*Helmholtz-Zentrum Berlin für Materialien und Energie, Wilhelm-Conrad-Röntgen-Campus BESSY II, D-12489 Berlin, Germany*
[3]*Technische Universität Dresden, D-01062 Dresden, Germany*

(Received 5 November 2013; revised manuscript received 21 February 2014; published 6 March 2014)

We have synthesized ferromagnetic InMnP, a member of the III-Mn-V ferromagnetic semiconductor family, by Mn ion implantation and pulsed laser annealing. Clear ferromagnetic hysteresis loops and a perpendicular magnetic anisotropy are observed up to a Curie temperature of 42 K. Large values of negative magnetoresistance and magnetic circular dichroism as well as an anomalous Hall effect are further evidence of a ferromagnetic order in InMnP. An effort is made to understand the transport mechanism in InMnP using the theoretical models. We find that the valence band of InP does not merge with the impurity band of the heavily doped ferromagnetic InMnP. Our results suggest that impurity band conduction is a characteristic of Mn-doped III-V semiconductors which have deep Mn-acceptor levels.

DOI: 10.1103/PhysRevB.89.121301 PACS number(s): 75.50.Pp, 75.70.−i

Diluted magnetic semiconductors (DMSs) containing a few atomic percent of a magnetic element exhibit simultaneous magnetic and semiconducting properties below the Curie temperature. The III-V based prototype ferromagnetic semiconductor GaMnAs has revealed a variety of unique features induced by the combination of its magnetic and semiconducting properties. Among these are the electric-field control of the Curie temperature [1] and the magnetization direction [2] and the low-current-density-induced magnetization reversal [3], which are expected to be useful for upcoming ultralow-power spintronic devices.

Yet controversy still surrounds the GaMnAs band structure and the mechanism behind the ferromagnetism. Generally two models are being used to explain the ferromagnetism in III-V semiconductors: the mean-field Zener model, where the ferromagnetism in III-V:Mn arises due to the *p-d* exchange interaction between the valence band (VB) holes and the localized Mn-3*d* electrons, and the Zener double-exchange model, where the hopping of the spin-polarized holes in the impurity band (IB) stabilizes the ferromagnetism. The former model seems to explain several features of GaMnAs, such as the carrier dependent metal-insulator transition [4], hole concentration dependent Curie temperature [5], etc. On the other hand, optical [6–8] and transport [9] studies of GaMnAs have revealed that the Fermi energy level (E_f) lies in the IB within the band gap of GaMnAs. Despite massive investigations on the origin and control of ferromagnetism in DMSs, the origin of ferromagnetism and the location of the impurity band in III-V-Mn semiconductors is still controversial [7,10–13]. Note that the Mn energy level ranges from 10 to 440 meV in different III-V hosts. It is unlikely that all different III-V-Mn combinations can be treated within a single model.

Scarpulla *et al.* prepared ferromagnetic GaMnP, which has the deepest Mn acceptor level (440 meV) among III-V semiconductors. They found that the ferromagnetic exchange coupling was mediated by holes localized in a Mn-derived band that is detached from the valence band [14]. Due to the deep Mn-acceptor level, strongly localized hole states are expected, leading to a detached impurity band in GaMnP. Moreover, GaMnP has an indirect band gap which also restricts its applications in optoelectronic devices. Therefore, it is worth choosing a system that has a band gap and Mn-acceptor energy level in between those of GaMnP (440 meV) and GaMnAs (110 meV) for a further understanding of the valence-impurity band dilemma in III-V semiconductors.

InP is a suitable candidate for investigating the existence and merging of the IB in InMnP, because it has a band gap (1.34 eV) closer to that of GaAs (1.42 eV) and a Mn-acceptor level at an energy 220 meV above the valence band which is almost half of the GaMnP [15]. Moreover, Dietl *et al.* have demonstrated theoretically that Mn-doped InP could be a promising diluted magnetic semiconductor (DMS) with a Curie temperature of ~50 K [16] where 5% Mn is substituted for the indium in the crystal grate nodes and is of $10^{20}/\mathrm{cm}^3$ hole concentration. To the best of our knowledge, a comprehensive report on the magnetic properties of InMnP is lacking in the literature, except for some reports which, in our opinion, do not show clear evidence of carrier-mediated ferromagnetism in InMnP. First, undesirable secondary phases appear in samples annealed by conventional methods (e.g., thermal annealing) [17–19]. Second, ferromagnetism is reported in Zn-doped *p*-type InMnP for a Mn concentration of only 1 at. % [20]. This would be incompatible with the well-established theory of ferromagnetism in semiconductors [16,21]. There must be a sufficient amount of Mn ions (~5 at. %) in the sample so that a net ferromagnetic order can be achieved at a reasonable high temperature (~50 K). Hence, those previous reports neither prove the intrinsic mechanism of ferromagnetism nor do they give any insight into the nature of the impurity band in InMnP. Therefore, it is highly desirable to synthesize a diluted magnetic semiconductor, InMnP, with reliable magnetic and transport properties. It can also contribute to the understanding of the valence-impurity band picture in III-V semiconductors.

In this Rapid Communication we focus on the Mn-induced ferromagnetism and the location of the Mn-induced impurity band in InMnP prepared by Mn ion implantation and pulsed

---

[*] m.khalid@hzdr.de
[†] s.zhou@hzdr.de

laser melting. We mainly discuss the results of a heavily doped (Mn 5 at. %) InMnP sample, however, some results of a low Mn-doped (Mn ∼ 2.5 at. %) InMnP sample are also included. The magnetization, magnetotransport, and x-ray magnetic circular dichroism (XMCD) measurements were carried out to support an intrinsic origin of ferromagnetism and the existence of a separate impurity band in InMnP.

Semi-insulating InP(100) wafers were implanted with 50 keV Mn^+ to fluences of $2 \times 10^{16}/\mathrm{cm}^2$ and $1 \times 10^{16}/\mathrm{cm}^2$, hereafter referred to as sample A and sample B, respectively. After that the samples were annealed by a XeCl excimer laser using an energy density of 0.4 $\mathrm{J/cm}^2$ for a single pulse duration (30 ns). The Mn concentration over a depth of around 90 nm (measured by transmission electron microscopy and Auger electron spectroscopy, not shown) for sample A was ∼5 at. %. Magnetization of the samples was measured by a superconducting quantum interference device (SQUID). Magnetotransport and XMCD measurements were performed using a Lakeshore system and at the beamline UE46/PGM-1 at BESSY II (Helmholtz-Zentrum Berlin), respectively.

Figure 1(a) shows the remanent magnetization versus temperature for three different InMnP samples. The Curie temperature (T_c) of the laser annealed samples A and B are found to be ∼42 and ∼20 K, respectively, while the as-implanted sample did not exhibit a ferromagnetically ordered state down to the lowest measured temperature. The inset of Fig. 1(a) represents the magnetic response of sample A as a function of a magnetic field at 5 K. There are two main contributions in the magnetic signals, a diamagnetic response which is due the InP substrate and a ferromagnetic one which originates from the Mn-implanted layer. It also shows a magnetic anisotropy (easy axis perpendicular to the sample plane) which often originates due to tensile strain, not only in Mn-implanted samples, but also in III-V semiconductors grown by molecular beam epitaxy (MBE) [22,23]. The dependence of Curie temperature on the Mn concentration supports the carrier-mediated ferromagnetism in InMnP.

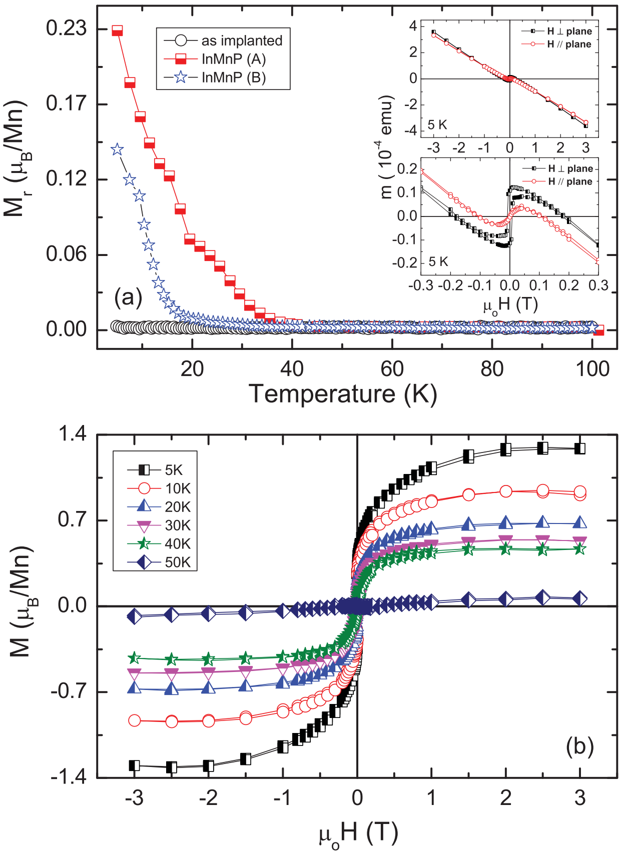

FIG. 1. (Color online) (a) Remanent magnetization vs temperature for an as-implanted sample and two laser annealed InMnP samples A and B. The inset shows the magnetization of laser annealed sample A in magnetic field ranges ±3 and ±0.3 T applied parallel and perpendicular to the sample plane. (b) Magnetization loops of laser annealed sample A measured at several temperatures. The magnetic field is applied perpendicular to the sample plane.

Ferromagnetic loops are observed up to the Curie temperature for sample A, as shown in Fig. 1(b). The saturation magnetization at 5 K is $\sim 1.2\mu_B$/Mn by considering that all implanted Mn ions contribute to the magnetization of the sample. Practically, this value is largely underestimated due to the following reasons: First, the sputtering effect in III-V semiconductors during ion implantation reduces the effective implantation fluence [24]. Second, it is known that the pulsed laser annealing results in a magnetically inert layer with a large Mn concentration due to surface segregation [25]. Moreover, self-compensation as in GaMnAs [26] can further depress the ferromagnetism in InMnP. If half of the implanted Mn concentration contributes to the total magnetization of InMnP, then the estimated magnetization will be $\sim 2.4\mu_B$/Mn, which is comparable to the magnetization of InMnAs [22,27].

X-ray absorption spectroscopy (XAS) is widely used to probe the electronic structure of matter while x-ray magnetic circular dichroism (XMCD) by utilizing circularly polarized light gives selective elemental magnetic information about a specimen. We have performed XMCD measurements on sample A at the Mn $L_{2,3}$ edges in which the $2p$ core electrons are excited to the unoccupied $3d$ states and consequently information about the electronic structure of the polarized Mn band is obtained (for more details, see Ref. [28] and references therein). The sample was etched in a diluted HCl solution (5%) prior to XMCD measurements to remove the surface oxide layer. This method has also been used previously for GaMnAs and GaMnP [29,30].

Figure 2(a) shows XAS spectra at the Mn $L_{2,3}$ edges along with a XMCD spectrum in total electron yield (TEY) mode at 4.2 K under a magnetic field of 4 T for sample A. The main intense features in the XAS spectra at the $L_{2,3}$ edges (at energies around 640 and 652 eV) are due to electric-dipole allowed transitions (i.e., $\Delta\ell = \pm 1$) from $2p$ to unfilled $3d$ states. A careful inspection of the XAS spectra of InMnP indicates that the spectral features are very similar to those of ferromagnetic GaMnP, GaMnAs, and InMnAs [25,29,30] regardless of whether they have different energy gaps and Mn-acceptor levels. It also hints to a similar bonding and p-d exchange interaction in most of the Mn-doped III-V semiconductors. The XMCD signal at the L_3 edge of InMnP defined as $(\mu^+ - \mu^-)/(\mu^+ + \mu^-)$ is ∼40% at 4.2 K under a magnetic field of 4 T, which is comparable to that of ferromagnetic GaMnP [25]. The large XMCD signal of InMnP also indicates that it has a high spin polarization at the

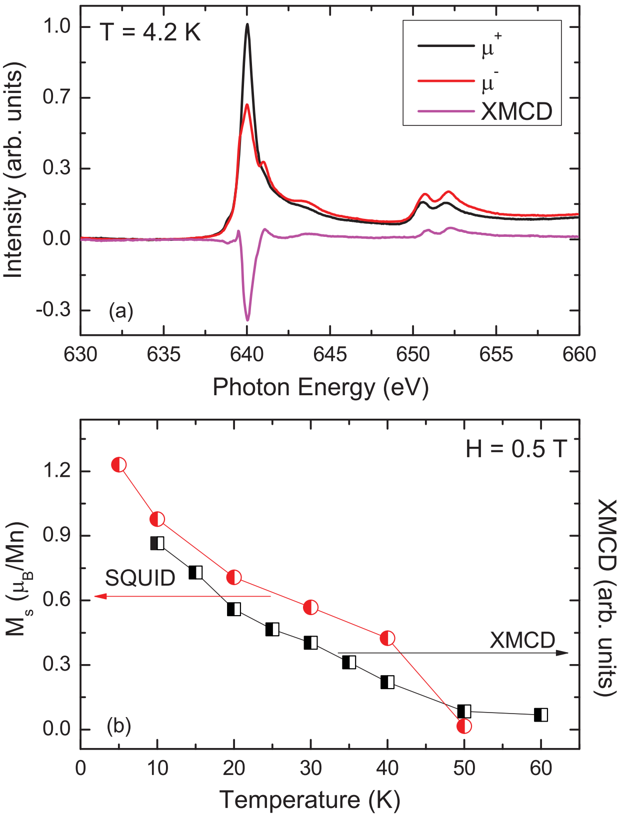

FIG. 2. (Color online) (a) XAS and XMCD spectra of an InMnP sample A measured at 4.2 K under a magnetic field of 4 T applied normal to the sample surface. (b) Saturation magnetization and normalized XMCD signals of the same sample at different temperatures under a magnetic field of 0.5 T.

Fermi energy (E_f). The XMCD sum rules also provide information on the degree of the spin and orbital moments in the system [31,32]. The spin moment calculated using XMCD data and the sum rules in InMnP sample A is $\sim 1\mu_B$/Mn while the orbital moment is negligibly small. This value of spin moment is slightly smaller than that obtained from SQUID measurements. The discrepancy in the magnetic moment could be due to the depth profile of the Mn concentration and the depth sensitivity of the two techniques (SQUID is volume sensitive while XMCD in the total electron yield mode is surface sensitive).

We have compared the magnetization measured by SQUID magnetometry and temperature dependent normalized XMCD signals in order to exclude any contribution from external impurities to the magnetization of the InMnP sample. Figure 2(b) shows the saturation magnetization and normalized XMCD signals at different temperatures. Both the magnetization and normalized XMCD signals decrease with temperature and vanish at ~50 K just above the Curie temperature (42 K). The very analogous temperature dependence of both quantities indicates an intrinsic origin of ferromagnetism in InMnP.

Another method for studying the carrier-mediated nature of ferromagnetism is the magnetotransport. We have carried out temperature dependent resistivity and magnetotransport

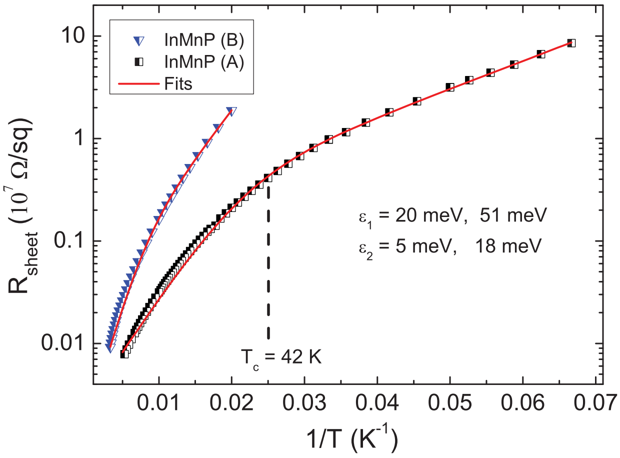

FIG. 3. (Color online) Sheet resistance of InMnP samples A and B as a function of inverse temperature. The red solid lines show the fits of data to Eq. (1).

(magnetoresistance, Hall effect) measurements on InMnP samples using van der Pauw geometry under a magnetic field perpendicular to the sample plane using a Lakeshore system. The temperature and magnetic field were varied up to 150 K and 6 T, respectively. Figure 3 shows the sheet resistance of InMnP samples A and B as a function of inverse temperature at zero field. We did not observed any metal-insulator transition, as has been observed in heavily doped GaMnAs [33], rather, the InMnP samples show an insulating character similar to that of GaMnP [14]. Therefore, to describe a thermally activated conduction process at high and low temperatures, we used a model given in Eq. (1),

$$\rho(T)^{-1} = [\rho_1 \exp(E_1/\kappa_B T)]^{-1} + [\rho_2 \exp(E_2/\kappa_B T)]^{-1}, \tag{1}$$

where preexponential constants ρ_1, ρ_2 and activation energies E_1, E_2 are the free parameters. The measured temperature dependent resistivity data fit to this model quite nicely. The fitting results indicate two thermally activated contributions to the resistivity of InMnP. For sample A a high temperature activation region with an activation energy ~20 meV (E_1) and a low temperature activation region with an energy ~5.1 meV (E_2) are observed. The activation energies in InMnP sample A for two activated regions are smaller than those of GaMnP [14], which are expected because of the following reason. The transition between the valence band and the acceptor states are responsible for the low resistivity at high temperatures. As the Mn-acceptor level in InMnP lies at a lower energy (220 meV) compared to GaMnP (400 meV), therefore, to excite an electron from the valence band to acceptor states needs less energy in InMnP. A close examination of the resistivity data of sample A in Fig. 3 also indicates a continuous change in the slope near T_c (42 K), which can be due to the nearest-neighbor hopping transport [34] at low temperatures with an activation energy 5.1 meV in sample A. On the other hand, for the low Mn-doped InMnP sample B, E_1 and E_2 increase to ~50 and ~18 meV, respectively. This is expected due to the narrowing of the impurity band and the shift of

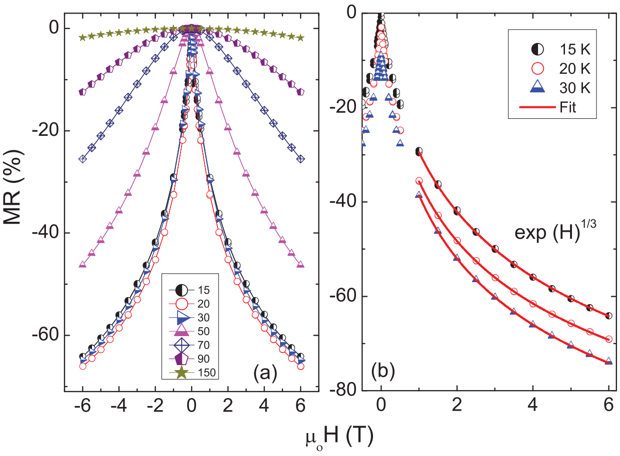

FIG. 4. (Color online) (a) Magnetoresistance of an InMnP sample A measured at several temperatures. (b) The red solid lines show the fits of the data to a model given in Eq. (2). Note that for clarity, the MR curves measured at 20 and 30 K are shifted vertically by constants 3 and 9, respectively.

the Fermi energy in the Mn-induced band accompanied by a reduction in hole concentration at a lower Mn concentration. It seems that, as least for semiconductors with deep Mn-acceptor levels, an impurity band is formed in heavily Mn-doped III-V semiconductors which is detached from the valence band. The high insulating character and the hopping transport in InMnP support a detached impurity band in InMnP.

To shed more light on the hopping transport mechanism in InMnP at low temperatures, we have performed magnetotransport experiments over a wider temperature range. Figure 4(a) shows the magnetoresistance of sample A measured at different temperatures above and below the Curie temperature. It exhibits negative magnetoresistance, as is typical for III-V diluted magnetic semiconductors. At the lowest measured temperature (15 K) the relative magnetoresistance, defined as $\mathrm{MR}(\%) = \{[\rho(H) - \rho(0)]/\rho(0)\} \times 100$, is about 64% at 6 T, which increases with the temperature and reaches a maximum value of 66% at 20 K, and then decreases with the temperature. The negative magnetoresistance in InMnP can be explained as follows: When a magnetic field is applied, it results in an antiferromagnetic coupling between the Mn ion and the hole. Consequently, the wave functions of Mn-hole complexes expand and the increased overlapping of these wave functions results in a negative magnetoresistance of InMnP. We have used a model in high-field limits, i.e., $\lambda \ll a$, where λ and a are the magnetic length and localization radius, respectively, which has been previously used for insulating GaMnAs [35]. The model is given in Eq. (2),

$$\rho(H) = \rho_o \exp\left[\frac{C}{(\lambda^2 T)^{1/3}}\right], \tag{2}$$

where $\lambda = (\frac{\hbar}{e\mu_0 H})^{1/2}$ is the magnetic length. This model is used to fit the magnetoresistance data below T_c and the results are shown in Fig. 4(b). The fit results show that the model is applicable to explain the magnetoresistance of InMnP in the high-field range of 1–6 T. The fitting parameter C has a negative sign due to the expansion of the wave functions in a magnetic field. The magnetotransport results suggest that hopping is the main conduction mechanism in InMnP at low temperatures, which is also an indication of a separated Mn-impurity-induced band within the band gap of InP.

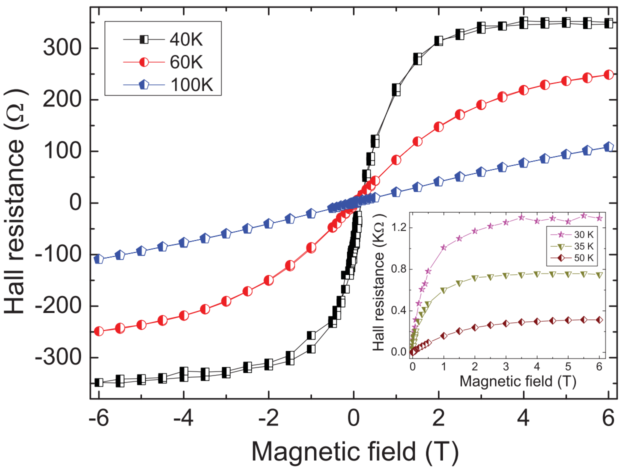

FIG. 5. (Color online) Anomalous Hall effect in InMnP at different temperatures. The inset shows the anomalous Hall effect below T_c.

Finally, the anomalous Hall effect was measured in the InMnP sample. It reflects the presence of spin-polarized carriers along with their type and concentration in the sample. The Hall resistance R_{Hall} of a magnetic semiconductor can be expressed phenomenologically as in Eq. (3),

$$R_{\mathrm{Hall}} = R_o B + R_s M. \tag{3}$$

The first term on the right-hand side of Eq. (3) is the ordinary Hall resistance while the second term stands for the anomalous Hall resistance. In general, the anomalous Hall contribution is proportional to the macroscopic magnetization of the sample [36]. Figure 5 shows the Hall resistance of InMnP sample A as a function of applied field measured at different temperatures. The Hall resistance of InMnP is dominated by the anomalous Hall component at low temperatures (see Fig. 5 and its inset). The temperature dependence and the shape of the Hall resistance is quite similar to that of magnetization of InMnP sample A. Therefore, we can conclude that both types of measurements reflect the intrinsic ferromagnetism of InMnP. The slope of the Hall resistance remains positive up to the measured temperatures and fields. This confirms that holes are the majority carriers in InMnP.

In conclusion, we have prepared the diluted magnetic semiconductor InMnP by Mn implantation and pulsed laser annealing. The transport results suggest that a separate impurity band formation is preferable even in heavily doped InMnP. The magnetization, x-ray circular dichroism, magnetoresistance, and anomalous Hall effect reflect an intrinsic ferromagnetic order in Mn-implanted InP. A large XMCD signal and negative magnetoresistance indicate that InMnP has a high spin polarization at the Fermi energy (E_F) and the ferromagnetism is carrier mediated. Last but not least, a careful inspection of XAS spectra of InMnP points out that the spectral features are very similar to those of ferromagnetic GaMnP and GaMnAs [14] regardless of whether they have different energy gaps and Mn-acceptor levels. The high insulating character of InMnP is very similar to that of GaMnP, which could be due to strong localization of carriers in an impurity band (low mobility) and the hopping transport mechanism supports a separate impurity band formation in InMnP and similar III-V semiconductors which have deep Mn-acceptor levels.

The authors thank René Hübner for transmission electron microscopy measurements. The work is financially supported by the Helmholtz-Gemeinschaft Deutscher Forschungszentren (VH-NG-713).

---

[1] H. Ohno, D. Chiba, F. Matsukura, T. Omiya, E. Abe, T. Dietl, Y. Ohno, and K. Ohtani, Nature (London) **408**, 944 (2000).

[2] D. Chiba, M. Sawicki, Y. Nishitani, Y. Nakatani, F. Matsukura, and H. Ohno, Nature (London) **455**, 515 (2008).

[3] M. Watanabe, J. Okabayashi, H. Toyao, T. Yamaguchi, and J. Yoshino, Appl. Phys. Lett. **92**, 082506 (2008).

[4] A. MacDonald, P. Schiffer, and N. Samarth, Nat. Mater. **4**, 195 (2005).

[5] Y. Nishitani, D. Chiba, M. Endo, M. Sawicki, F. Matsukura, T. Dietl, and H. Ohno, Phys. Rev. B **81**, 045208 (2010).

[6] K. Hirakawa, S. Katsumoto, T. Hayashi, Y. Hashimoto, and Y. Iye, Phys. Rev. B **65**, 193312 (2002).

[7] K. S. Burch, D. B. Shrekenhamer, E. J. Singley, J. Stephens, B. L. Sheu, R. K. Kawakami, P. Schiffer, N. Samarth, D. D. Awschalom, and D. N. Basov, Phys. Rev. Lett. **97**, 087208 (2006).

[8] K. Ando, H. Saito, K. C. Agarwal, M. C. Debnath, and V. Zayets, Phys. Rev. Lett. **100**, 067204 (2008).

[9] L. P. Rokhinson, Y. Lyanda-Geller, Z. Ge, S. Shen, X. Liu, M. Dobrowolska, and J. K. Furdyna, Phys. Rev. B **76**, 161201 (2007).

[10] S. Ohya, K. Takata, and M. Tanaka, Nat. Phys. **7**, 342 (2011).

[11] J. Mašek, F. Máca, J. Kudrnovský, O. Makarovsky, L. Eaves, R. Campion, K. Edmonds, A. Rushforth, C. Foxon, B. Gallagher *et al.*, Phys. Rev. Lett. **105**, 227202 (2010).

[12] N. Smarth, Nat. Mater. **11**, 360 (2012).

[13] M. Dobrowolska, K. Tivakornsasithorn, X. Liu, J. Furdyna, M. Berciu, K. Yu, and W. Walukiewicz, Nat. Mater. **11**, 444 (2012).

[14] M. A. Scarpulla, B. L. Cardozo, R. Farshchi, W. M. H. Oo, M. D. McCluskey, K. M. Yu, and O. D. Dubon, Phys. Rev. Lett. **95**, 207204 (2005).

[15] B. Clerjaud, J. Phys. C: Solid State Phys. **18**, 3615 (1985).

[16] T. Dietl, H. Ohno, F. Matsukura, J. Cibert, and D. Ferrand, Science **287**, 1019 (2000).

[17] Y. Shon, I. Yoon, S. Lee, H. Jeon, Y. Kwon, T. Kang, C. Park, and H. Kim, J. Korean Phys. Soc. **61**, 1292 (2012).

[18] Y. Shon, S. Lee, I. Yoon, T. Kang, Y. Lee, D. Kim, C. Yoon, and C. Park, J. Korean Phys. Soc. **61**, 1065 (2012).

[19] I. Bucsa, R. Cochrane, and S. Roorda, J. Appl. Phys. **107**, 073912 (2010).

[20] Y. Shon, H. Jeon, S. Lee, C. Park, E. Kim, D. Fu, X. Fan, C. Yoon, and J. Lee, Mater. Sci. Eng. B **146**, 220 (2008).

[21] T. Dietl, Semicond. Sci. Technol **17**, 377 (2002).

[22] S. Zhou, Y. Wang, Z. Jiang, E. Weschke, and M. Helm, Appl. Phys. Express **5**, 093007 (2012).

[23] A. Rushforth, M. Wang, N. Farley, R. Campion, K. Edmonds, C. Staddon, C. Foxon, and B. Gallagher, J. Appl. Phys. **104**, 073908 (2008).

[24] C. Fritzsche and W. Rothemund, Appl. Phys. **7**, 39 (1975).

[25] M. Scarpulla, R. Farshchi, P. Stone, R. Chopdekar, K. Yu, Y. Suzuki, and O. Dubon, J. Appl. Phys. **103**, 073913 (2008).

[26] G. Bouzerar, T. Ziman, and J. Kudrnovský, Phys. Rev. B **72**, 125207 (2005).

[27] T. Schallenberg and H. Munekata, Appl. Phys. Lett. **89**, 042507 (2006).

[28] G. Schütz, W. Wagner, W. Wilhelm, P. Kienle, R. Zeller, R. Frahm, and G. Materlik, Phys. Rev. Lett. **58**, 737 (1987).

[29] K. W. Edmonds, N. R. S. Farley, R. P. Campion, C. T. Foxon, B. L. Gallagher, T. K. Johal, G. van der Laan, M. MacKenzie, J. N. Chapman, and E. Arenholz, Appl. Phys. Lett. **84**, 4065 (2004).

[30] P. R. Stone, M. A. Scarpulla, R. Farshchi, I. D. Sharp, E. E. Haller, O. D. Dubon, K. M. Yu, J. W. Beeman, E. Arenholz, J. D. Denlinger *et al.*, Appl. Phys. Lett. **89**, 012504 (2006).

[31] B. T. Thole, P. Carra, F. Sette, and G. van der Laan, Phys. Rev. Lett. **68**, 1943 (1992).

[32] W. L. O'Brien and B. P. Tonner, Phys. Rev. B **50**, 12672 (1994).

[33] F. Matsukura, H. Ohno, A. Shen, and Y. Sugawara, Phys. Rev. B **57**, R2037 (1998).

[34] A. Kaminski and S. Das Sarma, Phys. Rev. B **68**, 235210 (2003).

[35] A. Van Esch, L. Van Bockstal, J. De Boeck, G. Verbanck, A. S. van Steenbergen, P. J. Wellmann, B. Grietens, R. Bogaerts, F. Herlach, and G. Borghs, Phys. Rev. B **56**, 13103 (1997).

[36] C. M. Hurd, *The Hall Effect and its Application* (Plenum, New York, 1980), pp. 1–54.

Statistics

Image: HZDR

Publications and patents

Books and chapters

1. Skorupa, W.; Schmidt, H. (Editors)
Subsecond Annealing of Advanced Materials: Annealing by Lasers, Flash Lamps and Swift Heavy Ions
Springer Series in Materials Science **192**, Springer Heidelberg (2014), ISBN 978-3-319-03130-9

Publications in journals

Magnetism

1. Bali, R.; Wintz, S.; Meutzner, F.; Hübner, R.; Boucher, R.; Ünal, A. A.; Valencia, S.; Neudert, A.; Potzger, K.; Bauch, J.; Kronast, F.; Facsko, S.; Lindner, J.; Fassbender, J.
Printing Nearly-Discrete Magnetic Patterns Using Chemical Disorder Induced Ferromagnetism
*Nano Letters **14**, 435 (2014)*
2. Ball, D. K.; Lenz, K.; Fritzsche, M.; Varvaro, G.; Günther, S.; Krone, P.; Makarov, D.; Mücklich, A.; Facsko, S.; Fassbender, J.; Albrecht, M.
Magnetic properties of granular CoCrPt:SiO_2 thin films deposited on GaSb nanocones
*Nanotechnology **25**, 085703 (2014)*
3. Bernert, K.; Sluka, V.; Fowley, C.; Lindner, J.; Fassbender, J.; Deac, A. M.
Phase diagrams of MgO magnetic tunnel junctions including the perpendicular spin-transfer torque in different geometries
*Physical Review B **89**, 134415 (2014)*
4. Duan, Z.; Smith, A.; Yang, L.; Youngblood, B.; Lindner, J.; Demidov, V. E.; Demokritov, S. O.; Krivorotov, I. N.
Nanowire spin torque oscillator driven by spin orbit torques
*Nature Communications **5**, 1 (2014)*
5. Fowley, C.; Sluka, V.; Bernert, K.; Lindner, J.; Fassbender, J.; Rippard, W. H.; Pufall, M. R.; Russek, S. E.; Deac, A. M.
Zero-field spin-transfer oscillators combining in-plane and out-of-plane magnetized layers
*Applied Physics Express **7**, 043001 (2014)*
6. Fu, Y.; Barsukov, I.; Meckenstock, R.; Lindner, J.; Zhai, Y.; Hjörvarsson, B.; Farle, M.
Uniaxial anisotropy and its manipulation in amorphous $Co_{68}Fe_{24}Zr_8$ thin films
*Journal of Applied Physics **115**, 172605 (2014)*
7. Gallardo, R. A.; Lenz, K.; Banholzer, A.; Körner, M.; Lindner, J.; Fassbender, J.; Landeros, P.
Splitting of spin-wave modes in thin films with Arrays of periodic perturbations: theory and experiment
*New Journal of Physics **16**, 023015 (2014)*
8. Greene, P. K.; Osten, J.; Lenz, K.; Fassbender, J.; Jenkins, C.; Arenholz, E.; Endo, T.; Iwata, N.; Liu, K.
Tuning perpendicular anisotropy gradient in Co/Pd multilayers by ion irradiation
*Applied Physics Letters **105**, 072401 (2014)*
9. Hamann, C.; Mattheis, R.; Mönch, I.; Fassbender, J.; Schultz, L.; McCord, J.
Magnetization dynamics of magnetic domain wall imprinted magnetic films
*New Journal of Physics **16**, 023010 (2014)*
10. Hassdenteufel, A.; Schubert, C.; Hebler, B.; Schultheiss, H.; Fassbender, J.; Albrecht, M.; Bratschitsch, R.
All-optical helicity dependent magnetic switching in Tb-Fe thin films with a MHz laser

oscillator
*Optics Express **22**, 10017 (2014)*

11. Hassdenteufel, A.; Schubert, C.; Schmidt, J.; Richter, P.; Zahn, D. R. T.; Salvan, G.; Helm, M.; Bratschitsch, R.; Albrecht, M.
Dependence of all-optical magnetic switching on the sublattice magnetization orientation in Tb-Fe thin films
*Applied Physics Letters **105**, 112403 (2014)*

12. Jakubisova-Liskova, E.; Visnovsky, S.; Wawro, A.; Baczewski, L. T.; Mazalski, P.; Maziewski, A.; Liedke, M. O.; McCord, J.; Fassbender, J.
Effect of Ga^+ irradiation in molecular-beam epitaxy grown Pt/Co/Pt thin films studied by magneto-optic spectroscopy
*Journal of Applied Physics **115**, 17C106 (2014)*

13. Khalid, M.; Prucnal, S.; Liedke, M. O.; Gao, K.; Facsko, S.; Skorupa, W.; Helm, M.; Zhou, S.
Synthesis and characterization of MnAs and MnP nanoclusters embedded in III–V semiconductors
*Materials Research Express **1**, 026105 (2014)*

14. Khalid, M.; Weschke, E.; Skorupa, W.; Helm, M.; Zhou, S.
Ferromagnetism and impurity band in a magnetic semiconductor: InMnP
*Physical Review B **89**, 121301(R) (2014)*

15. Körner, M.; Röder, F.; Lenz, K.; Fritzsche, M.; Lindner, J.; Lichte, H.; Fassbender, J.
Quantitative imaging of the magnetic configuration of modulated nanostructures by electron holography
*Small **10**, 5161 (2014)*

16. Langer, M.; Neudert, A.; Mönch, J. I.; Mattheis, R.; Lenz, K.; Fassbender, J.; McCord, J.
Magneto-optical analysis of stripe elements embedded in a synthetic antiferromagnet
*Physical Review B **89**, 064411 (2014)*

17. Maziewski, A.; Fassbender, J.; Kisielewski, J.; Kisielewski, M.; Kurant, Z.; Mazalski, P.; Stobiecki, F.; Stupakiewicz, A.; Sveklo, I.; Tekielak, M.; Wawro, A.; Zablotskii, V.
Magnetization states and magnetization processes in nanostructures: From a single layer to multilayers
*Physica Status Solidi (A) **211**, 1005 (2014)*

18. Möller, M.; Lenz, K.; Lindner, J.
Frequency-Domain Magnetic Resonance—Alternative Detection Schemes for Samples at the Nanoscale
*Journal of Surfaces and Interfaces of Materials **2**, 46 (2014)*

19. Ney, V.; Lenz, K.; Ollefs, K.; Wilhelm, F.; Rogalev, A.; Ney, A.
Role of preparation and implantation-related defects for the magnetic properties of $Zn_{0.9}Co_{0.1}O$ epitaxial films
*Journal of Applied Physics **116**, 043912 (2014)*

20. Osten, J.; Lenz, K.; Henschke, A.; Lindner, J.; Fassbender, J.
Simultaneous measurement of anisotropic magnetoresistance and observation of magnetic domains by Kerr microscopy
*Review of Scientific Instruments **85**, 123701 (2014)*

21. Pirro, P.; Sebastian, T.; Brächer, T.; Serga, Alexander A.; Kubota, T.; Naganuma, H.; Oogane, M.; Ando, Y.; Hillebrands, B.
Non-Gilbert-damping Mechanism in a Ferromagnetic Heusler Compound Probed by Nonlinear Spin Dynamics
*Physical Review Letters **113**, 227601 (2014)*

22. Roshchupkina, O. D.; Strache, T.; McCord, J.; Muecklich, A.; Baehtz, C.; Grenzer, J.
Structural modifications of thin magnetic Permalloy films induced by ion implantation and thermal annealing, a comparison
*Acta Materialia **74**, 278 (2014)*

23. Schoeppner, C.; Wagner, K.; Stienen, S.; Meckenstock, R.; Farle, M.; Narkowicz, R.; Suter, D.; Lindner, J.

Angular dependent ferromagnetic resonance analysis in a single micron sized cobalt stripe
*Journal of Applied Physics **116**, 033913 (2014)*

24. Schubert, C.; Hassdenteufel, A.; Matthes, P.; Schmidt, J.; Helm, M.; Bratschitsch, R.; Albrecht, M.
All-optical helicity dependent magnetic switching in an artificial zero moment magnet
*Applied Physics Letters **104**, 082406 (2014)*

25. Tahir, N.; Gieniusz, R.; Maziewski, A.; Bali, R.; Kostylev, M. P.; Wintz, S.; Schultheiss, H.; Facsko, S.; Potzger, K.; Lindner, J.; Fassbender, J.
Magnetization Reversal of Disorder Induced Ferromagnetic Regions in $Fe_{60}Al_{40}$ Thin Films
*IEEE Transactions on Magnetics **50**, 6101304 (2014)*

26. Trützschler, J.; Sentosun, K.; Langer, M.; Mönch, I.; Mattheis, R.; Fassbender, J.; McCord, J.
Optimization of magneto-resistive response of ion-irradiated Exchange biased films through zigzag arrangement of magnetization
*Journal of Applied Physics **115**, 103901 (2014)*

27. Vogt, K.; Fradin, F. Y.; Pearson, J. E.; Sebastian, T.; Bader, S. D.; Hillebrands, B.; Hoffmann, A.; Schultheiss, H.
Realization of a spin-wave multiplexer
*Nature Communications **5**, 3727 (2014)*

28. Wang, Y.; Chen, X.; Li, L.; Shalimov, A.; Tong, W.; Prucnal, S.; Munnik, F.; Yang, Z.; Skorupa, W.; Helm, M.; Zhou, S.
Structural and magnetic properties of irradiated SiC
*Journal of Applied Physics **115**, 17C104 (2014)*

29. Wang, Y.; Li, L.; Prucnal, S.; Chen, X.; Tong, W.; Yang, Z.; Munnik, F.; Potzger, K.; Skorupa, W.; Gemming, S.; Helm, M.; Zhou, S.
Disentangling defect-induced ferromagnetism in SiC
*Physical Review B **89**, 014417 (2014)*

30. Wang, Y.; Pochet, P.; Jenkins, C. A.; Arenholz, E.; Bukalis, G.; Gemming, S.; Helm, M.; Zhou, S.
Defect-induced magnetism in graphite through neutron irradiation
*Physical Review B **90**, 214435 (2014)*

31. Yildirim, O.; Butterling, M.; Cornelius, S.; Mikhailovskiy, Yu.; Novikov, A.; Semisalova, A.; Orlov, A.; Gan'Shina, E.; Perov, N.; Anwand, W.; Wagner, A.; Potzger, K.; Granovsky, A. B.; Smekhova, A.
Ferromagnetism and structural defects in V-doped titanium dioxide
*Physica Status Solidi (C) **11**, 1106 (2014)*

32. Yuan, Y; Wang, Y.; Khalid, M.; Gao, K.; Prucnal, S.; Gordan, O. D.; Salvan, G.; Zahn, D. T.; Skorupa, W.; Helm, M.; Zhou, S.
Ferromagnetic GaMnP Prepared by Ion Implantation and Pulsed Laser Annealing
*IEEE Transactions on Magnetics **50**, 2401304 (2014)*

33. Zhou, S.
Defect-induced ferromagnetism in semiconductors: a controllable approach by particle irradiation
*Nuclear Instruments and Methods in Physics Research B **326**, 55 (2014)*

Nanoscience and materials for information technologies

34. Bhattacharyya, J.; Zybell, S.; Eßer, F.; Helm, M.; Schneider, H.; Schneebeli, L.; Böttge, C. N.; Breddermann, B.; Kira, M.; Koch, S. W.
Magnetic control of Coulomb scattering and terahertz transitions among excitons
*Physical Review B **89**, 125313 (2014)*

35. Biermanns, A.; Dimakis, E.; Davydok, A.; Sasaki, T.; Geelhaar, L.; Takahasi, M.; Pietsch, U.
Role of liquid indium in the structural purity of wurtzite InAs nanowires that grow on

Si(111)
*Nano Letters **14**, 6878 (2014)*

36. Bischoff, L.; Böttger, R.; Heinig, K.-H.; Facsko, S.; Pilz, W.
Surface patterning of GaAs under irradiation with very heavy polyatomic Au ions
*Applied Surface Science **310**, 154 (2014)*

37. Bogusz, A.; Müller, A. D.; Blaschke, D.; Skorupa, I.; Bürger, D.; Scholz, A.; Schmidt, O. G.; Schmidt, H.
Resistive switching in polycrystalline $YMnO_3$ thin films
*AIP Advances **4**, 107135 (2014)*

38. Fiedler, J.; Heera, V.; Hübner, R.; Voelskow, M.; Germer, S.; Schmidt, B.; Skorupa, W.
High-fluence Ga-implanted silicon – the effect of annealing and cover layers
*Journal of Applied Physics **116**, 024502 (2014)*

39. Gao, K.; Prucnal, S.; Hübner, R.; Bähtz, C.; Skorupa, I.; Wang, Y.; Skorupa, W.; Helm, M.; Zhou, S.
$Ge_{(1-x)}Sn_{(x)}$ alloys synthesized by ion implantation and pulsed laser melting
*Applied Physics Letters **105**, 042107 (2014)*

40. Gao, K.; Prucnal, S.; Skorupa, W.; Helm, M.; Zhou, S.
Formation and photoluminescence of $GaAs_{1-x}N_x$ dilute nitride achieved by N-implatation and flash lamp annealing
*Applied Physics Letters **105**, 012107 (2014)*

41. Heera, V.; Fiedler, J.; Naumann, M.; Skrotzki, R.; Kölling, S.; Wilde, L.; Herrmannsdörfer, T.; Skorupa, W.; Wosnitza, J.; Helm, M.
Depth-resolved transport measurements and atom-probe tomography of heterogeneous, superconducting Ge:Ga films
*Superconductor Science and Technology **27**, 055025 (2014)*

42. Henke, T.; Bartha, J. W.; Rebohle, L.; Merkel, U.; Hübner, R.; Albert, M.; Skorupa, W.
Formation of regularly arranged large grain silicon islands by using embedded micro mirrors in the flash crystallization of amorphous silicon
*Journal of Applied Physics **115**, 034301 (2014)*

43. Kadi, F.; Winzer, T.; Malic, E.; Knorr, A.; Göttfert, F.; Mittendorff, M.; Winnerl, S.; Helm, M.
Microscopic Description of Intraband Absorption in Graphene: The Occurrence of Transient Negative Differential Transmission
*Physical Review Letters **113**, 035502 (2014)*

44. Kaspar, T.; Fiedler, J.; Skorupa, I.; Bürger, D.; Schmidt, O. G.; Schmidt, H.
Transport in ZnCoO thin films with stable bound magnetic polarons
*APL Materials **2**, 076101 (2014)*

45. Krause, M.; Buljan, M.; Mücklich, A.; Möller, W.; Fritzsche, M.; Facsko, S.; Heller, R.; Zschornak, M.; Wintz, S.; Endrino, J. L.; Baehtz, C.; Shalimov, A.; Gemming, S.; Abrasonis, G.
Compositionally modulated ripples during composite film growth: three-dimensional pattern formation at the nanoscale
*Physical Review B **89**, 085418 (2014)*

46. Lorenz, T.; Joswig, J.-O.; Seifert, G.
Two-dimensional and tubular structures of misfit compounds: Structural and electronic properties
*Beilstein Journal of Nanotechnology **5**, 2171 (2014)*

47. Mironov, O. A.; Hassan, A. H. A.; Morris, R. J. H.; Dobbie, A.; Uhlarz, M.; Chrastina, D.; Hague, J. P.; Kiatgamolchai, S.; Beanland, R.; Gabani, S.; Berkutov, I. B.; Helm, M.; Drachenko, O.; Myronov, M.; Leadley, D. R.
Ultra high hole mobilities in a pure strained Ge quantum well
*Thin Solid Films **557**, 329 (2014)*

48. Mittendorff, M.; Orlita, M.; Potemski, M.; Berger, C.; de Heer, W. A.; Schneider, H.; Helm, M.; Winnerl, S.
Intraband carrier dynamics in Landau-quantized multilayer epitaxial graphene
*New Journal of Physics **16**, 123021 (2014)*

49. Mittendorff, M.; Winzer, T.; Malic, E.; Knorr, A.; Berger, C.; de Heer, Walter A.; Schneider, H.; Helm, M.; Winnerl, S.
Anisotropy of excitation and relaxation of photogenerated charge carriers in graphene
*Nano Letters **14**, 1504 (2014)*

50. Nerowski, A.; Pötschke, M.; Wiesenhütter, U.; Nicolai, J.; Cikalova, U.; Dianat, A.; Erbe, A.; Opitz, J.; Bobeth, M.; Baraban, L.; Cuniberi, G.
Effect of Waveform of ac Voltage on the Morphology and Crystallinity of Electrochemically Assembled Platinum Nanowires
*Langmuir **30**, 5655 (2014)*

51. Nietiadi, M. L.; Sandoval, L.; Urbassek, Herbert M.; Möller, W.
Sputtering of Si nanospheres
*Physical Review B **90**, 045417 (2014)*

52. Ódor, G.; Kelling, J.; Gemming, S.
Aging of the (2+1)-dimensional Kardar-Parisi-Zhang model
*Physical Review E **89**, 032146 (2014)*

53. Pan, W.; Dimakis, E.; Wang, G. T.; Moustakas, T. D.; Tsui, D. C.
Two-dimensional electron gas in monolayer InN quantum wells
*Applied Physics Letters **105**, 213503 (2014)*

54. Philipp, P.; Bischoff, L.; Treske, U.; Schmidt, B.; Fiedler, J.; Hübner, R.; Klein, F.; Koitzsch, A.; Mühl, T.
The origin of conductivity in ion-irradiated diamond-like carbon – Phase transformation and atomic ordering
*Carbon **80**, 677 (2014)*

55. Prucnal, S.; Gao, K.; Zhou, S.; Wu, J.; Cai, H.; Gordan, O. D.; Zahn, D. R. T.; Larkin, G.; Helm, M.; Skorupa, W.
Optoelectronic properties of ZnO film on silicon after SF6 plasma treatment and milliseconds annealing
*Applied Physics Letters **105**, 221903 (2014)*

56. Prucnal, S.; Glaser, M.; Lugstein, A.; Bertagnolli, E.; Stöger-Pollach, M.; Zhou, S.; Helm, M.; Reichel, D.; Rebohle, L.; Turek, M.; Zuk, J.; Skorupa, W.
III–V semiconductor nanocrystal formation in silicon nanowires via liquid-phase epitaxy
*Nano Research **7**, 1769 (2014)*

57. Prucnal, S.; Jiao, F.; Reichel, D.; Zhao, K.; Cornelius, S.; Turek, M.; Pyszniak, K.; Drozdziel, A.; Skorupa, W.; Helm, M.; Zhou, S.
Influence of Flash Lamp Annealing on the Optical Properties of CIGS Layer
*Acta Physica Polonica A **125**, 1404 (2014)*

58. Prucnal, S.; Zhou, S.; Ou, X.; Facsko, S.; Liedke, M. O.; Bregolin, F.; Liedke, B.; Grebing, J.; Fritzsche, M.; Hübner, R.; Mücklich, A.; Rebohle, L.; Helm, M.; Turek, M.; Drozdziel, A.; Skorupa, W.
III-V/Si on silicon-on-insulator platform for hybrid nanoelectronics
*Journal of Applied Physics **115**, 074306 (2014)*

59. Putero, M.; Coulet, M.-V.; Muller, C.; Cohen, G.; Hopstaken, M.; Bähtz, C.; Raoux, S.
Density change upon crystallization of Ga-Sb films
*Applied Physics Letters **105**, 1819101 (2014)*

60. Rebohle, L.; Berencén, Y.; Wutzler, R.; Braun, M.; Hiller, D.; Ramírez, J. M.; Garrido, B.; Skorupa, W.; Helm, M.
The electroluminescence mechanism of Er^{3+} in different silicon oxide and silicon nitride environments
*Journal of Applied Physics **116**, 123104 (2014)*

61. Rebohle, L.; Braun, M.; Wutzler, R.; Liu, B.; Sun, J. M.; Helm, M.; Skorupa, W.
Strong electroluminescence from SiO_2-Tb_2O_3-Al_2O_3 mixed layers fabricated by atomic layer deposition
*Applied Physics Letters **104**, 251113 (2014)*

62. Teich, M.; Wagner, M.; Stehr, D.; Schneider, H.; Helm, M.; Böttge, C. N.; Klettke, A. C.; Chatterjee, S.; Kira, M.; Koch, S. W.; Khitrova, G.; Gibbs, H. M.
Systematic investigation of terahertz-induced excitonic Rabi splitting
*Physical Review B **89**, 115311 (2014)*

63. Tiagulskyi, S. I.; Nazarov, A. N.; Gordienko, S. O.; Vasin, A. V.; Rusavsky, A. V.; Rebohle, L.; Voelskow, M.; Skorupa, W.
Electroluminescent properties of Tb-doped carbon-enriched silicon oxide
*Semiconductor Physics, Quantum Electronics & Optoelectronics **17**, 34 (2014)*

64. Voelskow, M.; Endler, R.; Schumann, T.; Mücklich, A.; Ou, X.; Liepack, E. H.; Gebel, T.; Peeva, A.; Skorupa, W.
Formation of dendritic crystal structures in thin silicon films on silicon dioxide by carbon ion implantation and high intensity large area flash lamp irradiation
*Journal of Crystal Growth **388**, 70 (2014)*

65. Wendumu, T. B.; Seifert, G.; Lorenz, T.; Joswig, J.-O.; Enyashin, A.
Optical properties of triangular molybdenum disulfide nanoflakes
*The Journal of Physical Chemistry Letters **5**, 3636 (2014)*

66. Wilhelm, R. A.; Gruber, E.; Ritter, R.; Heller, R.; Facsko, S.; Aumayr, F.
Charge Exchange and Energy Loss of Slow Highly Charged Ions in 1 nm Thick Carbon Nanomembranes
*Physical Review Letters **112**, 153201 (2014)*

67. Wylezich, H.; Mähne, H.; Rensberg, J.; Ronning, C.; Zahn, P.; Slesazeck, S.; Mikolajick, T.
Local Ion Irradiation Induced Resistive Threshold and Memory Switching in Nb2O5/NbOx Films
*ACS Applied Materials and Interfaces **6**, 17474 (2014)*

68. You, T.; Shuai, Y.; Luo, W.; Du, N.; Bürger, D.; Skorupa, I.; Hübner, R.; Henker, S.; Mayr, C.; Schüffny, R.; Mikolajick, T.; Schmidt, Oliver G.; Schmidt, H.
Exploiting Memristive $BiFeO_3$ Bilayer Structures for Compact Sequential Logics
*Advanced Functional Materials **24**, 3357 (2014)*

69. Zybell, S.; Bhattacharyya, J.; Winnerl, S.; Eßer, F.; Helm, M.; Schneider, H.; Schneebeli, L.; Böttge, C. N.; Kira, M.; Koch, S. W.; Andrews, A. M.; Strasser, G.
Characterizing intra-exciton Coulomb scattering in terahertz excitations
*Applied Physics Letters **105**, 201109 (2014)*

Materials for energy and transport technologies

70. Altstadt, E.; Keim, E.; Hein, H.; Serrano, M.; Bergner, F.; Viehrig, H.-W.; Ballesteros, A.; Chaouadi, R.; Wilford, K.
FP7 Project LONGLIFE: Overview of Results and Implications
*Nuclear Engineering and Design **278**, 753 (2014)*

71. Ballesteros, A.; Altstadt, E.; Gillemot, F.; Hein, H.; Wagemans, J.; Rouden, J.; Barthelmes, J.; Wilford, K.; Serrano, M.; Brumovsky, M.; Chaouadi, R.; Ortner, S.
Monitoring radiation embrittlement during life extension periods
*Nuclear Engineering and Design **267**, 197 (2014)*

72. Ballesteros, A.; Hein, H.; May, J.; Planman, T.; Todeschini, P.; Brumovsky, M.; Gillemot, F.; Chaouadi, R.; Rouden, J.; Efsing, P.; Altstadt, E.
Reactor pressure vessel surveillance
*Nuclear Engineering International **59**, 19 (2014)*

73. Bergner, F.; Pareige, C.; Hernández-Mayoral, M.; Malerba, L.; Heintze, C.
Application of a three-feature dispersed-barrier hardening model to neutron-irradiated Fe-Cr model alloys
*Journal of Nuclear Materials **448**, 96 (2014)*

74. Bergner, F.; Ulbricht, A.; Lindner, P.; Keiderling, U.; Malerba, L
Post-irradiation annealing behaviour of neutron-irradiated FeCu, FeMnNi and FeMnNiCu model alloys investigated by means of small-angle neutron scattering
*Journal of Nuclear Materials **454**, 22 (2014)*

75. Chen, C.; Richter, A.; Kögler, R.
The effect of dual Fe^+/He^+ ion beam irradiation on microstructural changes in FeCrAl ODS alloys
*Journal of Alloys and Compounds **586**, S173 (2014)*

76. Gokhman, A.; Caturla, M.; Bergner, F.
Damage accumulation in pure iron and high concentrated Fe–12.5 at% Cr alloy: comparison between object kinetic Monte Carlo and cluster dynamics
*Radiation Effects and Defects in Solids **169**, 185 (2014)*

77. Gonzalez-Arrabal, R.; Panizo-Laiz, M.; Gordillo, N.; Tejado, E.; Munnik, F.; Rivera, A.; Perlado, J. M.
Hydrogen accumulation in nanostructured as compared to coarse-grained tungsten
*Journal of Nuclear Materials **453**, 287 (2014)*

78. Götze, A.; Makowski, S.; Kunze, T.; Hübner, M.; Zellbeck, H.; Weihnacht, V.; Leson, A.; Beyer, E.; Joswig, J.-O.; Seifert, G.; Abrasonis, G.; Posselt, M.; Fassbender, J.; Gemming, S.; Krause, M.
Tetrahedral amorphous carbon coatings for friction reduction of the valve train in internal combustion engines
*Advanced Engineering Materials **16**, 1226 (2014)*

79. Hanzig, J.; Zschornak, M.; Nentwich, M.; Hanzig, F.; Gemming, S.; Leisegang, T.; Meyer, D. C.
Strontium titanate: An all-in-one rechargeable energy storage material
*Journal of Power Sources **267**, 700 (2014)*

80. Hernández-Mayoral, M.; Serrano, M.; Oñorbe, E.; García-Junceda, A.; Hilger, I.; Kloeden, B.; Weissgaerber, T.; Ulbricht, A.; Bergner, F.; Radiguet, B.; Etienne, A.; Shariq, A.; Dewhurst, C. D.
Microstructural and mechanical characterisation of ODS ferritic alloys produced by mechanical alloying and spark plasma sintering
*Materials Science and Technology **30**, 1669 (2014)*

81. Hilger, I.; Tegel, M.; Gorley, M. J.; Grant, P. S.; Weißgärber, T.; Kieback, B.
The Structural changes of Y_2O_3 in ferritic ODS alloys during milling
*Journal of Nuclear Materials **447**, 242 (2014)*

82. Jantschner, O.; Field, S. K.; Music, D.; Terziyska, V. L.; Schneider, J. M.; Munnik, F.; Zorn, K.; Mitterer, C.
Sputtered Si-containing low-friction carbon coatings for elevated temperatures
*Tribology International **77**, 15 (2014)*

83. Kunze, T.; Posselt, M.; Gemming, S.; Konicek, A. R.; Carpick, R. W.; Pastewka, L.; Moseler, M.
Wear, Plasticity, and Rehybridization in Tetrahedral Amorphous Carbon
*Tribology Letters **53**, 119 (2014)*

84. Linse, T.; Kuna, M.; Viehrig, H.-W.
Quantification of brittle-ductile failure behavior of ferritic reactor pressure vessel steels using the Small-Punch-Test and micromechanical damage models
*Materials Science and Engineering A **614**, 136 (2014)*

85. Lipp Bregolin, F.; Krockert, K.; Prucnal, S.; Vines, L.; Hübner, R.; Svensson, B. G.; Wiesenhütter, K.; Möller, H.-J.; Skorupa, W.
Hydrogen engineering via plasma immersion ion implantation and flash lamp annealing in silicon-based solar cell substrates
*Journal of Applied Physics **115**, 064505 (2014)*

86. Ou, X.; Anwand, W.; Kögler, R.; Zhou, H.; Richter, A.
The role of helium implantation induced vacancy defect on hardening of tungsten
*Journal of Applied Physics **115**, 123521 (2014)*

87. Perez-Flores, J. C.; Baehtz, C.; Kuhna, A.; Garcia-Alvaradoa, F.
Hollandite-type TiO_2: a new negative electrode material for sodium-ion batteries
*Journal of Materials Chemistry A **2**, 1825 (2014)*

88. Pillaca, E. J. D. M.; Ueda, M.; Reuther, H.; Lepienski, C. M.
Study of the effects of plasma immersion ion implantation on austenitic stainless steel using E × B fields
*Surface & Coatings Technology **246**, 1 (2014)*

89. Posselt, M.; Murali, D.; Panigrahi, B. K.
Energetics, structure, and composition of nanoclusters in Oxide Dispersion Strenghtened Fe-Cr alloys
*Modelling and Simulation in Materials Science and Engineering **22**, 085003 (2014)*

90. Schindler, H.-J.; Kalkhof, D.; Viehrig, H.-W.
Effect of notch acuity on the apparent fracture toughness
*Engineering Fracture Mechanics **129**, 26 (2014)*

91. Schindler, H.-J.; Kalkhof, D.; Viehrig, H.-W.
Variability and lower bound of fracture toughness of welds in the ductile to brittle transition regime
*Procedia Materials Science **3**, 732 (2014)*

92. Viehrig, H.-W.; Houska, M.; Altstadt, E.
Radiation and annealing response of WWER 440 beltline welding seams
*Journal of Nuclear Materials **456**, 334 (2015)*

93. Yankov, R. A.; Kolitsch, A.; von Borany, J.; Munnik, F.; Mücklich, A.; Gemming, S.; Alexewicz, A.; Bracht, H.; Rösner, H.; Donchev, A.; Schütze, M.
Microstructural studies of fluorine-implanted titanium aluminides for enhanced environmental durability
*Advanced Engineering Materials **16**, 52 (2014)*

Other topics and external users of ion beam center and free-electron laser

94. Al-Abdullah, T.; Akhmadaliev, Sh.; Ayranov, M.; Bemmerer, D.; Dressler, R.; Elekes, Z.; Kivel, N.; Schmidt, K.; Schumann, D.; Sobiella, M.; Stowasser, T.; Takacs, M. P.; Zuber, K.
The Feasibility of direct measurement of the 44Ti(α, p)47V and 40Ca(α, p)43Sc reactions in forward kinematics at astrophysically relevant temperatures
*European Physical Journal A **50**, 140 (2014)*

95. Alexandru, M.; Florentin, M.; Constant, A.; Schmidt, B.; Michel, P.; Godignon, P.
5 MeV Proton and 15 MeV Electron Radiation Effects Study on 4H-SiC nMOSFET Electrical Parameters
*IEEE Transactions on Nuclear Science **61**, 1732 (2014)*

96. Asgekar, V.; Geloni, G. A.; Kocharyan, V.; Stojanovice, N.; Michel, P.; Gensch, M.
Interference effects in super-radiant THz sources
*Infrared Physics and Technology **64**, 26 (2014)*

97. Balaji, S.; Panigrahi, B. K.; Saravanan, K.; David, C.; Amirthapandian, S.; Kalavathi, S.; Nair, K. G. M.; Hübner, R.
Ion beam shaping of embedded metal nanoparticles by Si^+ ion irradiation
*Applied Physics A **116**, 1595 (2014)*

98. Barth, T.; Preuß, J.; Müller, G.; Hampel, U.
Single particle resuspension experiments in turbulent channel flows
*Journal of Aerosol Science **71**, 40 (2014)*

99. Bayer, B. C.; Bähtz, C.; Kidambi, P. R.; Weatherup, R. S.; Mangler, C.; Kotakoski, J.; Goddard, C. J. L.; Caneva, S.; Cabrero-Vilatela, A.; Meyer, J. C.; Hofmann, S.
Nitrogen controlled iron catalyst phase during carbon nanotube growth
*Applied Physics Letters **105**, 1431111 (2014)*

100. Behera, A. K.; Facsko, S.; Bandyopadyay, M. K.; Das, S.; Chatterjee, S.
Amorphization and recrystallization of single-crystalline hydrogen titanate nanowires by N^+ ion irradiation
*Journal of Applied Physics **115**, 233505 (2014)*

101. Bommali, R. K.; Modi, M. H.; Zhou, S.; Ghosh, S.; Srivastava, P.
Study of growth kinetics and depth resolved composition of a-SiN x:H thin films by resonant soft X-ray reflectivity at the Si L 2,3-edge
*Applied Surface Science **305**, 173 (2014)*

102. Bommali, R.; Ghosh, S.; Prakash, G. V.; Gao, K.; Zhou, S.; Khan, S. A.; Srivastava, P.
Hydrogen Plasma Induced Modification of Photoluminescence from a-SiN(x):H Thin Films
*Journal of Applied Physics **115**, 053525 (2014)*

103. Buchta, K.; Lewandowski, M.; Bischoff, L.; Synoradzki, K.; Błaszyk, M.; Toliński, T.; Luciński, T.
Magnetization reversal in Co zigzag nanocolumns grown by glancing angle deposition
*Thin Solid Films **568**, 13 (2014)*

104. Bussone, G.; Dimakis, E.; Grifone, R.; Biermanns, A.; Tahraoui, A.; Carbone, D.; Geelhaar, L.; Schülli, T. U.; Pietsch, U.
Impact of strain induced by polymer curing in benzocyclobutene embedded semiconductor nanostructures
*Physica Status Solidi (RRL) **8**, 1007 (2014)*

105. But, D. B.; Drexler, C.; Sakhno, M. V.; Dyakonova, N.; Drachenko, O.; Sizov, F. F.; Gutin, A.; Ganichev, S. D.; Knap, W.
Nonlinear photoresponse of field effect transistors terahertz detectors at high irradiation intensities
*Journal of Applied Physics **115**, 164514 (2014)*

106. Cavaleiro, A. J.; Ramos, A. S.; Martins, R. M. S.; Bähtz, C.; Vieira, M. T.; Braz Fernandes, F. M.
In Situ Phase Evolution of Ni/Ti Reactive Multilayers
*Journal of Materials Engineering and Performance **23**, 2446 (2014)*

107. Chen, Y. N.; Xu, S. J.; Zheng, C. C.; Ning, J. Q.; Ling, F. C. C.; Anwand, W.; Brauer, G.; Skorupa, W.
Nature of red luminescence band in research-grade ZnO single crystals: A “self-activated” configurational transition
*Applied Physics Letters **105**, 041912 (2014)*

108. Cheng, Y.; Jia, Y.; Akhmadaliev, Sh.; Zhou, S.; Chen, F.
Guided-wave phase-matched second-harmonic generation in $KTiOPO_4$ waveguide produced by swift heavy-ion irradiation
*Optical Engineering **53**, 117102 (2014)*

109. Dekov, V. M.; Egueh, N. M.; Kamenov, G. D.; Bayon, G.; Lalonde, S. V.; Schmidt, M.; Liebetrau, V.; Munnik, F.; Fouquet, Y.; Tanimizu, M.; Awaleh, M. O.; Guirreh, I.; Le Gall, B.
Hydrothermal carbonate chimneys from a continental rift (Afar Rift): Mineralogy, geochemistry, and mode of formation
*Chemical Geology **387**, 87 (2014)*

110. Deßmann, N.; Pavlov, S. G.; Shastin, V. N.; Zhukavin, R. Kh.; Tsyplenkov, V. V.; Winnerl, S.; Mittendorff, M.; Abrosimov, N. V.; Riemann, H.; Hübers, H.-W.
Time-resolved electronic capture in n-type germanium doped with antimony
*Physical Review B **89**, 035205 (2014)*

111. Döring, J.; von Ribbeck, H.-G.; Fehrenbacher, M.; Kehr, S. C.; Eng, L. M.
Near-field resonance shifts of ferroelectric barium titanate domains upon low-temperature phase transition
*Applied Physics Letters **105**, 053109 (2014)*

112. El-Said, A. S.; Heller, R.; Wilhelm, R.; Facsko, S.; Aumayr, F.
Surface modifications of BaF_2 and CaF_2 single crystals by slow highly charged ions
*Applied Surface Science **310**, 169 (2014)*

113. El-Said, A. S.; Moslem, W. M.; Djebli, M.
Surface nanostructuring by ion-induced localized plasma expansion in zinc oxide
Applied Physics Letters ***104****, 231609 (2014)*

114. El-Said, A. S.; Wilhelm, R. A.; Heller, R.; Ritter, R.; Wachter, G.; Facsko, S.; Lemell, C.; Burgdörfer, J.; Aumayr, F.
Nanostructuring CaF_2 surfaces with slow highly charged ions
Journal of Physics: Conference Series ***488****, 012002 (2014)*

115. Engler, M.; Frost, F.; Müller, S.; Macko, S.; Will, M.; Feder, R.; Spemann, D.; Hübner, R.; Facsko, S.; Michely, T.
Silicide induced ion beam patterning of Si(001)
Nanotechnology ***25****, 115303 (2014)*

116. Gaiduk, P. I.; Lundsgaard Hansen, J.; Larsen, A. N.; Korolik, O. V.; Bregolin, F. L.; Skorupa, W.
Carbon redistribution and precipitation in high temperature ion-implanted strained Si/SiGe/Si multi-layered structures
Microelectronic Engineering ***125****, 8 (2014)*

117. Gaiduk, P. I.; Lundsgaard Hansen, J.; Nylandsted Larsen, A.; Bregolin, F. L.; Skorupa, W.
Suppression of tin precipitation in SiSn alloy layers by implanted carbon
Applied Physics Letters ***104****, 231903 (2014)*

118. Gruber, W.; Rahn, J.; Bähtz, C.; Horisberger, M.; Geckle, U.; Schmidt, H.
Influence of a passivation layer on strain relaxation and lattice disorder in thin nano-crystalline Pt films during in-situ annealing
Thin Solid Films ***565****, 79 (2014)*

119. Hao, M. R.; Yang, Y.; Zhang, S.; Shen, W. Z.; Schneider, H.; Liu, H. C.
Near-room-temperature photon-noise-limited quantum well infrared photodetector
Laser & Photonics Reviews ***8****, 297 (2014)*

120. Hao, M. R.; Zhang, S.; Zhang, Y. H.; Shen, W. Z.; Schneider, H.; Liu, H. C.
Re-examining the doping effect on the performance of quantum well infrared photodetectors
IEEE Journal of Quantum Electronics ***50****, 3 (2014)*

121. He, C. W.; Dawi, K.; Platteau, C.; Barthe, M. F.; Desgardin, P.; Akhmadaliev, Sh.
Vacancy type defect formation in irradiated α-iron investigated by positron beam Doppler broadening technique
Journal of Physics: Conference Series ***505****, 012018 (2014)*

122. Hinrichs, K.; Furchner, A.; Sun, G.; Gensch, M.; Rappich, J.; Oates, T.
Infrared ellipsometry for improved laterally resolved analysis of thin films
Thin Solid Films ***571****, 648 (2014)*

123. Husar, R.; Hübner, R.; Hennig, C.; Martin, P. M.; Chollet, M.; Weiss, S.; Zänker, H.; Stumpf, T.; Ikeda-Ohno, A.
Intrinsic formation of nanocrystalline neptunium dioxide under neutral aqueous conditions relevant to deep geological repositories
Chemical Communications ***51****, 1301 (2015)*

124. Jercinovic, M.; Radic, N.; Buljan, M.; Grenzer, J.; Delac-Marion, I.; Kralj, M.; Bogdanovic-Radovic, I.; Hübner, R.; Dubcek, P.; Salamon, K.; Bernstorff, S.
Self-assembled growth of Ni nanoparticles in amorphous alumina matrix
Journal of Nanoparticle Research ***16****, 2296 (2014)*

125. Jia, J. Y.; Gao, J. H.; Hao, M. R.; Wang, T. M.; Shen, W. Z.; Zhang, Y. H.; Cao, J. C.; Guo, X. G.; Schneider, H.
Dark current mechanism of terahertz quantum-well photodetectors
Journal of Applied Physics ***116****, 154501 (2014)*

126. Kauffmann-Weiss, S.; Hamann, S.; Reichel, L.; Siegel, A.; Alexandrakis, V.; Heller, R.; Schultz, L.; Ludwig, A.; Fähler, S.
The Bain library: A Cu-Au buffer template for a continuous variation of lattice parameters in epitaxial films
APL Materials ***2****, 046107 (2014)*

127. Keller, A.; Rackwitz, J.; Cauet, E.; Liévin, J.; Körzdörfer, T.; Rotaru, A.; Gothelf, K. V.; Besenbacher, F.; Bald, I.
Sequence dependence of electron-induced DNA strand breakage revealed by DNA nanoarrays
*Scientific Reports **4**, 7391 (2014)*

128. Khanbabaee, B.; Facsko, S.; Doyle, S.; Pietsch, U.
Near-surface density profiling of Fe ion irradiated Si (100) using extremely asymmetric x-ray diffraction by variation of the wavelength
*Applied Physics Letters **105**, 163101 (2014)*

129. Khanbabaee, B.; Lützenkirchen-Hecht, D.; Hübner, R.; Grenzer, J.; Facsko, S.; Pietsch, U.
Near surface silicide formation after off-normal Fe-implantation of Si(001) surfaces
*Journal of Applied Physics **116**, 024301 (2014)*

130. Kidambi, P. R.; Blume, R.; Kling, J.; Wagner, J. B.; Bähtz, C.; Weatherup, R. S.; Schloegl, R.; Bayer, B. C.; Hofmann, S.
In Situ Observations during Chemical Vapor Deposition of Hexagonal Boron Nitride on Polycrystalline Copper
*Chemistry of Materials **26**, 6380 (2014)*

131. König, G.; Thorn, M.; Zschornack, J.; Schmidt, A.
A Compact, Versatile Low-Energy Electron Beam Ion Source
*Review of Scientific Instruments **85**, 02B703 (2014)*

132. Kopyra, J.; Keller, A.; Bald, I.
On the role of fluoro-substituted nucleosides in DNA radiosensitization for tumor radiation therapy
*RSC Advances **4**, 6825 (2014)*

133. Kosmata, M.; Munnik, F.; Hanf, D.; Grötzschel, R.; Richter, S.; Möller, W.
Oxygen depth profiling with subnanometre depth resolution
*Nuclear Instruments and Methods in Physics Research B **337**, 27 (2014)*

134. Kumar, P.; Saxena, N.; Chandra, R.; Gao, K.; Zhou, S.; Agarwal, A.; Singh, F.; Gupta, V.; Kanjilal, D.
SHI induced enhancement in green emission from nanocrystalline CdS thin films for photonic applications
*Journal of Luminescence **147**, 184 (2014)*

135. Lipp Bregolin, F.; Franzen, P.; Boudinov, H.; Sias, Uilson S.; Behar, M.
Low temperature and decay lifetime photoluminescence of Eu and Tb nanoparticles embedded into SiO_2
*Journal of Luminescence **153**, 144 (2014)*

136. Liu, G.; He, R.; Akhmadaliev, Sh.; de Aldana, J.; Zhou, S.; Chen, F.
Optical waveguides in LiTaO3 crystals fabricated by swift C^{5+} ion irradiation
*Nuclear Instruments and Methods in Physics Research B **325**, 43 (2014)*

137. Liu, H.; Jia, Y.; Ren, Y.; Akhmadaliev, Sh.; Zhou, S.; Chen, F.
Green up-conversion of swift C^{5+} ion irradiated planar waveguide in Er^{3+}, MgO codoped nearly stoichiometric $LiNbO_3$ crystal
*Nuclear Instruments and Methods in Physics Research B **320**, 22 (2014)*

138. Luan, Q.; Jia, Y.; Wang, Y.; Akhmadaliev, Sh.; Zhou, S.; de Aldana, J.; Tan, Y.; Chen, F.
Optical ridge waveguides in 4H-SiC single crystal produced by combination of carbon ion irradiation and femtosecond laser ablation
*Optical Materials Express **4**, 1166 (2014)*

139. Macková, A.; Malinsky, P.; Pupíková, H.; Nekvindová, P.; Cajzl, J.; Sofer, Z.; Wilhelm, R. A.; Kolitsch, A.; Oswald, J.
The structural changes and optical properties of $LiNbO_3$ after Er implantation using high ion fluencies
*Nuclear Instruments and Methods in Physics Research B **332**, 74 (2014)*

140. Mackova, A.; Malinsky, P.; Pupikova, H.; Nekvindova, P.; Cajzl, J.; Svecova, B.; Oswald, J.; Wilhelm, R. A.; Kolitsch, A.

A comparison of the structural changes and optical properties of $LiNbO_3$, Al_2O_3 and ZnO after Er^+ ion implantation
*Nuclear Instruments and Methods in Physics Research B **331**, 182 (2014)*

141. Macková, A.; Malinsky, P.; Sofer, Z.; Šimek, P.; Sedmidubsky, D.; Mikulics, M.; Wilhelm, R. A.
A study of the structural and magnetic properties of ZnO implanted by Gd ions
*Nuclear Instruments and Methods in Physics Research B **332**, 80 (2014)*

142. Markwitz, A.; Mohr, B.; Carpeño, D. F.; Hübner, R.
Ultra-smooth diamond-like carbon coatings with high elasticity deposited at low temperature by direct ion beam deposition
*Surface & Coatings Technology **258**, 956 (2014)*

143. Menéndez, E.; Templier, C.; Abrasonis, G.; Lopez-Barbera, J. F.; Nogués, J.; Temst, K.; Sortef, J.
A combinatorial study of the mechanical and magnetic properties of a gradually nitrided austenitic stainless steel single crystal
*CrystEngComm **16**, 3515 (2014)*

144. Merchel, S.; Mrak, I.; Braucher, R.; Benedetti, L.; Repe, B.; Bourlès, D. L.; Reitner, J. M.
Surface exposure dating of the Veliki vrh rock avalanche in Slovenia associated with the 1348 earthquake
*Quaternary Geochronology **22**, 33 (2014)*

145. Meunier, C.; Vives, S.; Munnik, F.; Berthout, G.; Mikhailov, S.
Effect on microstructure and hardness of 1 MeV carbon ion implantation in Al, Co and W
*Surface & Coatings Technology **262**, 191 (2015)*

146. Möller, W.
TRI3DYN – Collisional computer simulation of the dynamic evolution of 3-dimensional nanostructures under ion irradiation
*Nuclear Instruments and Methods in Physics Research B **222**, 23 (2014)*

147. Neelmeijer, C.; Pietsch, U.; Ulbricht, H.
Eighteenth-Century Meissen Porcelain reference data obtained by proton-beam analysis (PIXE-PIGE)
*Archaeometry **56**, 527 (2014)*

148. Okuyan, E.; Güdükbay, U.; Bulutay, C.; Heinig, K.-H.
MaterialVis: Material visualization tool using direct volume and surface rendering techniques
*Journal of Molecular Graphics and Modelling **50**, 50 (2014)*

149. Opherden, L.; Oertel, J.; Barkleit, A.; Fahmy, K.; Keller, K.
Paramagnetic Decoration of DNA origami Nanostructures by Eu^{3+} Coordination
*Langmuir **30**, 8152 (2014)*

150. Ott, U.; Merchel, S.; Herrmann, S.; Pavetich, S.; Rugel, G.; Faestermann, T.; Fimiani, L.; Gomez-Guzman, José M.; Hain, K.; Korschinek, G.; Ludwig, P.; D'Orazio, M.; Folco, L.
Cosmic ray exposure and pre-atmospheric size of the Gebel Kamil iron meteorite
*Meteoritics & Planetary Science **49**, 1365 (2014)*

151. Pavetich, S.; Akhmadaliev, Sh.; Arnold, M.; Aumaître, G.; Bourlès, D.; Buchriegler, J.; Golser, R.; Keddadouche, K.; Martschini, M.; Merchel, S.; Rugel, G.; Steier, P.
Interlaboratory study of the ion source memory effect in ^{36}Cl accelerator mass spectrometry
*Nuclear Instruments and Methods in Physics Research B **329**, 22 (2014)*

152. Pavlov, S. G.; Deßmann, N.; Shastin, V. N.; Zhukavin, R. Kh.; Redlich, B.; van der Meer, A. F. G.; Mittendorff, M.; Winnerl, S.; Abrosimov, N. V.; Riemann, H.; Hübers, H.-W.
Terahertz Stimulated Emission from Silicon Doped by Hydrogenlike Acceptors
*Physical Review X **4**, 021009 (2014)*

153. Persechini, L.; Verre, R.; Mcalinden, N.; Wang, J.; Ranjan, M.; Facsko, S.; Shvets, I.; Mcgilp, J.
An analytic approach to modeling the optical response of anisotropic nanoparticle arrays at surfaces and interfaces
*Journal of Physics: Condensed Matter **26**, 145302 (2014)*

154. Pohl, D.; Wiesenhütter, U.; Mohn, E.; Schultz, L.; Rellinghaus, B.
     Near-Surface Strain in Icosahedra of Binary Metallic Alloys: Segregational vs. Intrinsic Effects
     Nano Letters ***14****, 1776 (2014)*

155. Popov, A. A.; Kästner, Ch.; Krause, M.; Dunsch, L.
     Carbon Cage Vibrations of $M@C_{82}$ and $M_2@C_{2n}$ (M = La, Ce; 2n = 72, 78, 80): The Role of the Metal Atoms
     Fullerenes, Nanotubes, and Carbon Nanostructures ***22****, 202 (2014)*

156. Radek, M.; Bracht, H.; Posselt, M.; Liedke, B.; Schmidt, B.; Bougeard, D.
     Temperature dependence of ion-beam mixing in crystalline and amorphous germanium isotope multilayer structures
     Journal of Applied Physics ***115****, 023506 (2014)*

157. Rafaja, D.; Wüstefeld, C.; Dopita, M.; Motylenko, M.; Bähtz, C.
     Capability of X-ray diffraction for the study of microstructure of metastable thin films
     IUCrJ ***1****, 446 (2014)*

158. Rafaja, D.; Wüstefeld, C.; Dopita, M.; Motylenkoa, M.; Bähtz, C.; Michotte, C.; Kathrein, M.
     Crystallography of phase transitions in metastable titanium aluminium nitride nanocomposites
     Surface & Coatings Technology ***257****, 26 (2014)*

159. Rittweger, F.; Hinsche, N. F.; Zahn, P.; Mertig, I.
     Signature of the topological surface state in the thermoelectric properties of Bi_2Te_3
     Physical Review B ***89****, 035439 (2014)*

160. Rodrigues, D.; Korschinek, G.; Merchel, S.; Rugel, G.; Arazi, A.; Marti, G. V.
     Aplicacion de la tecnica de espectrometria de masas con aceleradores en el estudio de la dinamica de sedimentos submarinos (Application of the accelerator mass spectrometry technique to the study of the marine sediments dynamic)
     ANALES AFA (Asociación Física Argentina) ***25****, 51 (2014)*

161. Schmidt, K.; Akhmadaliev, Sh.; Anders, M.; Bemmerer, D.; Caciolli, A.; Dietz, M.; Elekes, Z.; Junghans, A. R.; Menzel, M.-L.; Schwengner, R.; Wagner, A.; Zuber, K.
     Strength of the E_p = 1.842 MeV resonance in the $^{40}Ca(p,\gamma)^{41}Sc$ reaction reexamined
     Physical Review C ***89****, 045802 (2014)*

162. Schmidt, M.; Zschornack, G.; Kentsch, U.; Ritter, E.
     Permanent magnet electron beam ion source/trap systems with bakeable magnets for improved operation conditions
     Review of Scientific Instruments ***85****, 02B704 (2014)*

163. Schwehr, K. A.; Otosaka, S.; Merchel, S.; Kaplan, D. I.; Zhang, S.; Xu, C.; Li, H.-P.; Ho, Y.-F.; Yeager, C. M.; Santschi, P. H.; Aster, T.
     Speciation of iodine isotopes inside and outside of a contaminant plume at the Savannah River Site
     Science of the Total Environment ***497–498****, 671 (2014)*

164. Sheng, Y.; Rui, W.; Qiu, X.; Du, J.; Zhou, S.; Xu, Q.
     The multiferroic properties of polycrystalline $Bi_{1-x}Y_xFeO_3$ films
     Journal of Applied Physics ***115****, 17D902 (2014)*

165. Stöcker, H.; Zschornak, M.; Richter, C.; Hanzig, J.; Hanzig, F.; Hinze, V.; Potzger, K.; Gemming, S.; Meyer, Dirk C.
     Surface-near modifications of $SrTiO_3$ local symmetry due to nitrogen implantation investigated by grazing incidence XANES
     Scripta Materialia ***86****, 1 (2014)*

166. Tan, Y.; Akhmadaliev, Sh.; Zhou, S.; Sun, S.; Chen, F.
     Guided continuous-wave and graphene-based Q-switched lasers in carbon ion irradiated Nd:YAG ceramic channel waveguide
     Optics Express ***22****, 3572 (2014)*

167. Tan, Y.; Chen, C.; Akhmadaliev, Sh.; Zhou, S.; Chen, F.
Nd:YAG waveguide laser Q-switched by evanescent-field interaction with graphene
Optics Express ***22**, 9101 (2014)*

168. Teshome, B.; Facsko, S.; Keller, A.
Topography-controlled alignment of DNA origami nanotubes on nanopatterned surfaces
Nanoscale ***6**, 1790 (2014)*

169. Tyschenko, I. E.; Voelskow, M.; Tscherkov, A. G.; Popov, V. P.
Ion-beam synthesis of InSb nanocrystals in the buried SiO2 layer of a silicon-on-insulator structure
Semiconductors ***48**, 1196 (2014)*

170. van Gastel, R.; Hlawacek, G.; Dutta, S.; Poelsema, B.
Backscattered helium spectroscopy in the helium ion microscope: Principles, resolution and applications
Nuclear Instruments and Methods in Physics Research B ***344**, 44 (2015)*

171. Virgilio, M.; Ortolani, M.; Teich, M.; Winnerl, S.; Helm, M.; Sabbagh, D.; Capellini, G.; de Seta, M.
Combined effect of electron and lattice temperatures on the long intersubband relaxation times of Ge/Si$_x$ Ge$_{1-x}$ quantum wells
Physical Review B ***89**, 045311 (2014)*

172. Weichsel, T.; Hartung, U.; Kopte, T.; Zschornack, G.; Kreller, M.; Silze, A.
An inverted cylindrical sputter magnetron as metal vapour supply for electron cyclotron resonance ion sources
Review of Scientific Instruments ***85**, 053301 (2014)*

173. Yao, Y.; Jia, Y.; Chen, F.; Akhmadaliev, Sh.; Zhou, S.
Channel waveguide lasers at 1064 nm in Nd:YAG crystal produced by C5+ ion irradiation with shadow masking
Applied Optics ***53**, 195 (2014)*

174. Zatsepin, A. F.; Fitting, H.-J.; Buntov, E. A.; Pustovarov, V. A.; Schmidt, B.
Defects and localized states in silica layers implanted with lead ions
Journal of Luminescence ***154**, 425 (2014)*

175. Zeil, K.; Metzkes, J.; Kluge, T.; Bussmann, M.; Cowan, T. E.; Kraft, S. D.; Sauerbrey, R.; Schmidt, B.; Zier, M.; Schramm, U.
Robust energy enhancement of ultrashort pulse laser accelerated protons from reduced mass targets
Plasma Physics and Controlled Fusion ***56**, 084004 (2014)*

176. Zierold, R.; Le Lam, C.; Dendooven, J.; Gooth, J.; Böhnert, T.; Sergelius, P.; Munnik, F.; Montero Moreno, J. M.; Görlitz, D.; Detavernier, C.; Nielsch, K.
Magnetic Characterization and Electrical Field-Induced Switching of Magnetite Thin Films Synthesized by Atomic Layer Deposition and Subsequent Thermal Reduction
Journal of Physics D: Applied Physics ***47**, 485001 (2014)*

177. Zschornack, G.; Ritter, E.; Schmidt, M.; Schwan, A.
Electron beam ion sources (EBIS) for use in second generation synchrotrons for medical particle therapy
Review of Scientific Instruments ***85**, 02B702 (2014)*

178. Zschornak, M.; Richter, C.; Nentwich, M.; Stöcker, H.; Gemming, S.; Meyer, D. C.
Probing a crystal's short-range structure and local orbitals by Resonant X-ray Diffraction methods
Crystal Research and Technology ***49**, 43-54 (2014)*

Patents

1. Schmidt, H.; Kaspar, T.; Bürger, D.; Skorupa, I.; Fiedler, J.
   P1313-Magnetisierbare Halbleiter und Oxide mit permanenter Magnetisierung, deren Herstellung und Verwendung
   DE102013209278.4 - Offenlegung-20.11.2014; Nachanmeldung-WO
2. Schmidt, H.; Kaspar, T.; Schmidt, O. G.; Brunner, R.
   P1309-Magnetooptik mit strukturierten unmagnetischen Metallen
   DE102013203761: Offenlegung-11.09.2014; Nachanmeldung WO
3. Schmidt, H.; Kolitsch, A.; Manjunath, N.; Ou, X.; Shuai, Y.; Skorupa, I.; You, T.; Bürger, D.; Du, N.
   P1401WO-Komplementärer Widerstandsschalter, Kontaktierte Polykristalline Piezo- oder Ferroelektrische Dünnschicht, Verfahren zum Verschlüsseln einer Bitfolge
   PCT/EP2014/050829 - Offenlegung: 14.07.2014;
4. Schmidt, H.; You, T.; Du, N.; Bürger, D.; Skorupa, I.
   P1304DE-Komplementärer Widerstandsschalter, dessen Herstellung und Verwendung
   DE102013200615 - Offenlegung: 17.07.2014
5. Bürger, D.; Skorupa, I.
   P1226DE-Funktionalisierte Festkörperoberflächen aus Zwei- und Mehrstoffsystemen mit Komposit-Nanostrukturen aus Metallen, Halbleitern und Isolatoren
   DE102012221409.7 - Offenlegung: 22.05.2014
6. Prucnal, S.; Voelskow, M.; Skorupa, W.
   P1227DE-Verfahren zur kostengünstigeren Herstellung von Silizium Solarzellen, und mit diesem Verfahren hergestellte Solarzellen
   DE102012221811 - Offenlegung: 28.05.2014
7. Kolitsch, A.; Rogozin, A.; Brinke-Seiferth, S.
   P1210-Metallmembran
   DE102012105770 - Offenlegung - 02.01.2014; Nachanmeldung: WO

Concluded scientific degrees

Habilitations

1. Erbe, A.
   Dynamics of colloidal suspension in two-dimensional geometries
   Universität Konstanz, 23.07.2014
2. Pashkin, A.
   Ultrafast probing and coherent control of low-energy excitations in condensed matter
   Universität Konstanz, 14.07.2014

PhD theses

1. Bernert, K.
   Spin-transfer torques in MgO-based magnetic tunnel junctions
   TU Dresden, 03.02.2014
2. Böttger, R.
   Self-organized nanostructures by heavy ion irradiation: defect kinetics and melt pool dynamics
   TU Chemnitz, 16.01.2014
3. Buhl, M.
   Spin transfer torque-induziertes Schalten von Nanomagneten in lateraler Geometrie bei Raumtemperatur
   TU Dresden, 07.04.2014
4. Cornelius, S.
   Charge transport limits and electrical dopant activation in transparent conductive (Al, Ga):ZnO and Nb:TiO_2 thin films prepared by reactive magnetron sputtering
   TU Dresden, 16.06.2014
5. Gao, K.
   Highly mismatched $GaAs_{1-x}N_x$ and $Ge_{1-x}Sn_x$ alloys prepared by ion implantation and ultrashort annealing
   TU Dresden, 19.12.2014
6. Kaspar, T.
   Metall-Halbleiter-Feldeffekttransistoren mit magnetischem Halbleiterkanal auf Zinkoxidbasis
   TU Dresden, 15.07.2014
7. Kunze, T.
   Atomistic simulations on the nanotribology of tetrahedral amorphous carbon films
   TU Dresden, 23.04.2014
8. Mittendorff, M.
   Carrier relaxation dynamics in graphene
   TU Dresden, 03.11.2014
9. Philipp, P.
   Phase transformation in tetrahedral amorphous carbon by focused ion beam irradiation
   TU Dresden, 12.02.2014
10. Teich, M.
    Non-linear THz spectroscopy in semiconductor quantum structures
    TU Dresden, 26.09.2014
11. Wiesenhütter, U.
    Elektrische Charakterisierung von FePt-Nanopartikeln
    TU Dresden, 02.06.2014

12. Wilhelm, R. A.
Wechselwirkung langsamer hochgeladener Ionen mit Ionenkristalloberflächen und ultradünnen Kohlenstoffmembranen
TU Dresden, 05.12.2014

13. Wintz, S.
Spin vortices in magnetic multilayers
TU Dresden, 28.03.2014

Master/Diploma theses

1. Baldauf, S.
Moleküldynamische Simulation der Rekristallisation in Germanium-Nanodrähten durch Festphasenepitaxie
TU BA Freiberg, 24.09.2104

2. Braun, M.
Elektrische und optoelektronische Eigenschaften siliziumbasierter Lichtemitter mit durch Atomlagenabscheidung hergestellten Tb2O3-SiO2 Mischschichten
Westsächsische Hochschule Zwickau, 27.03.2014

3. Bräuning, S.
Herstellung und Charakterisierung von Cr-Zr-O-Dünnschichtnanokompositen
TU BA Freiberg, 13.10.2014

4. Kusch, M.
Phasenbildung in metastabilen Al-Zr-O-Dünnschichtnanokompositen
TU BA Freiberg, 20.10.2014

5. Schiwarth, M.
Ab-initio investigation of copper-vacancy nanocluster in bcc iron
TU BA Freiberg, 22.11.2014

6. Schreiber, B.
Herstellung und Charakterisierung geordneter Au Nanopartikel, hergestellt auf gewellten Si-Oberflächen
TU Dresden, 27.10.2014

7. Xu, M.
Bandstructure modification of II-VI semiconductors oversaturated with isoelectronic impurities
KU Leuven, Belgium; TU Dresden, 24.09.2014

BSc theses

1. Hoffmann, S.
Magnetische Charakterisierung dünner Keilschichten mittels frequenzaufgelöstem magnetooptischen Kerr-Effekt
TU Ilmenau, 16.12.2014

2. Liersch, V.
Herstellung und Charakterisierung eines Spinventils zur Untersuchung der Spindiffusionslänge von FeAl
Westsächsische Hochschule Zwickau, 21.03.2014

3. Rupp, S.
Untersuchung der magnetischen Eigenschaften von Permalloy-Filmen mittels frequenzaufgelöstem magnetooptischen Kerr-Effekt (FR-MOKE)
nta Naturwissenschaftlich-Technische Akademie Prof. Dr. Grübler gGmbH, 27.02.2014

Appointments and honors

Appointments

1. **Ou, Xin**
   Scientist in the research group “Ion Induced Nanostructures“ of the Ion Beam Center has received a **professorship** within **The Hundred Talents Program** of the Chinese Academy of Sciences (CAS).

Awards and honors

1. **Bogusz, Agnieszka**
   PhD candidate in the Virtual Institute (VI) MEMRIOX and the division “Semiconductor Materials” won an **Excellent Student Paper Certificate** at the 12th International Conference on Solid - State and Integrated Circuit Technology (ICSICT), 28-31 Oct 2014, Guilin, China.
2. **Bogusz, Agnieszka**
   Agniezska Bogusz PhD candidate in the Virtual Institute (VI) MEMRIOX and the division “Semiconductor Materials” won an **Excellent Oral Presentation Certificate** at the 3rd International Conference on Material Science and Engineering Technology (ICMSET), 24-26 Oct 2014, Beijing, China.
3. **Facsko, Stefan; Heller, René; Wilhelm, Richard**
   Members of the research group “Ion Induced Nanostructures“ at the Ion Beam Center received the **HZDR Research Award 2014** for their investigations of slow highly charged ions interacting with carbon nano membranes and surfaces of ionic crystals.
4. **Gao, Kun**
   PhD candidate in the Helmholtz Young Investigator Group "Functional Materials" of the division “Semiconductor Materials” received the **Young Scientist Award**, Symp. X: Materials Research for Group IV Semiconductors: Growth, Characterization & Technological Developments, “Liquid phase epitaxy of Ge(1-x)Sn(x) alloy using ion-implantation and pulsed laser melting“ at the E-MRS 2014 Spring Meeting, 26-30 May 2014, Lille, France.
5. **Gao, Kun**
   PhD candidate in the Helmholtz Young Investigator Group "Functional Materials" of the division “Semiconductor Materials” received the **Best Poster Prize**: “$Ge_{(1-x)}Sn_x$ alloy synthesized by ion-implantation: from epitaxial thin films to crystalline nanostructures“ at the international conference "Trends in Nanotechnology 2014", 27-31 Oct 2014, Barcelona, Spain.
6. **Kolitsch, Andreas**
   Senior Scientist at the Ion Beam Center was appointed as **Guest professor** at the Faculty of materials science of the Slowak University of Technology Bratislava for a period of two years.
7. **Mittendorff, Martin**
   Scientist in the “Spectroscopy” division received a **HZDR Ph.D. Recognition Award 2014** for his thesis on “Carrier Relaxation Dynamics in Graphene”.
8. **Prucnal, Slawomir**
   PostDoc in the division “Semiconductor Materials” won the **Best Poster Prize**, Symp.Y: Advanced materials and characterization techniques for solar cells II, “OFOCell concept for low cost silicon photovoltaics“ at the E-MRS 2014 Spring Meeting, 26-30 May 2014, Lille, France.
9. **Schneider, Harald**
   Head of the “Spectroscopy” division was selected for the **Chinese National 1000 Foreign Experts Program** but declined a professorship at the Shanghai Jiao Tong University in Shanghai, China.

10. **Schultheiß, Helmut**
    PostDoc in the "Magnetism" division received funding of the **Emmy-Noether-Young-Investigator-Group** "Magnonics: Spin waves bridging Spintronics and Photonics" by the Deutsche Forschungsgemeinschaft (DFG).

11. **Schultheiß, Helmut**
    PostDoc in the "Magnetism" division was elected as **Member of the Editorial Review Board** of the journal "IEEE Magnetics Letters".

12. **Winnerl, Stephan**
    PostDoc in the "Spectroscopy" division was elected as **HZDR Research Fellow** for his outstanding internationally renowned scientific achievements in the field of terahertz and ultrafast spectroscopy.

Invited conference contributions, colloquia, lectures and talks

Invited conference talks

1. Buchriegler, J.; Munnik, F.; Hanf, D.; von Borany, J.; Nowak, S. H.; Scharf, O.; Ziegenrücker, R.; Merchel, S.; Renno, A. D.
High-Speed PIXE: Fast multi-elemental analysis with lateral resolution using a Colour X-Ray Camera
8th International Symposium on BioPIXE, 15.-19.09.2014, Bled, Slovenia
2. Buchriegler, J.; von Borany, J.; Hanf, D.; Merchel, S.; Munnik, F.; Nowak, Stanislaw H.; Renno, Axel D.; Scharf, O.; Ziegenrücker, R.
High-Speed PIXE: Fast Elemental Analysis with a Colour X-Ray Camera
14th International Conference on Nuclear Microprobe Technology and Applications, 06.-11.07.2014, Padova, Italy
3. Facsko, S.; Ou, X.
Spontaneous pattern formation in reverse epitaxy
5th International Conference on NANO-structures SElf-Assembly, 07.-11.07.2014, Marseille, France
4. Facsko, S.; Ou, X.; Helm, M.; Fassbender, J.
Faceting semiconductor surfaces by reverse epitaxy
16th International Conference on Thin Films, 13.-16.10.2014, Dubrovnik, Croatia
5. Fassbender, J.
Magnetic films tailored by ion irradiation
Physics of Surfaces and Interfaces, 24.-28.02.2014, Puri, India
6. Gago-Fernandez, R.; Redondo-Cubero, A.; Palomares, J.; Hübner, R.; Vazquez, L.
Self-organized Nanopatterns on Silicon Surfaces by Ion-Beam-Sputtering with Metal Co-deposition
2014 MRS Spring Meeting, 21.-25.04.2014, San Francisco, USA
7. Heller, R.; Wilhelm, R. A.; Gruber, E.; Ritter, R.; Stöger-Pollach, M.; Mücklich, A.; Werner, U.; Beyer, A.; Vieker, H.; Facsko, S.; Gölzhäuser, A.; Aumayr, F.
The interaction of slow highly charged ions with carbon nano membranes
20th International Workshop on Inelastic Ion-Surface Collisions (IISC-20), 16.-21.02.2014, Adelaide, Australia
8. Helm, M.; Mittendorff, M.; Winnerl, S.; Wendler, F.; Malic, E.; Knorr, A.
Population dynamics in graphene Landau levels
International Quantum Cascade Lasers School and Workshop 2014, 07.-12.09.2014, Policoro, Italy
9. Liedke, B.; Heinig, K.-H.; Böttger, R.; Anders, C.; Urbassek, H.; Facsko, S.; Posselt, M.
Atomistic modeling of ion-beam induced processes in Si and Ge
Swift Heavy ions in Materials Engineering and Characterization (SHIMEC 2014), 14.-17.10.2014, New Delhi, India
10. Möller, W.
Ion-surface interaction in plasma processing
PSE 2014 - International Conference on Plasma Surface Engineering, 15.-20.09.2014, Garmisch-Partenkirchen, Germany
11. Ou, X.; Hübner, R.; Helm, M.; Fassbender, J.; Facsko, S.
Reverse Epitaxy on Semiconductor Surfaces
The 10th international ESPS-NIS workshop, 20.-23.07.2014, Traunkirchen, Austria

12. Ou, X.; Keller, A.; Helm, M.; Fassbender, J.; Facsko, S.
Reverse epitaxy on Ge surfaces
23rd Conference on Application of Accelerators in Research and Industry, 25.-30.05.2014, San Antonio, USA

13. Prucnal, S.; Gao, K.; Skorupa, I.; Liu, F.; Skorupa, W.; Zhou, S.
Hyperdoping of semiconductors by ion implantation and ultrafast annealing: solid vs. liquid phase epitaxy
ION 2014 - X-th International Conference on Ion Implantation and Other Applications of Ions and Electrons, 23.-26.06.2014, Kazimierz Dolny, Poland

14. Rebohle, L.; Berencén, Y.; Braun, M.; Garrido, B.; Hiller, D.; Liu, B.; Ramírez, J. M.; Sun, J. M.; Wutzler, R.; Helm, M.; Skorupa, W.
Rare Earth Doped Metal-Oxide-Semiconductor Structures: A Promising Material System or a Dead End of Optoelectronic Evolution?
225th ECS Meeting, 11.-15.05.2014, Orlando, USA

15. Renno, Axel D.; Gutzmer, J.; Birtel, S.; Atanasova, P.; Bachmann, K.; Matos Camacho, S.; Schulz, B.; Kern, M.; Krause, J.; Munnik, F.
Geometallurgy of REE deposits - state of the art
Geology to Metallurgy of Critical Rare Earths, 24.-25.03.2014, Penryn, UK

16. Rugel, G.; Akhmadaliev, S.; Merchel, S.; Pavetich, S.; Renno, A. D.; Ziegenrücker, R.
Progress at DREsden AMS
DPG-Frühjahrstagung der Sektion AMOP (SAMOP), 17.-21.03.2014, Berlin, Germany

17. Schneider, H.
QWIP-Based “Ultrafast” Detectors for QCL Research
International Quantum Cascade Laser School and Workshop 2014 (IQCLSW2014), 07.-12.09.2014, Policoro, Italy

18. Schneider, H.
Coherent and nonlinear terahertz spectroscopy of low-dimensional semiconductors with a free-electron laser
7th International Symposium on Ultrafast Phenomena and Terahertz Waves (ISUPTW 2014), 13.-14.10.2014, Shanghai, China

19. Skorupa, W.
Quo vadis?: Ion Beam Engineeering and beyond…
X-th International Conference Ion Implantation and other Applications of Ions and Electrons, 23.-26.06.2014, Kazimierz Dolny, Poland

20. Vogt, K.; Fradin, F. Y.; Pearson, J. E.; Sebastian, T.; Bader, S. D.; Hillebrands, B.; Hoffmann, A.; Schultheiss, H.
Realization of a spin-wave multiplexer
59th Annual Magnetism & Magnetic Materials Conference, 03.-7.11.2014, Honolulu, USA

21. Wiesenhütter, K.; Lindberg, P.; Bregolin, F. L.; Prucnal, S.; Vines, L.; Mathey, A.; Wiesenhütter, U.; Monakhov, E. V.; Svensson, B. G.; Skorupa, W.
Advanced ms-annealing concepts for semiconducting oxides for PV applications
E-MRS Fall Meeting 2014, 15.-18.09.2014, Warszawa, Poland

22. Wilhelm, R. A.; Gruber, E.; Ritter, R.; Heller, R.; Facsko, S.; Aumayr, F.
Interaction of Slow Highly Charged Ions with Ultrathin Membranes
17th International Conference Physics of Highly Charged Ions (HCI2014), 31.08.-05.09.2014, San Carlos de Bariloche, Argentina

23. Winnerl, S.; Mittendorff, M.; Teich, M.; Jacob, R.; Schneider, H.; Helm, M.
Kurzzeit-Spektroskopie an Halbleiter-Quantenstrukturen am Freie-Elektronen-Laser FELBE
Deutsche Tagung für Forschung mit Synchrotronstrahlung, Neutronen und Ionenstrahlen an Großgeräten 2014 (SNI 2014), 21.-23.09.2014, Bonn, Germany

24. Winnerl, S.; Mittendorff, M.; Wendler, F.; Malic, E.; Knorr, A.; Schneider, H.; Helm, M.
Ultrafast spectroscopy on Landau quantized graphene: Evidence for strong Auger scattering

5th International Symposium on Terahertz Nanoscience, 01.-05.12.2014, Schoelcher, Martinique, France

25. Wintz, S.
Topology and Origin of Effective Spin Meron Pairs in Ferromagnetic Multilayer Elements
DPG-Frühjahrstagung der Sektion Kondensierte Materie, 30.03.-04.04.2014, Dresden, Germany

26. Wintz, S.; Raabe, J.; Fassbender, J.
Effective spin meron pairs in ferromagnetic multilayer elements
59th Annual Magnetism & Magnetic Materials Conference, 03.-07.11.2014, Honolulu, USA

27. Yankov, R.; Borany, J. von; Masset, P. J.; Donchev, A.; Schütze, M.
Recent developments in surface protection of titanium and titanium-aluminum alloys against environmental degradation at elevated temperatures
Shechtman International Symposium, 29.06.-04.07.2014, Cancun, Mexico

28. Zhou, S.
Ion beam synthesis of the full spectrum of III-V:Mn ferromagnetic semiconductors
E-MRS 2014 SPRING MEETING, 26.-30.05.2014, Lille, France

29. Zhou, S.
Ion beam synthesis of the full spectrum of III-V:Mn ferromagnetic semiconductors
X-th International Conference - Ion Implantation and Other Applications of Ions and Electrons, 23.-26.06.2014, Kazimierz Dolny, Poland

30. Zhou, S.
Ion beam synthesis of the full spectrum of III-V:Mn ferromagnetic semiconductors
The Moscow International Symposium on Magnetism 2014, 29.06.-03.07.2014, Moscow, Russia

Colloquia

31. Fassbender, J.
Nanomagnets - created and tailored by ions
Colloquium, Institute of Physics, 21.02.2014, Bhupaneshwar, India

32. Fassbender, J.
Nanomagnets - created and tailored by ions
Kolloquium, Universität Kiel, 27.01.2014, Kiel, Germany

33. Fassbender, J.
Nanomagnets - created and tailored by ions
Colloquium, Institute of Physics, Polish Academy of Sciences, 07.10.2014, Warschau, Poland

34. Fassbender, J.
Form follows function - neue Funktionalitäten durch Nanostrukturierung
10 Jahre Nano Structuring Centre Kaiserslautern, 08.07.2014, Kaiserslautern, Germany

35. Gensch, M.
Long waves from short bunches: Concepts and applications of super-radiant THz sources
Kolloquium der Fakultät für Physik, KIT, 31.01.2014, Karlsruhe, Germany

36. Gensch, M.
THz driven Dynamics in Matter: Sources and Applications
Kolloquium des Instituts für Analytische Wissenschaften (ISAS), 17.11.2014, Berlin, Germany

37. Hlawacek, G.
The dark side of Helium Ion Microscopy
Kolloquium, 06.06.2014, Bielefeld,Germany

38. Hlawacek, G.
5 years of Helium Ion Microscopy
Kolloquium PIN/UTwente, 17.04.2014, Enschede, Netherlands

39. Hübner, R.
Transmission Electron Microscopy at the Helmholtz-Zentrum Dresden-Rossendorf (HZDR)
Kolloquium des Instituts für Strukturphysik der TU Dresden, 28.01.2014, Dresden, Germany

Lectures and talks

40. Bali, R.; Wintz, S.; Meutzner, F.; Huebner, R.; Boucher, R.; Uenal, A. A.; Valencia, S.; Neudert, A.; Potzger, K.; Bauch, J.; Kronast, F.; Facsko, S.; Lindner, J.; Fassbender, J.
    Printing Nearly-Discrete Magnetic Patterns using Chemical Disorder Induced Ferromagnetism
    Sixth Joint BER II and BESSY II User Meeting, 03.-05.12.2014, Berlin, Germany

41. Buchriegler, J.; von Borany, J.; Hanf, D.; Munnik, F.; Nowak, Stansilaw H.; Renno, Axel D.; Scharf, O.; Ziegenrücker, R.
    High-Speed PIXE: A spatially resolved PIXE setup at the 6 MV Tandem accelerator
    SLcam$^{(R)}$ User Workshop, 16.01.2014, Berlin, Germany

42. Cornelius, S.
    Dopant activation and charge transport limits in transparent conductive (Al,Ga):ZnO and Nb:TiO2
    Institutsseminar, Institut für experimentelle Physik II, Universität Leipzig, 26.11.2014, Leipzig, Germany

43. Devaraj, M.
    Properties of oxide nanoclusters in ODS ferritic steels: A combined DFT and Monte Carlo simulation study
    Seminar talk Department of Mathematical Sciences, Loughborough University, 02.10.2014, Loughborough, UK

44. Erbe, A.
    Transport in mesoscopic conductors
    PIER summer school, 06.-09.10.2014, Hamburg, Germany

45. Erbe, A.
    Introduction to transport in confined geometries and across point contacts
    MAINZ summer school, 25.-29.08.2014, Mainz, Germany

46. Erbe, A.; Gemming, S.
    Nanoscale Transport Phenomena
    Abengoa Research Seminar, 20.05.2014, Sevilla, Spain

47. Facsko, S.
    Vacancy controlled spontaneous pattern formation on semiconductor surfaces
    Seminar, 12.11.2014, Stuttgart, Germany

48. Facsko, S.
    Low energy ion irradiations in material research
    Seminar, 20.06.2014, Cork, Ireland

49. Facsko, S.; Wilhelm, R. A.; Gruber, E.; Heller, R.; Aumayr, F.
    Energy Loss and Charge Exchange of Highly Charged Ions in Carbon Nanomembranes
    Seminar an der Fakultät für Physik der Universität Bielefeld, 06.06.2014, Bielefeld, Germany

50. Gemming, S.
    Kleinste Strukturen ganz groß – Forschung mit Großgeräten
    Seniorenkolleg der TU Chemnitz, 27.05.2014, Chemnitz, Germany

51. Gensch, M.
    High field THz sources operating at 100 kHz Repetition rates: Challenges and Opportunities
    Seminar of the Stanford Institute for Materials and Energy Sciences, 12.09.2014, Stanford / SLAC, USA

52. Grebing, J.; Deb, D.; Grube, M.; Trommer, J.; Teshome, B.; Sendler, T.; Wieser, M.; Helm, M.; Weber, W.; Keller, A.; Erbe, A.
    Transport in Nanoelectronic Systems
    9th Silicon Saxony Day, 03.07.2014, Dresden, Germany

53. Grenzer, J.
X-ray Diffraction and Scattering from Nanostructures
Workshop on X-ray Scattering Methods for Thin Film Characterization, 25.-26.09.2014, Prague, Czech Republic

54. Grenzer, J.
In-situ X-ray experiments for material science
Workshop „Advanced X-ray Diffraction for Semiconductor Materials and Technology“, 03.-04.04.2014, Frankfurt/Oder, Germany

55. Günther, F.; Gemming, S.; Seifert, G.
Calculation of Electronic Structure and Transport properties of Donor – Acceptor Polymers
Seminar der Professur Theorie ungeordneter Systeme TU Chemnitz, 17.12.2014, Chemnitz, Germany

56. Günther, F.; Gemming, S.; Seifert, G.
Calculation of Electronic Structure and Transport properties of Donor – Acceptor Polymers
Arbeitsgruppenseminar der Professur für Theoretische Chemie TU Dresden, 20.11.2014, Dresden, Germany

57. Helm, M.
THz spectroscopy of solids using a free-electron laser
Seminarvortrag am Fritz-Haber-Institut (FHI) Berlin, 20.10.2014, Berlin, Germany

58. Helm, M.
Terahertz spectroscopy of nanostructures with a free electron laser
Annual BuildMoNa Conference, 04.03.2014, Leipzig, Germany

59. Hlawacek, G.
The He ion microscope - a high resolution tool for the nano–world
ANP retreat, 19.-20.06.2014, Tecklenburg, Germany

60. Hlawacek, G.; Veligura, V.; Bali, R.; van Gastel, R.; Poelsema, B.; Facsko, S.
Helium Ion Microscopy: A high resolution tool for the nano-world
Workshop Ionenstrahlen & Nanostrukturen, 20.-22.07.2014, Paderborn, Germany

61. Krause, M.
The Ion Beam Center at the HZDR, nanocomposite growth with ions, and cluster tool setting up
Seminar at Abengoa Research, 12.02.2014, Seville, Spain

62. Langer, M.; Gallardo, R.; Banholzer, A.; Schneider, T.; Wagner, K.; Landeros, P.; Lenz, K.; Lindner, J.; Fassbender, J.
Evolution of Spin Wave Modes in Periodically Perturbed Thin Films
Gruppenseminar der AG Küpper an der TU Osnabrück, 10.-11.12.2014, Osnabrück, Germany

63. Liedke, B.
Power of the sun is all we need for a power plant
Science slam in Köln, 07.11.2014, Köln, Germany

64. Liedke, B.; Heinig, K.-H.; Friedrich, D.; Schmidt, B.; Mücklich, A.; Keles, U.; Bulutay, C.
Sponge-like Si-SiO_2 nanocomposite for PV applications
Seminar an der TU Bergakademie Freiberg, 15.07.2014, Freiberg, Germany

65. Liedke, B.; Heinig, K.-H.; Schmidt, B.; Bulutay, C.; Böttger, R.; Posselt, M.; Bracht, H.
Atomistic modeling of ion-beam and thermally induced processes in Si and Ge
Seminar at the KTH Royal Institute of Technology - Reactor Physics, 12.11.2014, Stockholm, Sweden

66. Mittendorff, M.
Kurzzeitspektroskopie: Kürzeste Laserpulse für Materialuntersuchungen
2. Fortbildungsveranstaltung zu Optotechnik und Bildverarbeitung, 27.06.2014, Darmstadt, Germany

67. Pelic, B.; Skorupa, W.
Plasma-based nanotechnology against corrosion of organ pipes
Final conference of the EU research project "EU-PANNA", 04.09.2014, Berlin, Germany

68. Schmidt, H.; Wiesenhütter, K.; Teichmann, D.
PolCarr - Smarte Trägermaterialien für die Biotechnologie
Cross Cluster Cooperation-Projekt „C3-Saxony“, IDEA CALL zum 9. Silicon Saxony Day, 03.07.2014, Dresden, Germany

69. Schneider, H.
High-performance QWIPs and time-resolved terahertz spectroscopy with a free-electron laser
Seminar, Kunming Institute of Physics, 17.10.2014, Kunming, China

70. Schneider, H.
Quantum structure THz photonics and spectroscopy at HZDR
Seminarvortrag, Centre Suisse d'Electronique et Microtechnique SA (CSEM), 19.09.2014, Neuchâtel, Switzerland

71. Schneider, T.; Hübner, R.; Lenz, K.; Lindner, J.; Fassbender, J.
Investigation of interlayer exchange coupling and magnetic anisotropy of Fe3Si-trilayers using ferromagnetic resonance
Gruppenseminar AG Wende, 14.01.2014, Duisburg, Germany

72. Wiesenhütter, K.; Urban, B.; Müller, M.; Müller, A.-D.; Skorupa, I.; Rüb, M.; Skorupa, W.; Schmidt, O. G.; Schmidt, H.
PolCarr: Smart carriers for advanced manufacturing in biotechnology
Bionection Partnering Conference for Technology Transfer in Life Sciences, 09.-10.10.2014, Dresden, Germany

73. Wiesenhütter, K.; Urban, B.; Müller, M.; Müller, A.-D.; Skorupa, I.; Rüb, M.; Skorupa, W.; Schmidt, O. G.; Schmidt, H.
PolCarr® - Smart carriers for advanced manufacturing in biotechnology
Innovation Days 2014 München: Research Meets Business, 01.-02.12.2014, München, Germany

Conferences, workshops, colloquia and seminars

Organization of conferences and workshops

1. Altstadt, E.; Colomer, M.
   LONGLIFE Final Workshop
   15. - 16.01.2014, Dresden, Germany
2. Bergner, F.; Heintze, C.; Hilger, I.; Posselt, M.
   2nd International Workshop on ODS Materials
   26. - 27.06.2014, Dresden, Germany
3. Blom, P.; Kläui, M.; Erbe, A.
   Summer School: Charge and Spin Transport in Non-Metallic Systems and Confined Geometries
   24. - 29.08.2014, Mainz, Germany
4. Erbe, A.; Zahn, P.
   IHRS NanoNet Annual Workshop 2014
   29. - 30.09.2014, Lohmen, Germany

Colloquia

1. Berger, Andreas
   CIC nanoGUNE Consolider, Donostia, Spain
   Focused Electron Beam Induced Deposition (FEBID) fabrication of nano-magnets and their magneto-optical characterization
   11.07.2014
2. Celinski, Zbigniew
   University of Colorado, Physics Department, Colorado Springs
   On-wafer microwave materials and devices
   23.01.2014
3. Celler, George
   Rutgers University, Piscataway, NJ, USA
   Laser annealing of semiconductors, what we learned 35 years ago, and why it still matters today
   27.06.2014
4. Coker, Jonathan
   HGST, a Western Digital Company, San Jose, CA, USA
   Opportunities and challenges in two dimensional magnetic recording
   09.04.2014
5. Feng, Xinliang
   TU Dresden, Department of Chemistry and Food Chemistry
   A milestone of Graphene Chemistry: From controlled synthesis to electronics and energy technologies
   20.11.2014
6. Hjörvarsson, Björgvin
   Uppsala University, Department of Physics and Astronomy, Sweden
   Demystifying nano - The influence of confinement and strain on hydrogen uptake
   22.05.2014
7. Kent, Andrew
   New York University, Department of Physics, NY, USA
   Current-induced torques in magnetic materials
   09.05.2014

8. Kläui, Mathias
   Johannes-Gutenberg-Universität Mainz, Institut für Physik
   Ultra-fast domain wall dynamics
   05.06.2014
9. Leyens, Christoph
   TU Dresden/Institut für Werkstoffwissenschaft und Fraunhofer IWS/Abteilung Thermisches Beschichten und Generieren
   Entwicklungen von Schutzschichten und Reparaturverfahren für Luftfahrtbauteile
   30.04.2014
10. Mayr, Stefan G.
    IOM Leipzig
    Ferromagnetic shape memory alloys: From ion beam assisted synthesis to plasma-assisted functionalization for biomedical applications
    23.10.2014
11. Riel, Heike
    IBM Research Zürich, Switzerland
    Semiconducting nanowires – From materials to devices
    27.03.2014
12. Sawicki, Maciek
    Institute of Physics, Polish Academy of Science, Warsaw, Poland
    The Origin of Ferromagnetism and Critical Behavior in Insulating (Ga,Mn)N
    18.11.2014

Seminars

1. Bakaev, Alexander
   SCK-CEN, Nuclear Materials Science Institute, Mol, Belgium
   Segregation-induced embrittlement in RPV steels; assessment by atomistic simulations
   14.08.2014
2. Bedanta, Subhankar
   School of Physics, National Institute of Science Education and Research (NISER), IOP Campus, Bhubaneswar, India
   Supermagnetism - State-of-art and challenges ahead
   17.02.2014
3. Boucher, Richard
   Leibniz-Institut für Festkörper- und Werkstoffforschung Dresden
   Influence of a Plasma Surface Treatment on the Electrical Properties of Bulk PZT
   31.01.2014
4. Bourlès, Didier L.
   CEREGE, CNRS, Aix-en-Provence, France
   Dating fossiliferous deposits and archaeological sites: a new accelerator mass spectrometry perspective
   08.12.2014
5. Braun, Johannes
   Universität Konstanz
   High-power Thulium-doped fiber amplifier
   06.05.2014
6. Celler, George
   Rutgers University, Piscataway, NJ, USA
   Properties of H+ implanted 4H-SiC as related to exfoliation of thin crystalline films
   27.06.2014

7. Chernykh, Pavel
Division of the atomic nuclear physics (DANP), Lomonosov Moscow State University, Skobeltsyn Institute of Nuclear Physics (MSU SINP), Russia
Ion-beam techniques for research and modification on coatings
07.01.2014

8. Dev, Bhupendra
Indian Association for the Cultivation of Science, Kolkota, India
Epitaxial nanostructures on surfaces: The role of surface symmetry and nanodot to nanowire shape transition
07.07.2014

9. Ebke, Daniel
Max-Planck-Institute for Chemical Physics of the Solids, Dresden
New Heusler compounds for spintronic applications
30.01.2014

10. Ehrler, Jonathan
TU Dresden
Improved crack propagation analysis with increased spatial resolution in the structure of microprocessors
19.09.2014

11. Engler, Martin
Institute of Physics II, University of Cologne
Self-organized ion induced pattern formation on Si(001)
24.11.2014

12. Forstner, Oliver
VERA Laboratory, Faculty of Physics, University of Vienna, Austria
Laser-Photodetachment of negative ions: Possible solution to the isobar problem in AMS?
07.04.2014

13. Fuchs, Florian
TU Chemnitz
Simulating electronic transport through carbon nanotubes and related nanostructures
15.10.2014

14. Galindo, Ramón Escobar
Abengoa Research, Sevilla, Spain
Absorber Layers for concentrated Solar Power
23.09.2014

15. Gonzalez-Elipe, Augustín R.
Materials Science Institute of Seville, Spain
Enhanced porosity in oxide thin films and nanostructures prepared by vacuum and plasma procedures: synthesis, modeling and applications
28.04.2014

16. Güttler, Dominik
ETH Zürich, Switzerland
Super-SIMS and C-14 AMS in Zurich: Challenges and applications
18.12.2014

17. Hoekstra, Ronnie
University of Groningen, The Netherlands
Unravelling the Different Potential Energy Contributions to the Secondary Electron Yields of Highly Charged Ar and Xe Ions Impacting on HOPG
21.10.2014

18. Jamshidi, Kambiz
TU Dresden, Faculty of Electrical and Computer Engineering, Communications Lab
Integrated photonic devices for communications and signal processing
29.10.2014

19. Josten, Elisabeth
FZ Jülich
Long range order in 3D nanoparticle assemblies
12.09.2014

20. Keleş, Ümit
Bilkent University, Ankara, Turkey
Silicon Nanowire-based Complex Structures: a large-scale atomistic electronic structure and ballistic transport
04.11.2014

21. Knyazev, Boris
Budker Institute of Nuclear Physics SB RAS and Novosibirsk State University, Novosibirsk, Russia
Ten years of operation of Novosibirsk free electron laser: status of the facility and recent experimental results
28.11.2014

22. König, Dirk
Theory and Characterization Group, 3rd Generation Dept., Australian Centre for Advanced Photovoltaics, Sydney, Australia
Alternatives to Conventional Doping for p and n Type Silicon Nanocrystals
18.07.2014

23. Marganiec, Justyna
GSI Darmstadt
Coulomb dissociation of Ne-17
18.12.2014

24. Migunov, Vadim
Ernst-Ruska-Zentrum Jülich
Studies of electronic and magnetic properties of nanoscaled objects by combination of electron holography and probe microcopy in TEM
13.06.2014

25. Murdin, Ben M.
University of Surrey, Guildford, UK
Physics of high field magnetic white dwarf stars – relevance to silicon quantum information applications?
24.06.2014

26. Narkowicz, Ryszard
TU Dortmund, Department of Physics
Planar microresonators for ferromagnetic resonance measurements of micro- and nanostructures
13.02.2014

27. Nazarov, Alexei
Institute of Semiconductor Physics NASU, Kyiv, Ukraine
Nanowire junctionless SOI transistors: Operation features and electrical characterization
13.06.2014

28. Ney, Andreas
Abteilung für Festkörperphysik/Johannes Kepler Universität Linz, Austria
Towards x-ray detected ferromagnetic resonance with broad-band microwave excitation and spatial resolution
21.11.2014

29. Norris, Scott
SMU Dallas, TX, USA
Irradiation-induced morphology evolution: In search of a predictive mathematical model
23.06.2014

30. Olsson, Pär
KTH Stockholm, Sweden
A study of gamma radiation damage in spent fuel canisters
27.08.2014

31. Pasquale, Massimo
    Istituto Nazionale di Ricerca Metrologica (INRIM), Torino, Italy
    Microwave properties and damping in [Pt/Co] multilayers with perpendicular anisotropy
    15.01.2014
32. Polushkin, Nikolay
    University of Lisbon, Institute of Materials and Surfaces Science and Engineering, Portugal
    Formation Mechanisms and Properties of Directly Laser Patterned Magnetic Media
    09.12.2014
33. Rodriguez, Raul
    TU Chemnitz
    Surface enhanced Raman spectroscopy
    28.04.2014
34. Spemann, Daniel
    Universität Leipzig
    Applications of ion beam modification and analysis in materials science
    29.01.2014
35. Sukhostavets, Oksana
    CIC nanoGUNE Consolider, Donostia, Spain
    Low frequency dynamics of magnetic vortices
    17.03.2014
36. Teichert, Christian
    Institute of Physics, Montanuniversität Leoben, Austria
    Graphene and ion-bombarded, rippled substrates as templates for organic thin film growth
    29.07.2014
37. Wallner, Anton
    Australian National University, Canberra, Australia
    Atom counting of actinides: nuclear (astro-)physics and environment
    16.10.2014
38. Wiedwald, Ulf
    Universität Duisburg-Essen
    Magnetic Antidot Films: From Spin-Ice to Spin-Waveguides
    30.10.2014
39. Williams, James S.
    The Australian National University, Canberra, Australia
    Supersaturation of implanted gold in silicon by pulsed laser melting and rapid thermal annealing for enhanced infrared photoresponse at room temperature
    25.09.2014
40. Zabka, Wolf-Dietrich
    Humboldt-Universität Berlin
    Adsorption of water at the (001) surface of Ga-rich Gallium phosphide
    10.03.2014

Exchange of researchers

FEL visitors

1. Ahmad, Z.
   Johann-Wolfgang-Goethe-Universität Frankfurt, Frankfurt/Main, Germany; 03.-10.03.2014
2. Awari, N.
   Zernike Institute for Advanced Materials, University of Groningen, The Netherlands; 08.-16.09.2014
3. Aydinli, A.
   Bilkent University, *Ankara, Turkey; 02.-10.03.2014*
4. Bauer, M.
   Johann-Wolfgang-Goethe-Universität Frankfurt, Frankfurt/Main, Germany; 03.-10.03.2014
5. Bordacs, S.
   Budapest University of Technology and Economics, Budapest, Hungary; 02.-08.11.2014
6. Bühler, J.
   Universität Konstanz, FB Physik - LS Leitenstorfer, Konstanz, Germany; 19.10.-24.10.2014
7. Deßmann, N.
   Aerospace Center DLR, Berlin, Germany; 03.-06.11.2014
8. *Di Pietro, P.*
   Elettra-Sincrotrone Trieste S.C.p.A. and INSTM-UdR Trieste, Basovizza, Trieste, Italy; 09.-12.04.2014; 27.05.-02.06.2014
9. Elagoz, S.
   Cumhuriyet University, *Sivas, Turkey; 02.-10.03.2014; 06.-10.07.2014*
10. Grundmann, H.
    Universität Zürich, *Physik-Institut, Zürich, Switzerland; 17.03-21.03.2014; 18.08.-21.08.2014; 25.08.-28.08.2014*
11. Lisauskas, A.
    Johann-Wolfgang-Goethe-Universität Frankfurt, Frankfurt/Main, Germany; 03.-10.03.2014
12. Orlita, M.
    Grenoble High Magnetic Field Laboratory (GHMFL), Grenoble, France; 05.02.-10.02.2014;
13. *Ortolani, M.*
    Sapienza Università di Roma, Department of Physics, Rome, Italy; 17.11.-24.11.2014
14. Pavlov, S.
    Aerospace Center DLR, Berlin, Germany; 03.-06.11.2014
15. *Perucchi, A.*
    Elettra-Sincrotrone Trieste S.C.p.A. and INSTM-UdR Trieste, Basovizza, Trieste, Italy; 09.-12.04.2014; 27.05.-02.06.2014
16. Penirschke, A.
    Technische Universität Darmstadt, Department of Electrical Engineering and Information Technology, Darmstadt, Germany; 13.04-14.04.2014
17. Pietka, B.
    University of Warsaw, Faculty of Physics, Warsaw, Poland; 12.03.-24.03.2014; 19.10.-27.10.2014
18. Pohl, A.
    Aerospace Center DLR, Berlin, Germany; 03.-06.11.2014

19. Preu, S.
Technische Universität Darmstadt, Department of Electrical Engineering and Information Technology, Darmstadt, Germany; 13.04-14.04.2014
20. *Sabbagh, D.*
Roma TRE University, Rome, Italy; 17.11.-24.11.2014
21. Sari, H.
Cumhuriyet University, Sivas, Turkey; 02.03.-10.03.2014, 06.07.-10.07.2014
22. Schmid, M.
Universität Augsburg, Institut für Physik, Augsburg, Germany; 03.11.-08.11.2014
23. Schmidt, Ch.
Universität Konstanz, FB Physik - LS Leitenstorfer, Konstanz, Germany; 19.10.-24.10.2014
24. Seletskiy, D.
Universität Konstanz, FB Physik - LS Leitenstorfer, Konstanz, Germany; 19.10.-24.10.2014
25. Szczytko, J.
University of Warsaw, Faculty of Physics, Warsaw, Poland; 12.03.-24.03.2014; 19.10.-27.10.2014
26. Tobey, R.
Zernike Institute for Advanced Materials, University of Groningen, The Netherlands; 08.09.-16.09.2014
27. *Virgilio, M.*
Università di Pisa, Department of Physics, Pisa, Italy; 17.11.-24.11.2014
28. de Vries, E.
Zernike Institute for Advanced Materials, University of Groningen, The Netherlands; 08.09.-16.09.2014
29. Wall, S.
ICFO - Institut de Ciències Fotòniques, Castelldefels, Spain; 23.09.-25.09.2014
30. Zdanevicius, J.
Johann-Wolfgang-Goethe-Universität Frankfurt, Frankfurt/Main, Germany; 03.-10.03.2014

ROBL-MRH visitors

1. Augustyns, V.
Katholieke Universiteit Leuven, Instituut voor Kern- en Stralingsfysica, Leuven, Belgium; 11.4.-15.4.2014
2. Becker, P.
Bergische Universität Wuppertal, Fachbereich Physik , Wuppertal, Germany; 7.5.-13.5.2014
3. Binzen, J.
TU Clausthal, Institut f. Metallurgie, Thermochemie & Mikrokinetik, Clausthal-Zellerfeld, Germany; 16.7.-22.7.2014
4. Biserka, G.
Rudjer Boskovic Institute, Division of Materials Physics, Zagreb, Croatia; 7.5.-10.5.2014
5. Bisht, M.
Katholieke Universiteit Leuven, IKS, Leuven, Belgium; 5.9.-9.9.2014
6. Bongers, M. D.
Georg-August-Universität Göttingen, Institut für Materialphysik, Göttingen, Germany; 15.5.-19.5.2014
7. Braeuninger-Weimer, P.
University of Cambridge, Department of Engineering, Cambridge, United Kingdom; 29.10.-4.11.2014

8. Braz Fernandes, F. M.
New University of Lisbon, CENIMAT - Materials Science Dept, Caparica, Portugal; 6.2.-11.2.2014

9. Buljan, M.
Ruder Boskovic Institute, Zagreb, Croatia; 25.6.-1.7.2014

10. Burlaka, V.
Georg-August-Universität Göttingen, Institut für Materialphysik, Göttingen, Germany; 15.5.-19.5.2014

11. Cabrero-Vilatela, A.
University of Cambridge, Centre for Advanced Photonics & Electronics, Cambridge, United Kingdom; 29.10.-4.11.2014

12. Caneva, S.
University of Cambridge, Department of Engineering, Cambridge, United Kingdom; 29.10.-4.11.2014

13. Cavaleiro, A.
University of Coimbra, CEMUC, Department of Mechanical Engineering, Coimbra, Portugal; 6.2.-11.2.2014

14. Chen, H.-Y.
Georg-August-Universität Göttingen, Institut für Röntgenphysik, Göttingen, Germany; 5.11.-11.11.2014

15. Coulet, M.-V.
CNRS UMR 7246 - Aix Marseille Université, Laboratoire MADIREL, Marseille, France; 2.4.-8.4.2014

16. da Costa Pereira, L. M.
Katholieke Universiteit Leuven, IKS, Leuven, Belgium; 11.4.-15.4.2014

17. de Jong, F.
Hamburg University of Technology, Institute of Multiphase Flows, Hamburg, Germany; 3.9.-5.9.2014, 1.12.-3.12.2014

18. de Sousa Ferreira, F.
University of Coimbra, CEMUC, Department of Mechanical Engineering, Coimbra, Portugal; 10.9.-15.9.2014

19. Deutges, M.
Georg-August-Universität Göttingen, Institut für Materialphysik, Göttingen, Germany; 15.5.-19.5.2014

20. Dopita, M.
TU Bergakademie Freiberg, Institute of Materials Science, Freiberg, Germany; 5.3.-11.3.2014

21. Etzelstorfer, T.
Johannes Kepler University, Institute of Semiconductor Physics, Linz, Austria; 19.11.-25.11.2014

22. Gruber, W.
TU Clausthal, Institute of Metallurgy, Clausthal-Zellerfeld, Germany; 16.7.-22.7.2014

23. Hamm, M.
Georg-August-Universität Göttingen, Institut für Materialphysik, Göttingen, Germany; 15.5.-19.5.2014

24. Hanzig, F.
TU Bergakademie Freiberg, Institute of Materials Science, Freiberg, Germany; 5.3.-11.3.2014

25. Hauge, H. I.
Eindhoven University of Technology, Department of Physics, Eindhoven, Netherlands; 19.11.-25.11.2014

26. Hoffmann, S.
Georg-August-Universität Göttingen, Institut für Röntgenphysik, Göttingen, Germany; 5.11.-11.11.2014

27. Kriegner, D.
Charles University, Faculty of Mathematics & Physics, Praha, Czech Republic; 19.11.-25.11.2014

28. Lazenka, V.
Katholieke Universiteit Leuven, IKS, Leuven, Belgium; 11.4.-15.4.2014, 5.9.-9.9.2014

29. Luetzenkirchen-Hecht, D.
Bergische Universität Wuppertal, Fachbereich Physik, Wuppertal, Germany; 7.5.-13.5.2014

30. Maksimova, K.
Immanuel Kant Baltic Federal University, Functional Nanomaterials, Kaliningrad, Russia; 23.4.-29.4.2014

31. Mehner, E.
TU Bergakademie Freiberg, Institute of Experimental Physics, Freiberg, Germany; 11.12.-17.12.2014

32. Menendez Dalmau, E.
Katholieke Universiteit Leuven, Instituut voor Kern- en Stralingsfysica, Leuven, Belgium; 5.9.-9.9.2014

33. Moeller, C.-O.
Hamburg University of Technology, Institute of Multiphase Flows, Hamburg, Germany; 1.12.-3.12.2014

34. Muller, C.
CNRS UMR 6242 - IM2NP, Ecole Polytechnique Universitaire Marseille, Marseille, France; 2.4.-8.4.2014

35. Nekic, N.
University of Zagreb, Semiconductors Laboratory, Zagreb, Croatia; 25.6.-1.7.2014

36. Nentwich, M.
TU Bergakademie Freiberg, Institute of Experimental Physics, Freiberg, Germany; 23.4.-29.4.2014, 11.12.-17.12.2014

37. Novikov, D. V.
DESY, Department of Photon Science, Hamburg, Germany; 23.4.-29.4.2014, 11.12.-17.12.2014

38. Oliveira, J.
University of Coimbra, CEMUC, Department of Mechanical Engineering, Coimbra, Portugal; 10.9.-15.9.2014

39. Osterhoff, M.
Georg-August-Universität Göttingen, Institut für Röntgenphysik, Göttingen, Germany; 5.11.-11.11.2014

40. Putero, M.
CNRS UMR 6242, IM2NP, Marseille, France; 2.4.-8.4.2014

41. Ramos, A. S.
University of Coimbra, CEMUC, Department of Mechanical Engineering, Coimbra, Portugal; 6.2.-11.2.2014

42. Richter, C.
TU Bergakademie Freiberg, Institute of Experimental Physics, Freiberg, Germany; 23.4.-29.4.2014, 11.12.-17.12.2014

43. Rodrigues, J.
University of Coimbra, CEMUC, Department of Mechanical Engineering, Coimbra, Portugal; 10.9.-15.9.2014

44. Salditt, T.
Georg-August-Universität Göttingen, Institut für Röntgenphysik, Göttingen, Germany; 5.11.-11.11.2014

45. Schlüter, M.
Hamburg University of Technology, Institute of Multiphase Flows, Hamburg, Germany; 1.12.-3.12.2014

46. Stangl, J.
    Johannes Kepler Universität Linz, Institut für Halbleiterphysik, Linz, Austria; 19.11.-25.11.2014
47. Teichmann, N.
    Georg-August-Universität Göttingen, Institut für Materialphysik, Göttingen, Germany; 15.5.-19.5.2014
48. van Stiphout, K.
    Katholieke Universiteit Leuven, IKS, Leuven, Belgium; 11.4.-15.4.2014
49. von Polheim, O.
    Bergische Universität Wuppertal, Department of Physics, Wuppertal, Germany; 7.5.-13.5.2014
50. Weatherup, R.
    University of Cambridge, Department of Engineering, Cambridge, United Kingdom; 29.10.-4.11.2014
51. Wüstefeld, C.
    TU Bergakademie Freiberg, Institute of Materials Science, Freiberg, Germany; 5.3.-11.3.2014
52. Wulff, D.
    Institut für Werkstoffkunde, Produktionstechnisches Zentrum, Garbsen, Germany; 10.5.-13.5.2014
53. Zhong, Q.
    Courant Research Centre Physics, Institute for X-Ray Physics, Göttingen, Germany; 5.11.-11.11.2014

Other guests

1. Ayache, R.
   University of Batna, Batna, Algeria; 14.10.-10.11.2014
2. Bedanta, S.
   National Institute of Science Education and Research, Bhubaneswar, India; 12.-24.05.2014
3. Bhattacharyya, P.
   Cornell University, Ithaca, USA; 09.06.-17.08.2014
4. Buljan, M.
   Ruder Boskovich Institute, Zagreb, Croatia; 07.-12.12.2014
5. Cai, H.
   Fudan University, China; 08.10.-31.12.2014
6. Dev, B.
   Indian Association for the Cultivation of Science, Kolkata, India; 03.-09.07.2014
7. El-Said, A.S.
   Mansoura University, Mansoura, Egypt; 30.05.-30.07.2014
8. Gritsenko, Y.
   Lomonosov Moscow State University, Moscow, Russia; 18.-24.10.2014
9. Jakubowski, M.
   Institute of Physics, Warsaw, Poland; 01.-30.09.2014
10. Keles, U.
    Bilkent University, Ankara, Turkey; 29.10.-06.11.2014
11. Khaibullin, R.
    Lomonosov Moscow State University, Moscow, Russia; 18.-23.10.2014
12. Larkin, G.
    Dublin Institute of Technology, Dublin, Ireland; 01.02.-31.08.2014
13. McKinnon, T.
    Simon Fraser University, Burnaby, Canada; 15.04.-03.07.2014

14. Monika, M.
    Simon Fraser University, Burnaby, Canada; 28.04.-31.08.2014
15. Marynowska, A.
    Institute of Physics, Warsaw, Poland; 01.-30.09.2014
16. Mathey, A.
    University Poitiers, Poitiers, France; 10.03.-29.08.2014
17. Nazarov, O.
    Institute of Semiconductor Physics, Kiew, Ukraine; 08.-14.06.2014
18. Norris, S.
    Southern Methodist University, Dallas, USA; 18.-26.06.2014
19. Olsson, P.
    KTH Royal Institute of Technology, Stockholm, Sweden; 25.-30.08.2014
20. Özey, N.
    Besevler, Turkey; 16.07.-12.09.2014
21. Rajagopal, A.
    NIT Tiruchirappalli, India; 13.05.-16.07.2014
22. Rhie, K.
    Korea University, Sejong, Korea; 18.08.-15.09.2014
23. Semisalova, A.
    Lomonosov Moscow State University, Moscow, Russia; 14.07.-13.09.2014
24. Smekhova, A.
    Lomonosov Moscow State University, Moscow, Russia; 18.-23.10.2014
25. Smith, R.
    Loughborough University, Loughborough, United Kingdom; 23.-28.06.2014
26. Tiagulsky, S.
    Institute of Semiconductor Physics, Kiew, Ukraine; 01.10.-14.12.2014
27. Wu, C.
    University of Electronic Science and Technology, Chengdu, China; 01.04.-31.12.2014
28. Xu, M.
    Xi’an University of Technology, Shaanxi, China; 27.06.-23.08.2014
29. You, T.
    TU Chemnitz, Chemnitz, Germany; 17.-21.02.; 28.03.-17.04.; 09.-20.06.; 25.08.-05.09.; 24.11.-06.12.2014
30. Yuan, X.
    TU Chemnitz, Chemnitz, Germany; 13.-18.01.2014

Projects

The projects are listed by funding institution and project starting date. In addition, the institute has several bilateral service collaborations with industrial partners and research institutions. These activities are not included in the following overview.

European Projects

1. 02/2010 – 01/2014 European Union EU
   LONGLIFE – Long term irradiation embrittlement effects
   Dr. E. Altstadt Phone: 0351 260 2276 e.altstadt@hzdr.de
2. 01/2011 – 12/2014 European Union EU
   MATTER – Materials testing and rules
   Dr. F. Bergner Phone: 0351 260 3186 f.bergner@hzdr.de
3. 06/2012 – 05/2015 European Union EU
   CALIPSO – Coordinated access to light sources
   Prof. M. Helm Phone: 0351 260 2260 m.helm@hzdr.de
4. 01/2013 – 12/2016 European Union EU
   SPRITE – Supporting postgraduate research
   Dr. J. v. Borany Phone: 0351 260 3378 j.v.borany@hzdr.de
5. 11/2013 – 10/2017 European Union EU
   MatISSE – Materials' Innovations for a Safe and Sustainable nuclear in Europe
   Dr. E. Altstadt Phone: 0351 260 2276 e.altstadt@hzdr.de

Helmholtz Association Projects

1. 03/2011 – 02/2016 Helmholtz–Gemeinschaft HGF
   Functional Materials – Helmholtz Young Investigators' Group
   Dr. Shengqiang Zhou Phone: 0351 260 2484 s.zhou@hzdr.de
2. 07/2011 – 09/2018 Helmholtz–Gemeinschaft HGF
   NANONET – Helmholtz research school on nanoelectronics
   Dr. A. Erbe Phone: 0351 260 2366 a.erbe@hzdr.de
3. 10/2011 – 09/2016 Helmholtz–Gemeinschaft HGF
   MEMRIOX – Virtual Institute – Memory effects in oxides
   Dr. P. Zahn Phone: 0351 260 3121 p.zahn@hzdr.de
4. 02/2012 – 01/2015 Helmholtz–Gemeinschaft HGF
   HRJRG–DETI.2 – Helmholtz Russia joint research group – Magnetic TiO_2
   Dr. K. Potzger Phone: 0351 260 3244 k.potzger@hzdr.de
5. 01/2013 – 12/2017 Helmholtz–Gemeinschaft HGF
   Professorship TU Chemnitz
   Prof. S. Gemming Phone: 0351 260 2470 s.gemming@hzdr.de
6. 03/2013 – 02/2014 Helmholtz–Gemeinschaft HGF
   HEF–i3membrane – nanopore metal filter
   Prof. A. Kolitsch Phone: 0351 260 3348 a.kolitsch@hzdr.de
7. 01/2014 – 12/2018 Helmholtz–Gemeinschaft HGF
   Spintronics – Helmholtz Young Investigators' Group
   Dr. A.M. Deac Phone: 0351 260 3709 a.deac@hzdr.de
8. 03/2014 – 02/2017 Helmholtz–Gemeinschaft HGF
   HGF Postdoc Dr. Yu Liu – Functional Materials
   Prof. M. Helm Phone: 0351 260 2260 m.helm@hzdr.de

9. 11/2014 – 10/2017 Helmholtz–Gemeinschaft HGF
HGF Postdoc Dr. K. Schultheiß – Magnetism
Prof. J. Faßbender Phone: 0351 260 3096 j.fassbender@hzdr.de

German Science Foundation Projects

1. 02/2010 – 06/2015 Deutsche Forschungsgemeinschaft DFG
HybMagMat – Hybride magnetic materials
Prof. J. Fassbender Phone: 0351 260 3096 j.fassbender@hzdr.de

2. 08/2010 – 06/2014 Deutsche Forschungsgemeinschaft DFG
SuSi – Superconductivity in heavily doped group-IV supercondcutors
Dr. V. Heera Phone: 0351 260 3343 v.heera@hzdr.de

3. 09/2010 – 07/2015 Deutsche Forschungsgemeinschaft DFG
TERATOP – Terahertz non–linear detection and quantum optical studies by resonant two–photon transitions in semiconductor quantum wells
Dr. H. Schneider Phone: 0351 260 2880 h.schneider@hzdr.de

4. 11/2010 – 06/2014 Deutsche Forschungsgemeinschaft DFG
Atomistic simulation of selforganization by ion-beam erosion
Dr. K.–H. Heinig Phone: 0351 260 3288 k.h.heinig@hzdr.de

5. 11/2010 – 12/2016 Deutsche Forschungsgemeinschaft DFG
Relaxation dynamics in graphene
Dr. S. Winnerl Phone: 0351 260 3522 s.winnerl@hzdr.de

6. 01/2011 – 09/2014 Deutsche Forschungsgemeinschaft DFG
Interaction of slow highly charged ions with surfaces
Dr. S. Facsko Phone: 0351 260 2987 s.facsko@hzdr.de

7. 01/2011 – 02/2014 Deutsche Forschungsgemeinschaft DFG
Selforganized surface patterns on germanium by heavy cluster ions
Dr. L. Bischoff Phone: 0351 260 2963 l.bischoff@hzdr.de

8. 03/2011 – 02/2014 Deutsche Forschungsgemeinschaft DFG
HISENSE – High–field studies of the band dispersion in novel semiconductor materials
Dr. O. Drachenko Phone: 0351 260 3593 o.drachenko@hzdr.de

9. 04/2011 – 06/2015 Deutsche Forschungsgemeinschaft DFG
FRUSTPART – Nucleation of spin order in low-dimensional colloidal particle systems
Dr. A. Erbe Phone: 0351 260 2366 a.erbe@hzdr.de

10. 08/2011 – 07/2014 Deutsche Forschungsgemeinschaft DFG
Nanostructuring of surfaces with direct extraction of ions from plasma sources
Dr. S. Facsko Phone: 0351 260 2987 s.facsko@hzdr.de

11. 03/2012 – 06/2014 Deutsche Forschungsgemeinschaft DFG
Space-resolved ferromagnetic resonance
Dr. J. Lindner Phone: 0351 260 3221 j.lindner@hzdr.de

12. 09/2012 – 09/2015 Deutsche Forschungsgemeinschaft DFG
ATOMIX – Atomic mixing in semiconductor layers
Dr. M. Posselt Phone: 0351 260 3279 m.posselt@hzdr.de

13. 01/2013 – 12/2015 Deutsche Forschungsgemeinschaft DFG
MWN – Magnetization dynamics in nanostructures
Dr. J. Lindner Phone: 0351 260 3221 j.lindner@hzdr.de

14. 01/2013 – 10/2017 Deutsche Forschungsgemeinschaft DFG
Cluster of Excellence – Center for Advancing Electronics Dresden
Prof. M. Helm Phone: 0351 260 2260 m.helm@hzdr.de

15. 02/2013 – 01/2016 Deutsche Forschungsgemeinschaft DFG
Nanostructured thermoelectrics
Dr. P. Zahn Phone: 0351 260 3121 p.zahn@hzdr.de

16. 08/2013 – 07/2014 Deutsche Forschungsgemeinschaft DFG
Magnetic Si:Mn
Dr. S. Zhou Phone: 0351 260 2484 s.zhou@hzdr.de

17. 04/2014 – 03/2016 Deutsche Forschungsgemeinschaft DFG
Dynano – Spin wave excitations in periodic nanostructures
Dr. K. Lenz Phone: 0351 260 2435 k.lenz@hzdr.de

18. 05/2014 – 04/2019 Deutsche Forschungsgemeinschaft DFG
Emmy Noether Junior Research Group - Magnonics
Dr. H. Schultheiß Phone: 0351 260 3243 h.schultheiss@hzdr.de

19. 07/2014 – 07/2015 Deutsche Forschungsgemeinschaft DFG
Time-resolved spectroscopy under high pressure
Dr. A. Pashkin Phone: 0351 260 3287 o.pashkin@hzdr.de

20. 11/2014 – 10/2017 Deutsche Forschungsgemeinschaft DFG
Thermal spin-transfer torques
Dr. J. Lindner Phone: 0351 260 3221 j.lindner@hzdr.de
Dr. A.M. Deac Phone: 0351 260 3709 a.deac@hzdr.de

Federally Funded Projects

1. 01/2012 – 11/2014 AG Industrieller Forschungseinrichtungen (AiF) BMWi
Oxidation protection of titanium alloys at high temperatures
Prof. A. Kolitsch Phone: 0351 260 3348 a.kolitsch@hzdr.de

2. 02/2013 – 07/2015 AG Industrieller Forschungseinrichtungen (AiF) BMWi
CFD-surface coating
Prof. A. Kolitsch Phone: 0351 260 3348 a.kolitsch@hzdr.de

3. 05/2013 – 04/2015 PT Jülich BMWi
Analytical ion-microscope
Dr. J. v. Borany Phone: 0351 260 3378 j.v.borany@hzdr.de

4. 06/2013 – 05/2015 PT Jülich BMWi
AIDA – Apparatus for in-situ defect analysis
Dr. K. Potzger Phone: 0351 260 3244 k.potzger@hzdr.de

5. 11/2013 – 10/2014 PT Jülich BMWi
BFO in wafer-quality
Dr. W. Skorupa Phone: 0351 260 3612 w.skorupa@hzdr.de

6. 01/2014 – 06/2017 PT Jülich BMBF
In-situ TEM
Prof. J. Fassbender Phone: 0351 260 3096 j.fassbender@hzdr.de

7. 10/2014 – 09/2015 PT Jülich BMWi
PolCarr – Electrically polarizable materials
Dr. K. Wiesenhütter Phone: 0351 260 2065 k.wiesenhuetter@hzdr.de

8. 10/2014 – 09/2017 PT Jülich BMBF
InTerFEL – High-field spectroscopy in the THz regime
Dr. H. Schneider Phone: 0351 260 2065 h.schneider@hzdr.de

Saxony State Funded Projects

1. 04/2012 – 03/2014 Sächsische Aufbaubank SAB
   ADDE II: H–passivation
   Dr. W. Skorupa Phone: 0351 260 3612 w.skorupa@hzdr.de
2. 06/2012 – 05/2014 Sächsische Aufbaubank SAB
   NanoKlang – corrosion protection of metallic organ-pipes
   Dr. W. Skorupa Phone: 0351 260 3612 w.skorupa@hzdr.de
3. 02/2014 – 12/2014 SMWK SMWK
   BFO-logic
   Dr. L. Rebohle Phone: 0351 260 3368 l.rebohle@hzdr.de

Personnel Exchange Projects

1. 01/2013 – 12/2014 Deutscher Akademischer Austauschdienst DAAD
   Personnel exchange with China: DFT and MC studies
   Dr. M. Posselt Phone: 0351 260 3279 m.posselt@hzdr.de
2. 01/2013 – 12/2014 Deutscher Akademischer Austauschdienst DAAD
   Personnel exchange with Norway: Flash-PV
   Dr. W. Skorupa Phone: 0351 260 3612 w.skorupa@hzdr.de
3. 07/2014 – 09/2014 Deutscher Akademischer Austauschdienst DAAD
   Visit of Dr. Semisalova
   Dr. S. Zhou Phone: 0351 260 2484 s.zhou@hzdr.de

Bilateral Projects

1. 04/2010 – 03/2014 FHR Anlagenbau / Centrotherm Industry
   Development of an industry-suited temperature measurement
   Dr. W. Skorupa Phone: 0351 260 3612 w.skorupa@hzdr.de
2. 07/2012 – 06/2016 Abengoa Research, Seville, Spain Industry
   AR Framework Collaboration
   Prof. S. Gemming Phone: 0351 260 2470 s.gemming@hzdr.de
3. 10/2012 – 12/2016 Carl–Zeiss Microscopy Industry
   Collaboration on analytical ion microscopy
   Dr. J. v. Borany Phone: 0351 260 3378 j.v.borany@hzdr.de
4. 06/2013 – 12/2014 TUD-Energietechnik TUD
   Fracture mechanics after neutron embrittlement
   Dr. H.–W. Viehrig Phone: 0351 260 3246 h.w.viehrig@hzdr.de
5. 10/2013 – 06/2015 TÜV Süd
   Education and Training CAMBO Bratislava
   Prof. A. Kolitsch Phone: 0351 260 3348 a.kolitsch@hzdr.de

Doctoral training programme

International Helmholtz Research School NanoNet

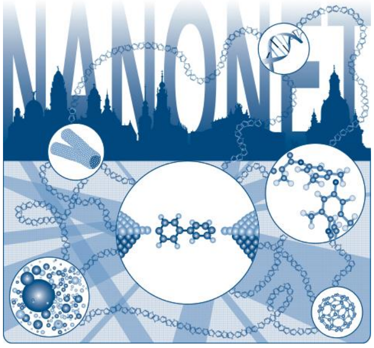

The Institute of Ion Beam Physics and Materials Research is coordinating the International Helmholtz Research School for Nanoelectronic Networks (IHRS NanoNet) supported by the Initiative and Networking Fund of the Helmholtz Association. The project started in October 2012. The total funding is 1.2 Mio. € for a period of six years.

The IHRS NanoNet is an international, interdisciplinary and thematically focused doctoral programme in the field of molecular electronics. The research school aims at attracting and promoting excellence by educating promising doctoral candidates with backgrounds in physics, chemistry, materials science and electrical engineering. During a period of three years PhD candidates benefit from well-structured, comprehensive training curricula and multiple mentorship, while performing cutting edge research projects within one of the 14 NanoNet research groups. Under the supervision of outstanding scientists leading the field of nanoelectronics, the doctoral candidates have the unique opportunity to contribute to the advancement of molecular electronics by developing strategies for the real integration of single nanosized building blocks into large interconnected networks.

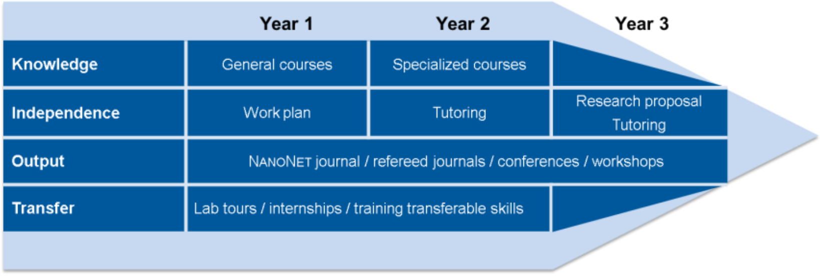

	Year 1	Year 2	Year 3
Knowledge	General courses	Specialized courses	
Independence	Work plan	Tutoring	Research proposal Tutoring
Output	NanoNet journal / refereed journals / conferences / workshops		
Transfer	Lab tours / internships / training transferable skills		

Annual International NanoNet Workshop

PhD seminar

The period of doctoral studies is crucial in the academic career of young scientists. Therefore, the IHRS NanoNet fosters not only professional qualification but also personal development by equipping young graduates with competencies for successful careers in a wide variety of positions in academia and industry. The training programme invests on professional competencies, such as the capability to work across disciplines and cultures by promoting networking and the exchange of ideas and knowledge with fellows, mentors and collaboration partners. The cooperation with international scientific and industrial partners complements and broadens the expertise of the IHRS NanoNet by establishing a unique research and training network for its doctoral candidates.

The consortium

- Helmholtz-Zentrum Dresden-Rossendorf (HZDR)
- Technische Universität (TU) Dresden
- Leibniz Institute of Polymer Research (IPF) Dresden
- Fraunhofer Institute for Ceramic Technologies and Systems (IKTS) Dresden
- Nanoelectronic Materials Laboratory (NaMLab) gGmbH Dresden

For further information please contact the NanoNet coordinator, Dr. Peter Zahn (nanonet@hzdr.de) or visit the IHRS NanoNet website: www.ihrs-nanonet.de

Experimental equipment

Accelerators, ion implanters and ion-assisted-deposition

Van de Graaff Accelerator (VdG)	2 MV	*TuR Dresden, DE*
Tandetron Accelerator (T1)	3 MV	*HVEE, NL*
Tandetron Accelerator (T2)	6 MV	*HVEE, NL*
Low-Energy Ion Implanter	0.5 - 50 kV	*Danfysik, DK*
High-Current Ion Implanter	20 - 200 kV	*Danfysik, DK*
High-Energy Ion Implanter	40 - 500 kV	*HVEE, NL*
Plasma Immersion Ion Implantation	5 - 60 keV	*GBR, DE / Home-built*
Focused Ion Beam (15 nm, variable ions)	30 keV, 10 A/cm^2	*Orsay Physics, FR*
Helium/Neon Ion Microscope	10-40 keV	*Zeiss, DE*
Highly-Charged Ion Facility	25 eV – 25 keV × Q Q = 1…40 (Xe)	*Home-built*
High-Power Impulse Magnetron Sputtering		*Melec, DE*
Ion-Beam Sputtering	200 - 2000 V	*Home-built*
UHV Ion Irradiation (Ar, He, etc.)	0 - 5 keV Scan 10×10 mm^2	*VG, USA*

Ion Beam Analysis (IBA)

A wide variety of advanced IBA techniques are available at the MeV accelerators (see figure).

RBS	Rutherford Backscattering Spectrometry	(1), (9), (11), (12), (21)	*VdG, T1, T2*
RBS/C	RBS + Channelling	(1), (9), (11), (12)	*VdG, T1, T2*
HR-RBS	High-Resolution RBS/C	(9), (13)	*T1*
ERDA	Elastic Recoil Detection Analysis	(1), (4)	*VdG, T2*
PIXE	Particle-Induced X-ray Emission	(1), (5), (6), (12)	*VdG, T1, T2*
PIGE	Particle-Induced γ Emission	(6), (12)	*T1, T2*
NRA	Nuclear Reaction Analysis	(3)	*T2*
NRRA	Nuclear Resonance Reaction Analysis	(11)	*T1*
NMP	Nuclear Microprobe	(12)	*T1*
AMS	Accelerator Mass Spectrometry (focused to cosmic radionuclides: ^{10}Be, ^{26}Al, ^{36}Cl, ^{41}Ca, ^{129}I)	(10)	*T2*

Some stations are equipped with additional process facilities enabling *in-situ* IBA investigations during ion irradiation, sputtering, deposition, annealing etc.

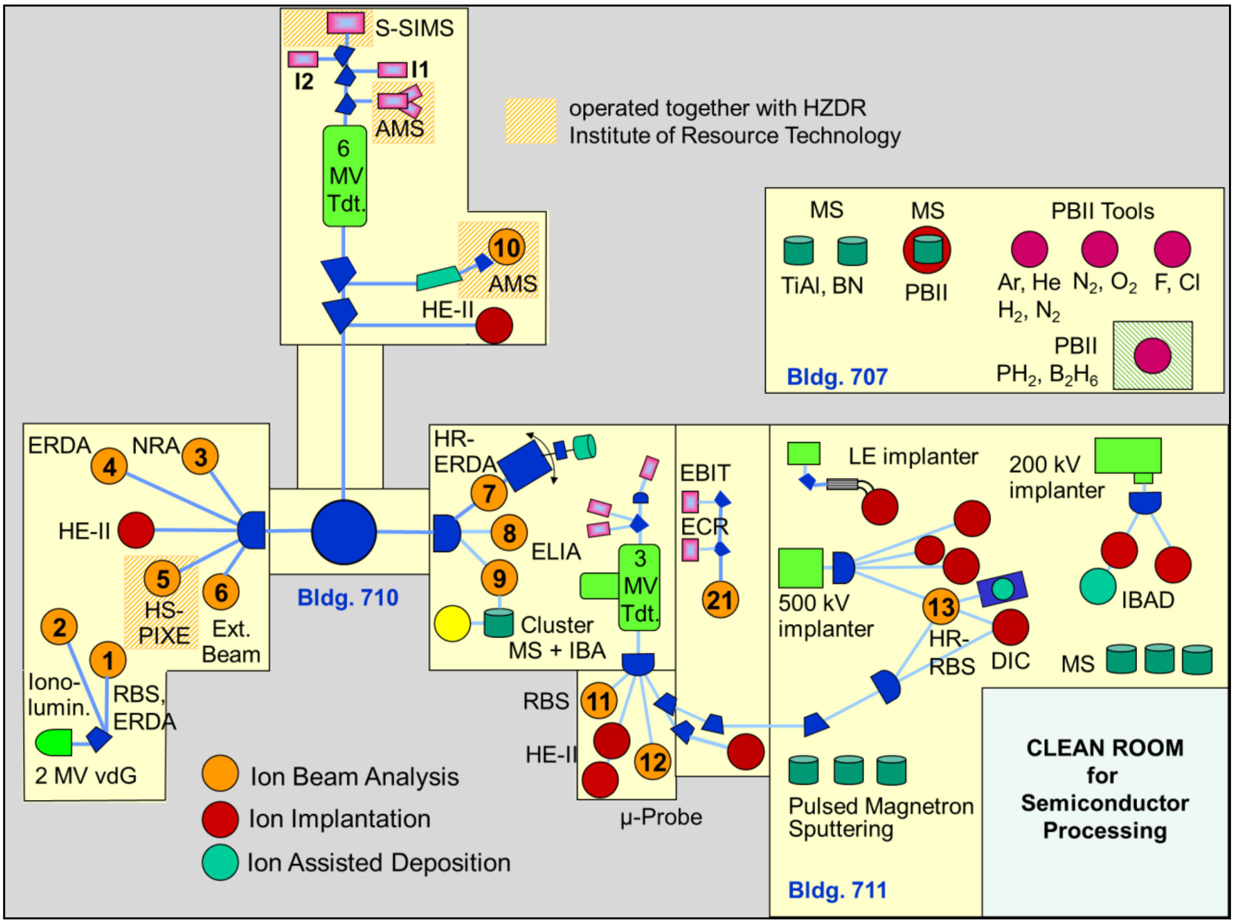

Schematic overview of the Ion Beam Center

Other particle-based analytical techniques

SEM	Scanning Electron Microscope	1 - 30 keV + EDX	*Hitachi, JP*
TEM	Transmission Electron Microscope (Titan 80-300 with Image Corrector)	80 - 300 keV + EDX, +GIF	*FEI, NL*
SIM	Scanning Ion Microscope (ORION NanoFab with He, Ne ions)	10 - 35 keV + GIS, Patterning	*Zeiss Microscopy, DE*
FIB/SEM	Focused Ion / Electron Cross Beam (NVision 40 with Elphy Plus Litho)	0.5 – 30 keV + EDX, EBSD	*Zeiss-NTS, DE* *Raith, Bruker, DE*
AES	Auger Electron Spectroscopy	+ XPS	*Fisions, UK*
CEMS	Mössbauer Spectroscopy	^{57}Fe source	*Home-built*
PAS	Positron Annihilation Spectroscopy	^{22}Na source 30 V - 36 kV	*Home-built*

Photon-based analytical techniques

XRD / XRR	X-Ray Diffraction and Reflection	Cu-Kα	*Bruker AXS, DE*
HR-XRD	High-Resolution XRD	Cu-Kα	*GE Inspection, DE*
TFA	Thin Film Analysis, including Grazing Incidence Small Angle Scattering (GiSAXS)	Cu-Kα	*PANalytical, NL*
XRD / XRR	with Synchrotron Radiation	5 – 35 keV	*ROBL at ESRF, FR*
SE	Spectroscopic Ellipsometry	250 - 1700 nm	*Woollam, US*
UV-Vis	Solid Spec 3700 DUV	190 - 3300 nm	*Shimadzu,JP*
FTIR	Fourier-Transform Infrared Spectrometer	600 - 7000 cm^{-1}	*Nicolet, US*
FTIR	Fourier-Transform Infrared Spectrometer	50 - 15000 cm^{-1}	*Bruker, DE*
	Ti:Sapphire Femtosecond Laser	78 MHz	*Spectra Physics, US*
	Femtosecond Optical Parametric Osci.		*APE, DE*
	Ti:Sapphire Femtosecond Amplifier	1 kHz	*Femtolasers, AT*
	Ti:Sapphire Femtosecond Amplifier	250 kHz	*Coherent, US*
	Femtosecond Optical Parametric Amplifier		*Light Conversion, LI*
THz-TDS	Terahertz Time-Domain Spectroscopy	0.1 - 4 THz	*Home-built*
Raman	Raman Spectroscopy	> 45 cm^{-1} shift	*Jobin-Yvon-Horiba, FR*
	In-situ Raman Spectroscopy	> 100 cm^{-1}	*Jobin-Yvon-Horiba, FR*
PL	Photoluminescence (10-300 K)	300 - 1600 nm	*Jobin-Yvon-Horiba, FR*
TRPL	Time-Resolved PL	τ = 3 ps - 2 ns τ > 5 ns	*Hamamatsu Phot., JP* *Stanford Research, US*
EL	Electroluminescence	300 - 1600 nm	*Jobin-Yvon-Horiba, FR*
	Optical Split-Coil Supercond. Magnet	7 T	*Oxford Instrum., UK*
PR	Photomodulated Reflectivity	300 - 1600 nm	*Jobin-Yvon-Horiba, FR*
PLE	Photoluminescence Excitation	300 - 1600 nm	*Jobin-Yvon-Horiba, FR*
OES	Optical Emission Spectroscopy	250 – 800 nm	*Jobin-Yvon-Horiba, FR*

Magnetic thin film deposition and analysis

MBE	Molecular Beam Epitaxy with in-situ FIB		*CreaTec, DE*
PLD	Pulsed Laser Deposition		*SURFACE, DE*
MFM	Magnetic Force Microscope	~ 50 nm resol.	*VEECO / DI, US*
SQUID MPSM	Supercond. Quantum Interference Device	± 7 T	*Quantum Design, US*
SQUID VSM	Vibrating Sample Magnetometer	± 7 T	*Quantum Design, US*
FR-MOKE	Frequency-resolved Magneto-Optic KE	± 1.1 T	*Home-built*
MOKE	Magneto-Optic Kerr Effect (in-plane)	± 0.35 T	*Home-built*
MOKE	Magneto-Optic Kerr Effect (perpend.)	± 2 T	*Home-built*
SKM	Scanning Kerr Microscope		*Home-built*
	Kerr Microscope		*Evico Magnetics, DE*
TR-MOKE	Time-Resolved MOKE (Pump-Probe)		*Home-built*

VNA-FMR	Vector Network Analyzer Ferromagnetic Resonance	*Agilent / Home-built*
ME	Magnetoellipsometer	*LOT, DE; AMAC, US*

Other analytical and measuring techniques

STM	UHV Scanning Tunneling Microscope (variable T)		*Omicron, DE*
AFM	Atomic Force Microscope (Tapping Mode)		*SIS, DE*
AFM	Atomic Force Microscope (with c-AFM, SCM-Module)		*Bruker, US*
	Dektak Surface Profilometer		*Bruker, US*
	Micro Indenter / Scratch Tester		*Shimatsu, JP*
MS	Mass Spectrometers (EQP-300, HPR-30)		*HIDEN, DE & US*
	Wear Tester (pin-on disc)		*Home-built*
LP	Automated Langmuir Probe		*Impedans, IE*
HE	Hall Effect Equipment	2 - 400 K, ≤ 9 T	*LakeShore, US*
RS	Sheet-Rho-Scanner		*AIT, South Korea*
DLTS	Deep Level Transient Spectroscopy	(+ I-U / C-V) (10 - 300 K, 1 MHz)	*PhysTech, DE*
IV / CV	Photocapacitance (+I-V/G-V)	(250 - 2500 nm)	*Home-built*
IV / CV	I-V and C-V Analyzer		*Keithley, US*
IV / CV	I-V and C-V Semi-Automatic Prober	(-60 – 300°C)	*Süss, DE; Keithley, US*
IV	I-V Prober	(4.2 – 600 K)	*LakeShore, Agilent, US*

Deposition and processing techniques

Physical Deposition	Sputtering DC / RF, Evaporation	*Nordiko, UK*
	Electron Beam Evaporation System	*Leybold Optics, DE*
	Thermal Evaporation	*Bal-Tec, LI*
Semiconductor Molecular Beam Epitaxy	III-V semiconductors	*Riber, FR*
Chemical Deposition	Plasma Enhanced CVD (for a-Si, a-Ge, SiO_2, SiON, Si_3N_4)	*Oxford Instruments, UK*
Atomic Layer Deposition	Al_2O_3, HfO_2, SiO_2	*Ultratech, US*
Dry Etching	Plasma and RIE Mode	*Sentech, DE*
Reactive Ion Beam Etching	∅ 6”, Ar, CF_4	*Roth & Rau, DE*
Etching / Cleaning	incl. Anisotropic Selective KOH Etching	
Photolithography	Mask-Aligner, 2 µm-level	*Süss, DE*
Electron Beam Lithography	Raith 150-TWO: ∅ 6”, 10 nm res.	*Raith, DE*
Thermal Treatment	Room Temperature - 2000°C	
• Furnace		*InnoTherm, DE*
• Rapid Thermal Annealing		*ADDAX, FR*
• Flash-Lamp Units (0.5 – 20 ms)		*Home-built; FHR, DTF, DE*
• RF Heating (Vacuum)		*JIP.ELEC, FR*
• Laser annealing (CW, 808 nm, 450 W)		*LIMO, DE*

- Laser annealing (30 ns pulse,10 Hz, 308 nm, 500 mJ) *COHERENT, USA*

Bonding Techniques	Ultrasonic Wire Bonding	*Kulicke & Soffa, US*
Cutting, Grinding, Polishing		*Bühler, DE*
TEM Sample Preparation	Plan View and Cross Section incl. Ion Milling Equipment	*Gatan, US*

Hot cells laboratory

Mechanical testing of neutron irradiated structural materials	max. total activity 5 TBq (Co-60), T = -150 ... +315 °C	
Fracture mechanics testing	max load ±50 kN	MTS, US
Charpy impact testing	300 J	WPM Leipzig, DE
Small punch test	10 kN	Hegewald & Peschke, DE
Specimen preparation	Electrical discharge machining	AGIE, DE
Depth sensing nanoindentation/ AFM	UNAT, load range 1 … 500 mN	ASMEC, DE

User facilities and services

Ion Beam Center (IBC)

The Ion Beam Center (IBC) at HZDR combines various machines (electrostatic accelerators, ion implanters, plasma-based equipment) into a unique facility primarily used for ion beam modification and ion beam analysis of materials. The available energy range spans from a few eV to almost 100 MeV with a respective interaction depth in solids between 0.1 nm to 10 µm. In addition to standard broad beams also focused (down to 1 nm) and highly-charged (charge state up to +45) ion beams are provided. In addition to these ion beam facilities, structural analysis (electron microscopy and spectroscopy, X-ray scattering techniques) and sample or device processing under clean-room conditions can be utilized at IBC to deliver a "complete" user service. A schematic overview of the IBC including the description of the main beam lines and experimental stations is given at page 78 of this Annual Report. In 2014 about 12.000 beam time hours were delivered to 350 users from 25 countries worldwide performing experiments at IBC or using the capabilities for ion beam services.

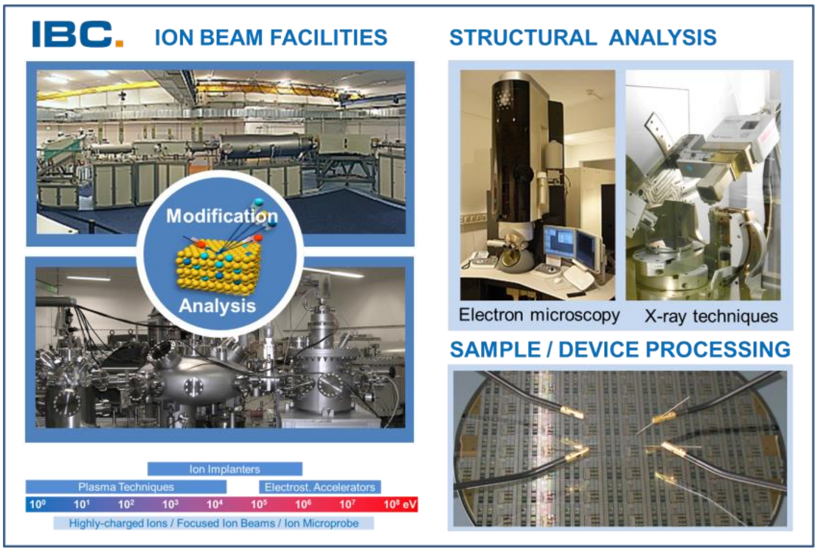

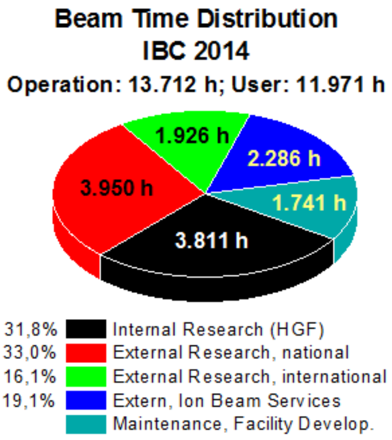

After HZDR joined the Helmholtz Association in 2011, IBC activities have been integrated efficiently into various Helmholtz programmes within the research field "Matter", but also in the Helmholtz cross-programme activities "Mineral Resources", "Helmholtz Climate Initiative" and "Materials Research for Energy Technologies". From the beginning of 2015 the IBC has the status as a Helmholtz LK-II User Facility. Moreover, from 2013 the IBC has been recognized as a large-scale facility within the "BMBF Verbundforschung" program promoting long-term collaborations with universities.

The IBC demonstrates its outstanding status in relation to other international ion beam facilities by the following features:

- The IBC has provided ion beam technology as a user and competence center for ion beam applications for more than 30 years. With respect to user beam time hours the IBC is internationally leading and has been supported by numerous national and European grants and by industry.
- IBC activities cover both ion beam modification as well as ion beam analysis (IBA). Experienced staff is present to support IBC users and to enhance the experimental capabilities to their needs.

- Operation of IBC is accompanied by a strong in-house research at the affiliated host institute, both in experiment and theory. This allows in-depth research in targeted research areas as well as the exploration of new application fields for ion beam technology.

Following the rules of a European and national user facility, access for scientific experiments to IBC is provided on the basis of a proposal procedure (www.hzdr.de/IBC) via the common HZDR user facility portal **HZDR-GATE** (gate.hzdr.de). Due to the availability of multiple machines and versatile instrumentation, continuous submission of IBC proposals can be offered (no deadline). The scientific quality of the proposals is steadily evaluated and ranked by an external international User Selection Panel (USP). For successfully evaluated proposals, users get free access to IBC facilities for their experiments which can be often realized within three month after proposal submission. The use of the IBC facilities includes the scientific and technical support during planning, execution and subsequent evaluation of the experiments.

The IBC has a strong background in the commercial exploitation of ion beam technology with partners from industry which is essential for materials science applications. For ion beam services the HZDR Innovation GmbH (spin-off of the HZDR) – www.hzdr-innovation.de – provides a direct and fast access to the IBC facilities based on individual contracts. The close collaboration between IBC and HZDR Innovation GmbH is considered as a reference model aiming to develop innovative strategies for an effective contribution of Helmholtz large-scale facilities for economic innovation. Currently, about 20% of the total IBC beam time is used for commercial ion beam services.

The IBC pursues two strategic objectives for further development. On one hand, it is focused on the successful operation as an international user facility to sustain its position as a leading European ion beam center in the fields of materials and interdisciplinary research. This requires the continuous development and extension of ion beam technologies. Special emphasis is directed towards new R&D areas and communities which so far have not been aware of the advantages of ion technology. On the other hand, cutting edge scientific challenges, in particular for the modification and understanding of the function of materials at the nano-scale down to the atomic level, is addressed in order to achieve new functionalities and to design novel materials. These challenges comprise:

- the extended application of low-energy ions for modification and analysis of ultra-thin films, surfaces, 2D materials and molecular layers based on a new **L**ow **E**nergy **I**on **N**ano-**E**ngineering **F**acility (LEINEF) which is currently projected for first experiments in 2017,

- the investigation of material states and modifications far from equilibrium induced by high-energy density excitations with cluster and highly-charged ions,

- the exploration of new IBA approaches with unprecedented lateral resolution, ultimate detection limit and high sample throughput, e.g. for resource technology. In this context, a fruitful and close collaboration between the IBC and the Helmholtz Institute of Resource Technology (www.hzdr.de/fwg) has been developed during last years. With projects like “High-Speed-PIXE” and “Super-SIMS”, the interdisciplinary work of IBC will be substantially extended towards the application of ion beam analysis methods in geosciences and resource technology.

In 2013, some new ion beam tools or end-stations have been commissioned which will attract new users by cutting-edge experimental instrumentation. As an example, the installation and routine operation of the ion microscope *ORION NanoFab* (He / Ne ions, 10 - 40 keV) is mentioned enabling unique possibilities for ion imaging and nano-fabrication with feature sizes below 10 nm. The development of ion beam analysis capabilities for this instrument is presently under study.

For more detailed information please contact Dr. Johannes von Borany (j.v.borany@hzdr.de) or Dr. Stefan Facsko (s.facsko@hzdr.de) and visit the IBC webpage: www.hzdr.de/IBC.

Free Electron Laser FELBE

ELBE is an acronym for the free-electron laser (FEL) at the Electron Linear accelerator with high Brilliance and low Emittance (ELBE) located at the Helmholtz-Zentrum Dresden-Rossendorf, Germany. The heart of ELBE is a superconducting linear accelerator operating in cw mode with a pulse repetition rate of 13 MHz. The electron beam (40 MeV, 1 mA max.) is guided to several laboratories where secondary beams (particle and electromagnetic) are generated. Two free-electron lasers (U27-FEL and U100-FEL) produce intense, coherent electromagnetic radiation in the mid and far infrared, which is tunable over a wide wavelength range (4 – 250 µm) by changing the electron energy or the undulator magnetic field. Main parameters of the infrared radiation produced by FELBE are as follows:

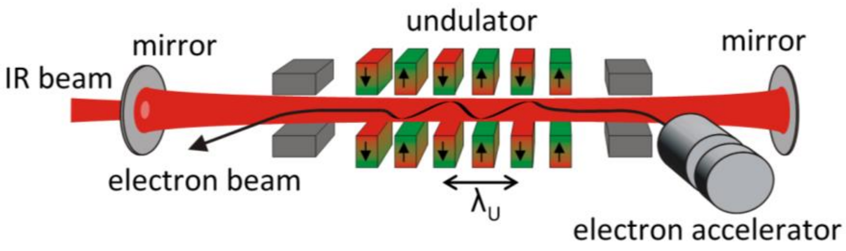

Wavelength λ	4 – 22 µm 18 – 250 µm	FEL with undulator U27 FEL with undulator U100
Pulse energy	0.01 – 2 µJ	depends on wavelength
Pulse length	1 – 25 ps	depends on wavelength
Repetition rate	13 MHz	3 modes: • cw • macropulsed (> 100 µs, < 25 Hz) • single pulsed (Hz…kHz)

The free electron laser is a user facility. Applications for beam time can be submitted twice a year, typically by April 15 and October 15. Users from EU countries can receive support through the FP7 Integrated Infrastructure Initiative (I3) CALIPSO (**C**oordinated **A**ccess to **LI**ghtsources to **P**romote **S**tandards and **O**ptimization).

Typical applications are picosecond pump-probe spectroscopy (also in combination with several other femtosecond lasers, which are synchronized to the FEL), near-field microscopy and nonlinear optics. The FELBE facility also serves as a far-infrared source for experiments at the High-Field Laboratory Dresden (HLD) involving pulsed magnetic fields up to 70 Tesla.

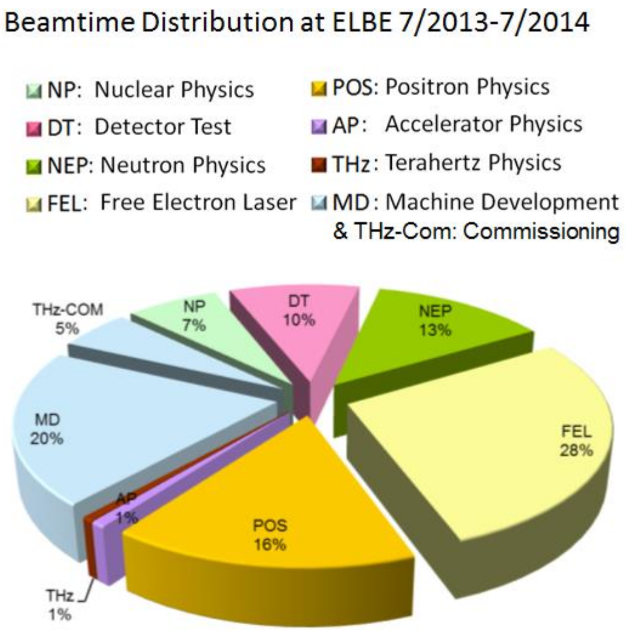

The statistics shows that the FEL used 1670 hours beamtime of the ELBE accelerator. This corresponds to 28 % of total beamtime, which is again distributed among internal and external users.

For further information please contact:
Prof. Manfred Helm (m.helm@hzdr.de)
or visit the FELBE webpage www.hzdr.de/FELBE.

ROssendorf BeamLine (ROBL)

Since 1998 the HZDR operates the Rossendorf Beamline at the ESRF. More than 220 days of beamtime are provided for user operation per year. Two experimental stations sharing one beamline optics are available: the station for X-ray spectroscopy of Actinides and other radionuclides (**R**adio **C**hemistry **H**utch RCH) and the **M**aterials **R**esearch **H**utch MRH. In 2012, the X-ray optics in the optics hutch was completely replaced. The new monochromator hosts three different sets of crystals and two different sets of multilayers. The higher photon flux of the multilayer is gained by a loss of energy resolution as displayed in the table below. In the energy range of 5 to 11.5 keV an unfocussed, parallel beam for high resolution diffraction experiments can be used, while from 9 to 35 keV the synchrotron radiation beam is focused by a toroidal mirror. By the new optics, the beamline gained in general more flexibility allowing to optimize the beamline parameters for each particular experiment.

Energy resolution	< 5×10^{-4} ΔE/E (Si(111)) < 1×10^{-4} ΔE/E (Si(311)) ~ 2×10^{-2} ΔE/E (multilayer ML)
Beam size	(10×0.5) mm^2 unfocussed (0.3×0.3) mm^2 focussed
Photon flux	8×10^{9} phot./(s.mm^2) unfocussed (Si111) > 3×10^{11} phot./(s.mm^2) focused (Si111) > 2×10^{13} phot./(s.mm^2) focused (ML)

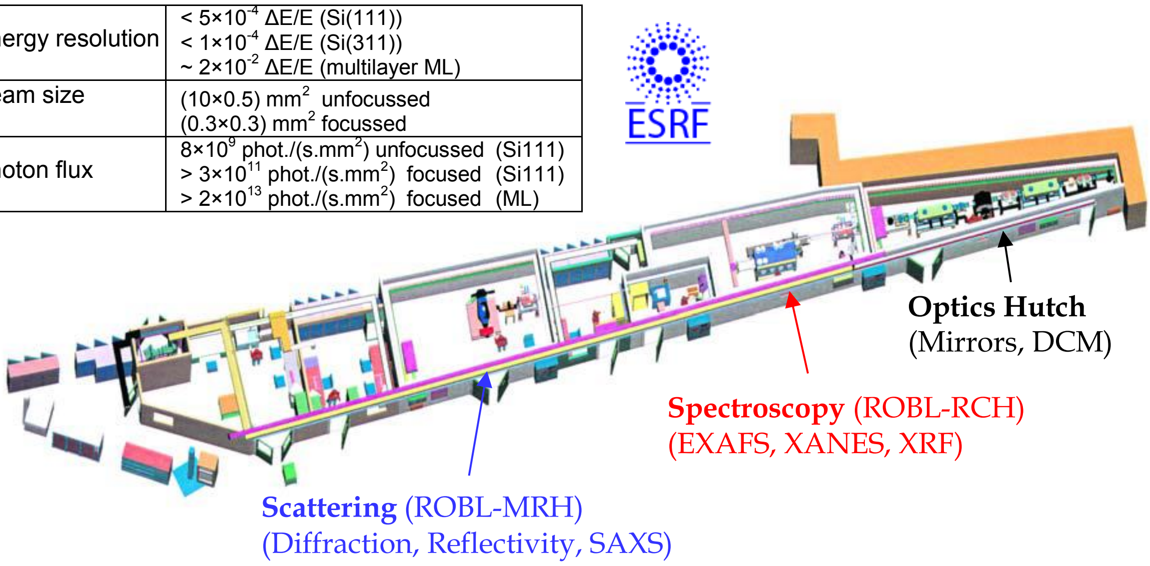

The majority of MRH experiments is dedicated to the analysis of nano-sized as well as nano-structured materials, thin films, multilayers or the investigation of crystalline phases in low concentration by different X-ray based methods like (anomalous) scattering and diffraction, even spectroscopy is possible. In the center of interest are in-situ investigations of materials under processing or synthesis conditions.

In particular highly specialized sample environments present at MRH need to be mentioned here. A three-port magnetron sputtering chamber is available for in-situ growth and annealing studies using DC and RF sputtering. Additionally one magnetron can be replaced by an ion gun permitting surface irradiation or ion implantation experiments. Thereby the implantation energy can be increased up to 20keV by applying an additional potential. The most requested sample chamber is a furnace equipped with a semispherical Be dome (for vacuum experiments) or with a Kapton window dome (for experiments at atmospheric pressures). The latter setup is dedicated to in-situ measurements operating with different reactive gases like acetylene, hydrogen, ammonia, benzene etc. used in CVD growth processes or hydrogen loading. Furthermore electrical measurements and in-situ X-ray experiments can be combined in these furnaces. Additionally, sample environments provided by users can be integrated in the set-up. All these experiments aim at the correlation of structural properties of materials with their functionality which is the key for a better material understanding.

For further information please contact

Dr. Andreas Scheinost (ROBL-RCH): scheinost@esrf.fr
Dr. Carsten Bähtz (ROBL-MRH): baehtz@esrf.fr
or visit the ROBL webpage: www.hzdr.de/ROBL

Organization chart

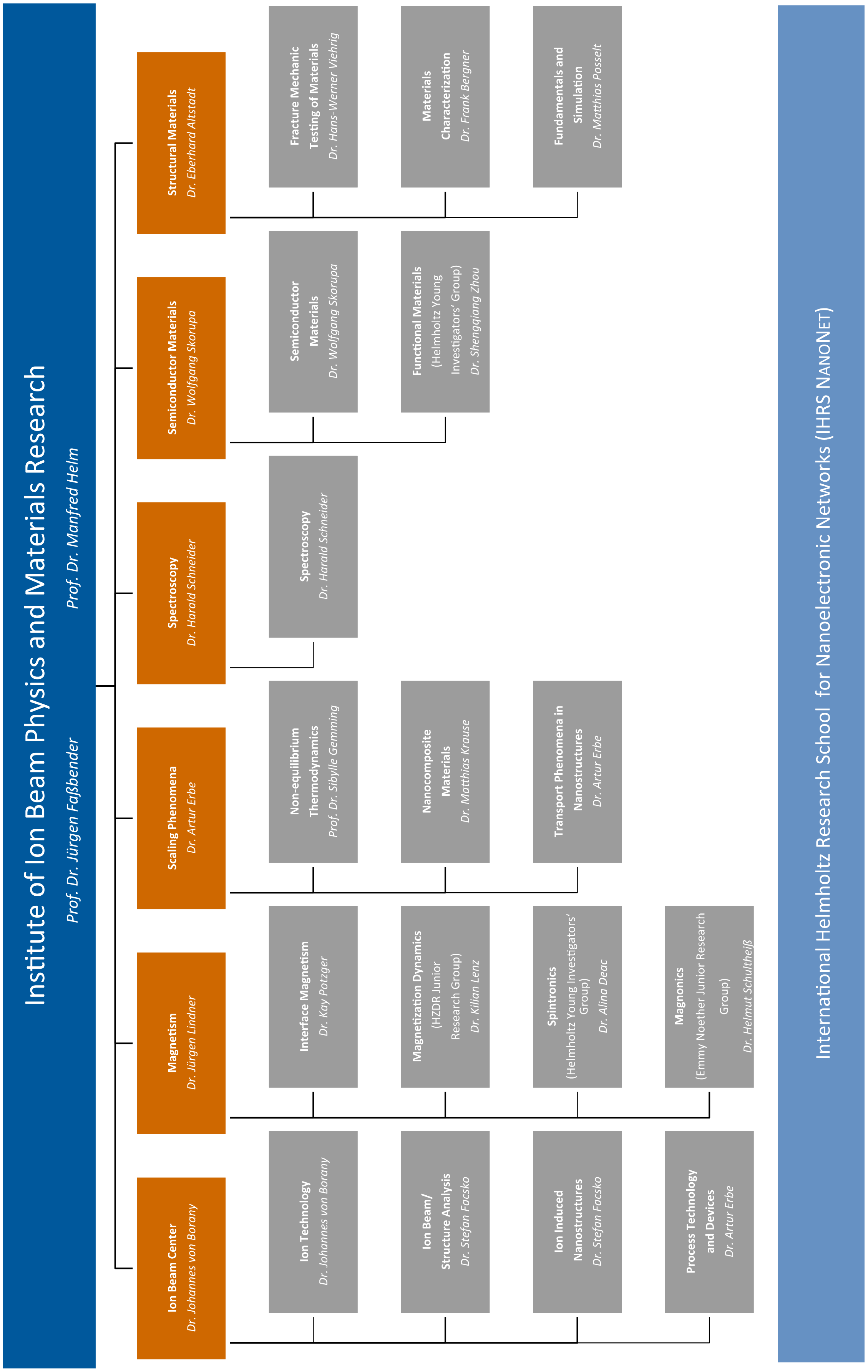

Institute of Ion Beam Physics and Materials Research
Prof. Dr. Jürgen Faßbender *Prof. Dr. Manfred Helm*

- **Ion Beam Center** *Dr. Johannes von Borany*
  - **Ion Technology** *Dr. Johannes von Borany*
  - **Ion Beam/ Structure Analysis** *Dr. Stefan Facsko*
  - **Ion Induced Nanostructures** *Dr. Stefan Facsko*
  - **Process Technology and Devices** *Dr. Artur Erbe*
- **Magnetism** *Dr. Jürgen Lindner*
  - **Interface Magnetism** *Dr. Kay Potzger*
  - **Magnetization Dynamics** (HZDR Junior Research Group) *Dr. Kilian Lenz*
  - **Spintronics** (Helmholtz Young Investigators' Group) *Dr. Alina Deac*
  - **Magnonics** (Emmy Noether Junior Research Group) *Dr. Helmut Schultheiß*
- **Scaling Phenomena** *Dr. Artur Erbe*
  - **Non-equilibrium Thermodynamics** *Prof. Dr. Sibylle Gemming*
  - **Nanocomposite Materials** *Dr. Matthias Krause*
  - **Transport Phenomena in Nanostructures** *Dr. Artur Erbe*
- **Spectroscopy** *Dr. Harald Schneider*
  - **Spectroscopy** *Dr. Harald Schneider*
- **Semiconductor Materials** *Dr. Wolfgang Skorupa*
  - **Semiconductor Materials** *Dr. Wolfgang Skorupa*
  - **Functional Materials** (Helmholtz Young Investigators' Group) *Dr. Shengqiang Zhou*
- **Structural Materials** *Dr. Eberhard Altstadt*
  - **Fracture Mechanic Testing of Materials** *Dr. Hans-Werner Viehrig*
  - **Materials Characterization** *Dr. Frank Bergner*
  - **Fundamentals and Simulation** *Dr. Matthias Posselt*

International Helmholtz Research School for Nanoelectronic Networks (IHRS NANONET)

List of personnel 2014

DIRECTORS

Prof. Dr. M. Helm, Prof. Dr. J. Fassbender

OFFICE

S. Gebel, S. Kirch

SCIENTIFIC STAFF

Permanent staff

Dr. G. Abrasonis
Dr. C. Akhmadaliev
Dr. E. Altstadt
Dr. C. Bähtz
Dr. F. Bergner
Dr. L. Bischoff
Dr. J. von Borany
Dr. S. Facsko
Dr. S. Gemming
Dr. J. Grenzer
Dr. V. Heera
Dr. R. Hübner
Dr. M. Krause
Dr. J. Lindner
Dr. A. Mücklich
Dr. G. Müller
Dr. F. Munnik
Dr. C. Neelmeijer
Dr. M. Posselt
Dr. K. Potzger
Dr. L. Rebohle
Dr. H. Reuther
Dr. H. Schneider
Dr. W. Skorupa
Dr. A. Ulbricht
Dr. H.-W. Viehrig
Dr. M. Voelskow
Dr. M. Werner
Dr. S. Winnerl

Non-permanent

Dr. A. Bakaev (P)
Dr. R. Bali
Dr. R. Böttger
Dr. F. Bregolin (P)
Dr. V. Cantelli
Dr. A. Cordeiro (P)
Dr. S. Cornelius (P)
Dr. A. Deac
Dr. M. Devaraj (P)
Dr. E. Dimakis
Dr. A. Erbe
Dr. J. Fiedler (P)
Dr. C. Fowley
Dr. M. Friedrich (P)
Dr. K.-H. Heinig
Dr. C. Heintze
Dr. R. Heller
Dr. G. Hlawacek (P)
M. Houska (P)
Dr. E. Josten
Dr. A. Kakay
Dr. A. Keller
Dr. J. Kerbusch (P)
Dr. M. Khalid (P)
Prof. A. Kolitsch (P)
Dr. K. Lenz
Dr. B. Liedke (P)
Dr. Y. Liu (P)
Prof. W. Möller (P)
Dr. X. Ou
Dr. A. Pashkin
Dr. S. Prucnal (P)
Dr. H. Schultheiß (P)
Dr. T. Sebastian (P)
Dr. V. Sluka
Dr. S. Stienen (P)
Dr. K. Wiesenhütter (P)
Dr. U. Wiesenhütter (P)
Dr. R. Wilhelm
Dr. S. Wintz
Dr. R. Yankov (P)
Dr. P. Zahn (P)
Dr. S. Zhou (P)

(P) Projects

TECHNICAL STAFF

Permanent staff

Rb. Aniol
Ry. Aniol
E. Christalle
S. Eisenwinder
B. Gebauer
D. Hanf
J. Haufe
A. Henschke
H. Hilliges
S. Klare
J. Kreher
A. Kunz
H. Lange
U. Lucchesi
F. Ludewig
R. Mester
M. Mißbach
C. Neisser
F. Nierobisch
J. Pietzsch
T. Putzke
A. Reichel
H. Richter
M. Roßner
S. Rott
B. Scheumann
G. Schnabel
A. Schneider
A. Scholz
T. Schumann
U. Skorupa
M. Steinert
A. Thiel
K. Thiemig
A. Vetter
J. Wagner
W. Webersinke
R. Weidauer
A. Weise
R. Weiss
J. Winkelmann
I. Winkler
L. Zimmermann
J. Zscharschuch

Non-permanent

T. Schönherr (P)
I. Skorupa (P)
A. Weißig (P)

(P) Projects

PhD STUDENTS

Y. Aleksandrov
A. W. Awan
A. Banholzer
K. Bernert
D. Blaschke
J. Braun
A. Bogusz
J. Buchriegler
A. Das
D. Deb
J. Ehrler
F. Eßer
M. Fehrenbacher
C. Franke
F. Fuchs
K. Gao
S. Germer
F. Günther
A. Heidarian
I. Hilger
Y. Ji
J. Kelling
N. Klingner
E. Kowalska
M. Langer
F. Liu
T. Lorenz
F. Lungwitz
M. Mittendorff
J. Osten
J. Otto
B. Pelic
J. Schmidt
E. Schumann
S. Seidel
T. Sendler
G. Steinbach
D. Stephan
M. Teich
B. Teschome
A. Wagner
K. Wagner
Y. Wang
R. Wenisch
M. Wieser
R. Wutzler
O. Yildirim
Y. Yuan

STUDENTS (diploma / MSc / BSc)

S. Baldauf
M. Braun
S. Bräunig
M. Hähnel
H. Hentschel
S. Hoffmann
N.K. Katkoju
R. Kießling
M. Kusch
V. Liersch
K. Manjunath
S. Rupp
M. Schiwarth
B. Schreiber
M. Xu

Institute of Ion Beam Physics and Materials Research
P.O. Box 51 01 19 · 01314 Dresden/Germany
Phone +49 351 260-2345
Fax +49 351 260-3285
http://www.hzdr.de

Member of the Helmholtz Association